

*The Electronic Structure and Reactivity of Sulfide Surfaces: Combining Atomic-Scale Observations with Theoretical Calculations*

Kevin M. Rosso

Dissertation submitted to the Faculty of the Virginia Polytechnic Institute and State University in partial fulfillment of the requirements for the degree of

Doctor of Philosophy  
in  
Geology

Michael F. Hochella, Jr., Chair  
David F. Cox  
John G. Dillard  
Gerald V. Gibbs  
James D. Rimstidt

June 5<sup>th</sup>, 1998  
Blacksburg, Virginia

**Keywords:** Pyrite, covellite, STM, tunneling spectroscopy, oxidation, adsorption, electronic structure, coesite, electron density, Laplacian

*Copyright 1998, Kevin M. Rosso*

# *The Electronic Structure and Reactivity of Sulfide Surfaces: Combining Atomic-Scale Observations with Theoretical Calculations*

Kevin M. Rosso

## ***Abstract***

The electronic structure of clean pyrite {100} and covellite {001} surfaces have been investigated in ultra-high vacuum (UHV) for the purpose of understanding the nature of sulfide surface reactivity. Using primarily scanning tunneling microscopy and spectroscopy (STM/STS), the electronic structure at atomic sites on these surfaces was directly probed, and chemical insight into the results was provided by *ab-initio* calculations. Pyrite is the most abundant sulfide at the earth's near surface. Its oxidation influences a wide variety of natural and industrial chemical process, but very little is known about the stepwise oxidation reactions involved. For this reason, the first two chapters are directed at understanding the surface electronic structure and fundamental reactivity of pyrite surfaces at the atomic scale. UPS spectra show a characteristic peak at  $\sim 1$  eV forming the top of the valence band for the near surface. *Ab-initio* calculated densities of states for the bulk crystal suggest that this band is comprised primarily of non-bonding Fe 3d  $t_{2g}$  and lesser S 3p and Fe 3d  $e_g$  states. *Ab-initio* slab calculations predict that the broken bonding symmetry at the surface displaces a Fe 3d  $d_{z^2}$  dangling bond state into the bulk band gap. Evidence confirming the presence of this surface state is found in low bias STM imaging and normalized single-point tunneling spectra, which are in remarkable agreement with calculations of the LDOS at surface Fe and S sites. The results predict that due to the dangling bond surface states, Fe sites are energetically favored for redox interaction with electron donors or acceptor species. STM/STS observations of

O<sub>2</sub>/H<sub>2</sub>O exposed surfaces are consistent with this assertion, as are *ab-initio* cluster calculations of adsorption reactions between O<sub>2</sub>/H<sub>2</sub>O derived species and the {100} surface. Furthermore, an enhancement in the “rate” of oxidation was discovered using UPS on pyrite surfaces exposed to a mixture of O<sub>2</sub>/H<sub>2</sub>O. Cluster calculations of adsorption energies reveal a similar result for the case where both O<sub>2</sub> and H<sub>2</sub>O are dissociated on the surface and sorbed to Fe sites.

Covellite, similar to pyrite, is a natural semiconducting metal sulfide. In contrast, however, precious metal bearing solutions have a curiously lower affinity for covellite surfaces than for pyrite. At the same time, its unique combination of low resistivity and perfect basal cleavage represented a unique opportunity to improve our ability to interrogate metal sulfide surfaces using STM/STS at the atomic scale. *Ab-initio* calculations predict that cleaving covellite exposes two slightly different surfaces, one is expected to have dangling bonds, the other is not. Atomic-scale STM images and LEED patterns indicate that the surface structure is laterally unreconstructed. The STM images are predicted to show Cu sites as high tunneling current sites on the dangling bond covered surface, and S sites on the other. Based on tunneling spectra and tip-induced effects therein, reasonable arguments are presented which allow one to uniquely differentiate between the two possible surfaces.

For both pyrite and covellite, the combination of experiment and theoretical calculations afforded much more insightful conclusions than either would have alone. The calculations provided the necessary chemical framework with which to make interpretations of the experimental data and, in this sense, contribute information obtainable by no other means. This point is further developed in an investigation of Si-O interactions and the electron density distribution in the model silicate coesite, which is presented in the appendix. In addition, it breaks new ground by delving into differences and similarities between periodic vs. cluster calculations of minerals.

## ***Acknowledgements***

In the professional regard, there are a lot of people I wish to thank for their unselfish help and support over the years. Thanks first to Mike for taking me on as his student, entrusting me with his expensive toys, and training me well. I also thank my committee members for their valuable input towards many different aspects of the work presented here today. Special thanks to Dave and John for use of their equipment, to Don for his insight into geochemistry, and to Jerry for his mineralogical acumen and passionate perspective on the future of mineralogy. I am also thankful for being surrounded by the many talented peers that did or currently shape our research group, namely Russ, Udo, Barry, Dirk, Jeanne, Maureen, Steven, Eric, John, Jodi, Chris, and Rob. Group meetings were very fun and productive, something of a hybrid between a WWF match and a meeting of the minds. Many others contributed to my success here in ways that they might not recall, but I do. Thanks to Cahit for being such an admirable department head. And to Frank Harrison, Bob Bodnar, and Frank Cromer for use of their facilities, expertise, and equipment, especially Frank's soldering iron. Thanks to David Larsen, Mark Lemon, Bob Montgomery, and John and Eric Wonderly, for the computer/electronics assistance. And to Mark Fortney for photographic needs. Jean Plymale's help from the Computing Center was essential for access to and maintenance of workstations. Susan Eriksson helped tremendously with acquiring samples. Jerome Long contributed brain power and equipment for Hall effect measurements. And finally, I'd like to end with some MVP's. All the ladies in the main office, Linda, Mary, Carolyn, and Connie kept me feeling like I was in good hands with administrative and academic needs. And literally none of my experimentation would have been possible without the skills of Dan Smith, especially when I needed to have square holes drilled.

This dissertation may be destined to end-up collecting a lot of digital dust, but some things from my time here will not. Had these things not been in place, work would have just been, well, work. So, on a more personal note, I wish give thanks to those who give my life

meaning. Thanks first to God who is the only one who can read my dissertation and say, "Been there, made that." He also showed me that knows me better than I know myself by giving me my wonderful wife Jodi. These pages can't hold all the things she means to me. Likewise, I thank my parents John and Lorna, and Harp and Barbara for so many years of love and support. I'm also very thankful for my friendships with Mike and Barbara and Michael and Katherine. I look forward to seeing them in Montana each year. I'm honored to also have what I hope will be lasting friendships with Jerry Gibbs, Paul Ribbe, and Don Bloss, some of the pillars of this department. With the same sentiment, I value the friendships that have developed with my peers, Keith and Patricia Wood, Eric Rufe and Maria Rapien (soon to be the Rufe's), Barry and Keiko Bickmore, Udo Becker, and the rest of the gang.

*Lift your eyes and look to the heavens: Who created all these? He who brings out the starry host one by one, and calls them each by name. Because of his great power and mighty strength, not one of them is missing.*

*Isaiah 40:26*

# Table of Contents

<i>Abstract</i> .....	<i>ii</i>
<i>Acknowledgements</i> .....	<i>iv</i>
<i>Table of Figures</i> .....	<i>x</i>
<i>Table of Tables</i> .....	<i>xiv</i>
<i>Chapter One - Introduction</i> .....	<i>1</i>
Overview.....	1
Looking Ahead.....	4
References Cited.....	6
<i>Chapter Two - Atomically Resolved Electronic Structure of Pyrite {100} Surfaces: An Experimental and Theoretical Investigation with Implications for Reactivity</i> .....	<i>9</i>
Introduction.....	9
Methods.....	10
<i>Principal Instrumentation</i> .....	<i>10</i>
<i>Samples</i> .....	<i>10</i>
<i>Low Energy Electron Diffraction</i> .....	<i>11</i>
<i>Ultra-violet Photoelectron Spectroscopy</i> .....	<i>11</i>
<i>Scanning Tunneling Microscopy and Spectroscopy</i> .....	<i>12</i>
<i>Ab-initio Calculations</i> .....	<i>13</i>
Results and Discussion.....	15
<i>Surface Microtopography and Atomic Structure</i> .....	<i>15</i>
<i>Bulk and Surface Electronic Structure</i> .....	<i>18</i>
<i>Atomic Scale Scanning Tunneling Microscopy</i> .....	<i>29</i>
<i>Scanning Tunneling Spectroscopy</i> .....	<i>35</i>
<i>Calculated Local Densities of States</i> .....	<i>41</i>
<i>Beam-Induced Surface Alteration</i> .....	<i>42</i>

Summary.....	45
References Cited.....	45
<i>Chapter Three - The Interaction of Pyrite {100} Surfaces with O<sub>2</sub> and H<sub>2</sub>O: Fundamental Oxidation Mechanisms.....</i>	<i>52</i>
Introduction.....	52
Methods.....	54
<i>Principal Instrumentation and Samples.....</i>	<i>54</i>
<i>Gas Dosing.....</i>	<i>54</i>
<i>X-ray Photoelectron Spectroscopy.....</i>	<i>55</i>
<i>Ultra-violet Photoelectron Spectroscopy.....</i>	<i>55</i>
<i>Low Energy Electron Diffraction.....</i>	<i>56</i>
<i>Scanning Tunneling Microscopy and Spectroscopy.....</i>	<i>56</i>
<i>Ab-initio Calculations.....</i>	<i>57</i>
Results / Discussion.....	58
<i>Photoelectron Spectroscopy / LEED.....</i>	<i>58</i>
<i>Scanning Tunneling Microscopy.....</i>	<i>68</i>
<i>Scanning Tunneling Spectroscopy.....</i>	<i>76</i>
<i>Ab-initio Calculations.....</i>	<i>80</i>
Summary and Implications.....	89
References Cited.....	90
<i>Chapter Four - A UHVSTM/STS and Ab-Initio Investigation of Covellite {001} Surfaces.....</i>	<i>96</i>
Introduction.....	96
Methods.....	97
<i>Principal Instrumentation and Samples.....</i>	<i>97</i>
<i>Ultra-violet Photoelectron Spectroscopy.....</i>	<i>98</i>
<i>Low Energy Electron Diffraction.....</i>	<i>98</i>
<i>Scanning Tunneling Microscopy and Spectroscopy.....</i>	<i>98</i>
<i>Ab-initio Calculations.....</i>	<i>99</i>
Results / Discussion.....	99
<i>Surface Atomic Structure.....</i>	<i>99</i>
<i>Electronic Structure.....</i>	<i>103</i>

<i>Scanning Tunneling Microscopy</i> .....	106
<i>Scanning Tunneling Spectroscopy</i> .....	110
Summary.....	114
References Cited.....	115
<i>Appendix - SiO and BeO bonded interactions: A comparison of crystalline, molecular and experimental electron density distributions</i> .....	119
Abstract.....	119
Introduction.....	120
<i>Electron density distributions and the chemical bond</i> .....	120
<i>Properties of the Laplacian</i> .....	121
<i>Diagnostics of an electron density distribution</i> .....	121
<i>Goals</i> .....	122
Calculated and observed bond critical point properties.....	123
<i>Model crystal</i> .....	123
<i>Earlier calculations</i> .....	125
<i>Crystal calculations</i> .....	125
<i>Molecular calculations</i> .....	126
<i>Observed electron density distribution</i> .....	127
Trends between calculated and observed bond critical point properties.....	127
<i>A comparison of molecular and crystal results</i> .....	127
<i>A comparison of observed and calculated bcp properties</i> .....	133
<i>Calculations for BeO</i> .....	136
Discussion.....	137
References.....	140
<i>Curriculum Vitae</i> .....	144

## ***Table of Figures***

<i>Chapter Two - Atomically Resolved Electronic Structure of Pyrite {100} Surfaces: An Experimental and Theoretical Investigation with Implications for Reactivity</i> .....	9
Figure 1: Ball and stick model of the pyrite {100} surface.....	16
Figure 2: LEED image of in-vacuum cleaved pyrite {100}.....	17
Figure 3: Topographic UHV STM images showing pyrite cleavage surface microtopography. ....	19
Figure 4: Topographic UHV STM image showing high step density. ....	20
Figure 5: Topographic UHV STM image showing flat {100} terraces separated by curved unit-cell high step edges.....	21
Figure 6: He I UPS valence band spectra of an in-vacuum cleaved pyrite {100} surface.....	23
Figure 7: Calculated total and projected densities of states for the valence band of bulk pyrite. ....	24
Figure 8: Cross-section of the 9-monolayer periodic slab.....	26
Figure 9: Calculated projected densities of states for the Fe 3d states in both bulk and surface environments in pyrite. ....	27
Figure 10: Calculated projected densities of states for the S 3p states in both bulk and surface environments in pyrite. ....	28
Figure 11: Atomic-scale raw topographic and current UHV STM images of in-vacuum cleaved pyrite {100}.....	31
Figure 12: Atomic-scale topographic and current UHV STM images showing two terraces separated by a half-unit cell high step. ....	32
Figure 13: Diagram showing the bias voltage values corresponding to atomically resolved UHV STM images. ....	33
Figure 14: Dual-mode UHV STM images collected simultaneously. ....	34
Figure 15: Schematic band structure diagrams modeling the tip-pyrite tunneling contact. .	36

Figure 16: Area-averaged normalized $(dI/dV)/(I/V)$ tunneling spectrum. ....	38
Figure 17: Single-point normalized $(dI/dV)/(I/V)$ tunneling spectra and calculated local densities of states. ....	40
Figure 18: Area-averaged $I(V)$ tunneling spectra collected on in-vacuum cleaved pyrite comparing the tunneling current response in the dark vs. illuminated conditions.....	44
<i>Chapter Three - The Interaction of Pyrite {100} Surfaces with O<sub>2</sub> and H<sub>2</sub>O: Fundamental Oxidation Mechanisms</i> .....	52
Figure 1: He I UPS valence band spectra and difference spectra for pristine pyrite surfaces and those exposed to O <sub>2</sub> gas. ....	59
Figure 2: He I UPS valence band spectra comparing pristine pyrite surfaces with those exposed to O <sub>2</sub> , O <sub>2</sub> - H <sub>2</sub> O, and air.....	63
Figure 3: He I UPS valence band difference spectra of pyrite surfaces that were exposed to similar doses of different mixtures of O <sub>2</sub> -H <sub>2</sub> O, and a surface that was exposed to a much larger dose of pure O <sub>2</sub> .....	64
Figure 4: He I UPS spectra showing no change in the valence band structure of a pyrite surface exposed to various doses of O <sub>2</sub> (L) after the surface had been irradiated with He I UV light.....	66
Figure 5: XPS spectra of UV-exposed and unexposed pyrite allowed to oxidize in air for 7 days. ....	67
Figure 6: Atomic-scale topographic UHV STM image of an in-vacuum cleaved pyrite {100} surface after exposure to 4 L oxygen.....	69
Figure 7: Dual-mode current UHV STM images collected simultaneously on pyrite {100} exposed to 4 L oxygen. ....	70
Figure 8: Topographic and current UHV STM images collected on pyrite {100} exposed to 4 L oxygen. ....	72
Figure 9: Topographic and current UHV STM images collected on pyrite {100} exposed to 4 L oxygen. ....	73
Figure 10: Topographic and current UHV STM images collected on pyrite {100} exposed to 0.4 L 40 mol % O <sub>2</sub> (O <sub>2</sub> -H <sub>2</sub> O).....	74

Figure 11: I(V) area-averaged tunneling spectra collected over a random distribution of points on pristine and O <sub>2</sub> exposed surfaces. ....	77
Figure 12: Area-averaged (dI/dV)/(I/V) tunneling spectra and difference spectra (reacted - unreacted) collected over a random distribution of points on pristine and O <sub>2</sub> exposed surfaces. ....	78
Figure 13: 27-atom cluster of pyrite used for <i>ab-initio</i> calculations of the interaction of the {100} surface with oxygen and water species. ....	81
Figure 14: Optimized cluster configurations and reaction energies for the interaction of the pyrite {100} surface with O <sub>2</sub> and O. ....	83
Figure 15: Optimized cluster configurations and reaction energies for the interaction of the pyrite {100} surface with water and dissociated water species. ....	85
Figure 16: Optimized cluster configurations and reaction energies for the interaction of the pyrite {100} surface with oxygen and water species. ....	87
<b>Chapter Four - A UHVSTM/STS and Ab-Initio Investigation of Covellite {001} Surfaces.....</b>	<b>96</b>
Figure 1: The structure of covellite viewed perpendicular and parallel to the <i>c</i> -axis. ....	101
Figure 2: A comparison of experimental valence band spectra (He I UPS) with calculated densities of states. ....	105
Figure 3: UHV STM images of the basal plane of covellite cleaved in air. ....	107
Figure 4: Topographic and current UHV STM images of the atomically resolved basal plane of in-nitrogen cleaved covellite. ....	108
Figure 5: Current UHV STM image of the atomically resolved basal plane of in-air cleaved covellite. ....	109
Figure 6: Atomic-scale current UHV STM image of the {001} surface of in-air cleaved covellite. ....	111
Figure 7: Schematic band structure diagrams modeling the tip-covellite tunneling contact. ....	113

*Appendix - SiO and BeO bonded interactions: A comparison of crystalline, molecular and experimental electron density distributions..... 119*

Figure 1: Plot of the observed SiO bond length in coesite vs.  $f_s(O)$ , the *s*-character of the bond..... 124

Figure 2: Scatter plots of the SiO bond lengths observed for coesite vs. the bcp properties of the bonds calculated for the crystal. .... 129

Figure 3: Scatter plots of the SiO bond lengths observed for coesite vs. the bcp properties of the bonds calculated for two  $H_{12}Si_5O_{16}$  molecules. .... 131

Figure 4: Scatter plots of the bcp properties calculated for a coesite crystal vs. those calculated for  $H_{12}Si_5O_{16}$  molecules. .... 132

Figure 5: Scatter plots of the ellipticity of the SiO bonds in coesite calculated for a coesite crystal, calculated for  $H_{12}Si_5O_{16}$  molecules, and observed for coesite vs.  $f_s(O)$ . .... 134

Figure 6: Scatter plots of the bcp properties calculated for a coesite crystal vs. those observed..... 135

## ***Table of Tables***

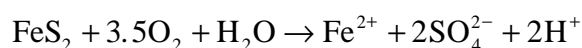
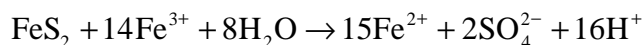
Table 1: Bond critical point properties for the symmetry unique bonds in covellite. ....	102
Table 2: Bond Critical Point Properties For SiO <sub>2</sub> . ....	128
Table 3: Bond Critical Point Properties For BeO. ....	137

## **Chapter One**

### **Introduction**

#### **OVERVIEW**

Transition metal sulfides form an important class of minerals that are found in many geologic settings, from ore deposits to anoxic sedimentary environments to contact metamorphic zones. Pyrite ( $\text{FeS}_2$ ) is undoubtedly the most common and interesting of all the sulfides as it occurs in all the above environments as well as many others. It is unique among its related counterparts in that it naturally crystallizes in a variety of crystal forms, in both high and low temperature environments. When pyrite is exposed, either naturally or artificially, to aqueous solutions at atmospheric conditions, it oxidatively decomposes, and in the process releases dissolved ferrous iron and sulfuric acid into the environment primarily by the following reactions:



These reactions are now well-known due to the many years of research summarized in reviews by Lawson (1982), Hiskey and Schlitt (1982), and Nordstrom (1982), and also due to the environmental problems that result from them. However, the details of these reactions are just now being revealed. In this regard, it can be seen from the above reactions that the individual subreactions must involve the removal of 7 electrons from each sulfur in pyrite, whereas the oxidation state of iron remains unchanged overall. A key piece of information was provided by the isotopic tracer studies of Taylor and Wheeler (1984) and Reedy *et al.* (1991), which showed that where either of the above reactions is prevailing, oxygen in the end-product

sulfate is primarily derived from dissociated water. This means that water participates more as a reactant and less as a spectator species.

Elucidating more detail about these subreactions has been the topic of more recent studies, many of which have ensued from a surface science perspective. Using primarily X-ray photoelectron spectroscopy on pyrite surfaces that had been exposed to air or solution, it has been shown that oxidation products appear on reacted surfaces in the general order: Iron oxides and/or hydroxides, iron sulfate, and an iron-deficient sulfide layer (*e.g.* Buckley and Woods, 1987; Mycroft *et al.*, 1990; Karthe *et al.*, 1993; Nesbitt and Muir, 1994; Knipe *et al.*, 1995). Collectively, the aqueous and surface analytical investigations have led to several models for the stepwise oxidation process, although they lacked the spatial resolution required to make unambiguous conclusions on the specific surface sites involved in the reactions. The first study to address this problem using STM was a watershed event. Direct observation of the growth of oxidation patches on pyrite surfaces in air showed that there is much to be learned about pyrite oxidation by visiting the atomic scale (Eggleston *et al.*, 1996). In many respects, our knowledge stops here, although additional relevant facts have been contributed in other studies that have not mentioned in this brief overview.

In a sense, the work presented in this dissertation was performed with the same goal of attempting to understand the fundamental oxidation mechanisms. However, it is unique in that it is the first to approach the problem with atomic spatial resolution on pristine pyrite surfaces in the chemical isolation of ultra-high vacuum. Chapter 2 addresses the surface electronic structure of pyrite, which is the basis of surface reactivity, and Chapter 3 involves the surface chemistry of pyrite exposed to O<sub>2</sub>/H<sub>2</sub>O mixtures in vacuum. The primary contribution is in our understanding of the surface sites involved in electron transfers, the complementary roles of the oxidant and water, and chemical basis for reactivity at the initial stages of pyrite oxidation. The results can be tied back in with previous surface analytical observations in that

dissociated gas species on the surface interact with Fe sites, forming Fe-O bonds and incipient iron oxide/oxyhydroxide phases. Furthermore, a mechanism is presented by which surface S sites may become susceptible to hydrophyllic attack, consistent with the idea that dissociated water species combine with oxidized S to form sulfate eventually.

At the same time, on the broader canvas, this dissertation is an attempt to advance our science even more by utilizing tunneling spectroscopy. This work is the first in geologic circles to endeavour to collect atomically resolved tunneling spectra, following in the tradition of the seminal studies on silicon surfaces (Hamers *et al.*, 1987; Hamers, 1988). This technique is not without its difficulties, however, and it met with varying degrees of success depending on many factors, most of which are extremely difficult to control like the atomic structure at the end of the tip. Moreover, the particular tunneling conditions necessary for atomically resolved images on pyrite are very different than those for optimal spectral data collection. Although there is a method to circumvent this problem (Mårtensson and Feenstra, 1989; Feenstra, 1994), it is not compatible with the electronics of our instrument. This precluded the collection of atomically resolved images and spectra simultaneously. However, single-point spectra collected on pyrite could be understood when compared to what was predicted using *ab-initio* calculations of the local density of states of the sample over surface sites (Chapter 2). This remarkable result in itself is probably the foremost achievement herein in that demonstrates the underexploited potential of combining tunneling spectroscopy with theory to unambiguously characterize the local electronic structure.

Covellite (CuS) is another important transition metal sulfide with unique electrical and structural characteristics that lead to its interesting behavior in the geochemistry of ore deposits. As opposed to pyrite, precious metals are known to have a much lower affinity for covellite surfaces (Guilbert and Park, 1986), and in that respect, this makes the study of this material at the atomic-scale potentially rewarding. In contrast to pyrite, this mineral lended

itself to atomically resolved simultaneous STM/STS. This, combined with the unique surface characteristics of covellite (CuS), became the impetus for the work presented in Chapter 4. It is hoped that the tunneling spectra and the related discussions therein contribute insight into the complexities of using tunneling spectroscopy on geologic materials and thereby continue to advance our science.

A final thread that is prevalent in this dissertation is the mutual dependence of experimental and theoretical results. Interpretations of the STM/STS data, for both pyrite and covellite, were only made possible by using theoretical electronic structure calculations. Yet, at the same time, the calculations do not stand unchecked against verifiable experimentation. This symbiosis should perhaps be our key scientific creed when our experimental investigations take us to the atomic scale. This theme is continuous into the appendix where work is presented that directly compares experimental and theoretical determinations of electron density distributions in the model silicate, coesite. Using the theory of Atoms-in-Molecules developed recently (see Bader, 1990), properties of Si-O bonds such as bond strength and covalency are uniquely understood in terms of the electron density distribution. In contrast to the other chapters, the results in this study show poorer agreement between experiment and theory owing to the difficulties in the determination of experimental electron density distribution. It thereby demonstrates that some studies can only be convened from theory.

## LOOKING AHEAD

Since its inception, the use of scanning tunneling microscopy in the geologic sciences has increased slowly and perhaps steadily, but apparently it is still in a phase where it is proving its worth. In that regard, and including the work presented here, it has given us "first looks" at the atomic structures on surfaces of many important natural materials including galena,

hematite, pyrite, pyrrhotite, molybdenite, and covellite. Images collected at this scale also give us rare glimpses at a variety of structural defects such as dislocations, point vacancies, and can even capture dynamic surface processes such as surface energy minimization (Rosso *et al.*, in preparation). Studies such as these reveal not only the atomic structure of the surface, but implicitly address a more important property with respect to reactivity - the surface electronic structure. STM has also been successfully used to document adsorption and surface chemical processes on some of these minerals. For example, the adsorption of sulfate at step edges on hematite has been recently investigated using atomic scale STM imaging (Eggleston *et al.*, 1998), and in this dissertation, the mechanism of the oxidation of pyrite surfaces by  $O_2/H_2O$  is investigated. However, studies such as these are few and far between and they are being performed by only a handful of groups in the geologic sciences. The lackluster popularity is perhaps due to the fact that it can only be used on semiconducting or electrically conducting minerals. Even if this is widely held as the foremost drawback of STM, it seems to me that there is still a tremendous number of important questions on STM-compatible minerals that can be answered best by obtaining atomic-scale observations. For example, a variety of manganese oxides appear to be sufficiently conductive such that cleavage or more likely in-vacuum prepared surfaces could be imaged successfully. In doing so, one might be able to address their surface chemical properties that lead to their well known affinity for heavy metals. The same approach would be valuable for the common suite of natural iron oxides as well. This point can easily be expanded to include a wide range of interesting problems in geochemistry in the areas of photo-redox surface reactions and the reductive precipitation of precious metals on surfaces.

I believe that many of these problems can and eventually will be effectively addressed from a combined tunneling microscopic, spectroscopic, and theoretical strategy. And in the years to follow, we can probably expect to see the arrival of newer atomically resolved SPMs,

like chemical SPM, which will open new doors into the atomic-scale on a whole new suite of minerals and problems.

### REFERENCES CITED

- Bader, R.F.W (1990) *Atoms in molecules: A quantum theory*, 438 p. Oxford Science Publications, Oxford.
- Buckley, A.N., and Woods, R. (1987) The surface oxidation of pyrite. *Applied Surface Science*, 27, 437-452.
- Eggleston, C.M., Ehrhardt, J.-J., and Stumm, W. (1996) Surface structural controls on pyrite oxidation kinetics: An XPS-UPS, STM, and modeling study. *American Mineralogist*, 81, 1036-1056.
- Eggleston, C.M., Hug, S., Stumm, W., Sulzberger, B., Afonso, M.D. (1998) Surface complexation of sulfate by hematite surfaces: FTIR and STM observations. *Geochimica et Cosmochimica Acta*, 62, 585-593.
- Feenstra, R.M. (1994) Tunneling spectroscopy of the (110) surface of direct-gap III-V semiconductors. *Physical Review B*, 50, 4561-4570.
- Guilbert, J.M., and Park, C.F. (1986) *The geology of ore deposits*, 985 p. Freeman, New York.
- Hamers, R., Tromp, R., and Demuth, J. (1987) Electronic and geometric structure of Si (111)-(7 × 7) and Si (001) surfaces. *Surface Science*, 181, 346-355.
- Hamers, R. (1988) Characterization of localized atomic surface defects by tunneling microscopy and spectroscopy. *Journal of Vacuum Science and Technology B*, 6, 1462-1467.
- Hiskey, J.B., and Schlitt, W.J. (1981) Aqueous oxidation of pyrite. In *Proceedings of the 2<sup>nd</sup> SME-SPE International Solution Mining Symposium*, Denver CO, 55-74.

- Karthe, S., Szargan, R., and Suoninen, E. (1993) Oxidation of pyrite surfaces: A photoelectron spectroscopic study. *Applied Surface Science*, 72, 157-170.
- Knipe, S.W., Mycroft, J.R., Pratt, A.R., Nesbitt, H.W., and Bancroft, G.M. (1995) X-ray photoelectron spectroscopic study of water adsorption of iron sulphide minerals. *Geochimica et Cosmochimica Acta*, 59, 1079-1090.
- Lowson, R.T. (1982) Aqueous oxidation of pyrite by molecular oxygen. *Chemical Reviews*, 82, 461-497.
- Mårtensson, P., and Feenstra, R.M. (1989) Geometric and electronic structure of antimony on the GaAs (110) surface studied by scanning tunneling microscopy. *Physical Review B*, 7744-7753.
- Mycroft, J. R., Bancroft, G. M., McIntyre, N. S., Lorimer, J. W., and Hill, I. R. (1990) Detection of sulphur and polysulphides on electrochemically oxidized pyrite surfaces by X-ray photoelectron spectroscopy and Raman spectroscopy. *Journal of Electroanalytical Chemistry* 292, 139-152.
- Nesbitt, H.W., and Muir, I.J. (1994) X-ray photoelectron spectroscopic study of a pristine pyrite surface reacted with water vapor and air. *Geochimica et Cosmochimica Acta*, 58, 4667-4679.
- Nordstrom, K. D. (1982) Aqueous pyrite and the consequent formation of secondary minerals. In *Acid Sulfate Weathering: Pedogeochemistry and Relationship to Manipulation of Soil Materials*: Madison, Wisconsin (ed. J. A. Kittrick, D. S. Fanning, and L. R. Hossner), pp. 37-56. Soil Science Society of America Press.
- Reedy B. J., Beattie J. K., and Lowson R. T. (1991) A vibrational spectroscopic  $^{18}\text{O}$  tracer study of pyrite oxidation. *Geochimica et Cosmochimica Acta* 55, 1609-1614.
- Rosso, K.M., Becker, U., and Hochella, M.F., Jr. (in preparation) "Real-time" UHVSTM observation and molecular modeling of surface defect healing on pyrite.

Taylor B. E. and Wheeler M. C. (1984) Stable isotope geochemistry of acid mine drainage:  
Experimental oxidation of pyrite. *Geochimica et Cosmochimica Acta* 48, 2669-2678.

## **Chapter Two**

# ***Atomically Resolved Electronic Structure of Pyrite {100} Surfaces: An Experimental and Theoretical Investigation with Implications for Reactivity***

### **INTRODUCTION**

Pyrite ( $\text{FeS}_2$ ) plays an important chemical role in many natural processes such as the redox cycling of metals (e.g. Moore and Luoma, 1990; Calmano *et al.*, 1994; Nimick and Moore, 1994), precious metal ore deposit formation (e.g. Nash *et al.*, 1981; Jean and Bancroft, 1985; Bakken *et al.*, 1989; Hyland and Bancroft, 1989; Starling *et al.*, 1989), and the generation of environmentally hazardous acid mine drainage (e.g. Jambor and Blowes, 1994). It is also a photovoltaic semiconductor with potential applications in solar energy conversion (e.g. Bronold *et al.*, 1994a). As such, there has been much interest in understanding the nature of its reactivity, particularly its oxidation. Most of the groundbreaking research to that end was conducted prior to the early 1980s (see references in Hiskey and Schlitt, 1981; Lowson, 1982; and Nordstrom, 1982). However, our understanding of its surface chemistry and the fundamental oxidation reactions, a topic of more recent studies, remained predominantly unaddressed at that time. A likely reason for this arose from the former lack of experimental techniques where surface-sensitive microscopic and spectroscopic observations could be applied with a suitable level of chemical isolation (Hochella *et al.*, in press). A recent ambient STM study of pyrite by Eggleston *et al.* (1996) has provided the best picture yet of the atomic scale reactivity of pyrite fracture surfaces. Beyond this, surfaces must be investigated in a controlled environment where the surface properties can be considered pristine. Furthermore, the site-specific electronic structure of the surface has not been studied, the basis upon which a better understanding of reactivity should be built. In this paper, we investigate pristine pyrite surfaces in ultra-high vacuum (UHV) using scanning tunneling microscopy and spectroscopy

(STM/STS), ultra-violet photoelectron spectroscopy (UPS), low energy electron diffraction (LEED), and theoretical calculations with a goal of understanding the atomic-scale electronic structure of the surface. Herein the first atomically resolved tunneling spectra on a geochemically significant natural material are presented. The experimental results are interpreted using *ab-initio* calculations. This investigation is meant to elucidate the site-specific variables of primary importance and to aid in future investigations of fundamental pyrite surface reactivity.

## METHODS

### Principal Instrumentation

All the experimental techniques were performed in a OMICRON compact UHV lab operating at a base pressure of  $1 \times 10^{-10}$  mbar. The main chamber is equipped with a dual anode (Al,Mg) x-ray source, UV lamp, ion gun, a reverse view LEED with a 1 keV electron gun, cylindrical sector electron energy analyzer, and a sample heater capable of heating to 750 °C. The system is also equipped with an in-house built gas leak manifold for controlled gas bleeds to various parts of the main chamber. A side chamber contains an STM stage, its vibration isolation and eddy current damping system, and the tunneling in-vacuum electronics.

### Samples

Natural pyrite single crystal cubes from Logroño, Spain were obtained from the Museum of Geological Sciences at Virginia Tech. The samples were cut into approximately  $5 \times 5 \times 10$  mm oriented prisms with faces perpendicular to the principal crystallographic. The resistivity of one of the samples was measured to be  $3 \times 10^{-4}$   $\Omega$ ·m and Hall voltage measurements on the same sample indicated that it was *n*-type. Since it has been shown that the semiconducting properties of pyrite are consistent for samples derived from similar geologic environments (Pridmore and Shuey, 1976), it is assumed that all the samples used in this study were *n*-type.

Samples showing any visible inclusions were discarded. The samples were mechanically mounted in custom stainless steel stubs and cleaved using an in-house built cleavage stage in the load-lock chamber which is turbo-pumped to better than  $1 \times 10^{-7}$  mbar. The prisms were slightly notched to control fracture propagation. Pyrite cleaved in the load-lock chamber was quickly transferred to the lower base pressure of the main chamber in less than 30 seconds.

### **Low Energy Electron Diffraction**

LEED patterns were acquired using 4-grid reverse view LEED optics (OMICRON) at beam energies between 70 - 300 eV. The electron gun has a beam diameter of approximately 1 mm. Diffraction patterns were photographically recorded. The data were collected immediately after turning up the beam energy because the intensity and sharpness of the diffraction spots were found to degrade within a few minutes. The surface cell dimension was determined using the measured separation between diffraction spots arising from the reciprocal face-centered cubic lattice.

### **Ultra-violet Photoelectron Spectroscopy**

UPS spectra were collected using He I (21.2 eV) radiation and a pass energy of 10 eV. The sample stubs and the notches in the pyrite prisms used in the UPS experiments were sputter coated with a visible layer of Au to isolate the Fe spectral data to that coming from the cleaved surface. Ten spectral scans were collected over a period of 10 minutes to average out noise. The absolute binding energy scale of the UPS spectra was referenced to the sample Fermi level, which was determined by subtracting 21.2 eV from the low kinetic energy photoelectron cutoff energy and adding the workfunction of the spectrometer. The low kinetic energy edge was designated at the energy half way between the 16% and 84% count rate levels at the cutoff. The workfunction of the spectrometer is based on the measured position of the Ag  $3d_{5/2}$  photo peak.

## Scanning Tunneling Microscopy and Spectroscopy

The STM tip is rastered using a tripod piezo scanner with a 1.2  $\mu\text{m}$  lateral scan range. The bias voltage is applied to the sample while the tip is held at ground potential. Tips were prepared by electrochemically etching W wire in 1 M KOH, except for the spectral data presented in Figure 17, which were pre-cut commercial Pt-Ir tips (Digital Instruments). Surfaces with large, flat terraces were targeted for atomic-scale imaging. It turned out that the most ideal tunneling conditions for atomically resolved images were at low negative bias voltages, between -0.40 to -0.02 V, using a 1 nA setpoint current. For larger scale topographic imaging, 1 V and 1 nA were used. Larger scale images were processed by fitting and subtracting a planar background. Atomically resolved images that required processing to remove noise were band pass FFT filtered by passing the frequencies pertaining to "topographic" features (low frequency) and atomic periodicity. Samples and tips were stored under base pressure in a carousel attached to the main chamber. Samples were shielded from light during all STM imaging, and images were collected at room temperature.

I(V) tunneling spectra were collected over 1  $\text{nm}^2$  imaging areas on a well developed {100} terrace. At each spectroscopy point, the tip raster was paused, the feedback loop was turned off, the voltage ramp was applied, the loop was re-engaged, and imaging resumed. Spectra were collected at room temperature, which has been estimated to have a maximum energy resolution of  $\sim 100$  mV taking into account thermal broadening effects (Hansma, 1982; Chen, 1993). All spectra were collected in the dark unless otherwise noted. Because the most successful imaging conditions were at very low bias for atomically resolved images, the tip-sample distance was relatively small. During the voltage ramp at a spectral point, the exponentially increasing tunneling current would quickly saturate the current-to-voltage converter. Because of an instrumental control limitation, the tip-sample separation could not be adjusted simultaneously during the voltage ramp, a technique known as the varying-gap method (Mårtensson and Feenstra, 1989; Feenstra, 1994). In order to collect wide dynamic

range spectra, tunneling conditions were re-optimized for a larger tip-sample separation for spectral data collection. Using 4 V and 7 nA allowed a -4 to +4 V dynamic range in the voltage ramp. The raw  $I(V)$  curves were converted to  $(dI/dV)/(I/V)$  using a least-squares moving window fit. This form removes the tip-sample separation dependence of the tunneling conductance under certain conditions (Feenstra *et al.*, 1987) and can provide information that is related to the density of states of the sample under the assumption that the tip density of states is constant. The mathematical spike at low bias was suppressed by adding a small constant to  $I/V$  across the entire voltage range before the conversion.

### ***Ab-initio* Calculations**

*Ab-initio* calculations were performed using GAUSSIAN94 (Frisch *et al.*, 1995) for cluster calculations, and CRYSTAL95 (Dovesi *et al.*, 1996) and TOPOND (Gatti, 1997) for periodic structure calculations. The TOPOND code is the implementation of the theory of atoms-in-molecules (see Bader, 1990) for CRYSTAL95. The computer platforms utilized were two DEC Alpha stations and an IBM SP2 at Virginia Tech. For the GAUSSIAN94 calculations, after investigating various cluster sizes and basis sets and weighing in the factor of computational expense, a 27-atom stoichiometric cluster was chosen to model the pyrite {100} surface. It is a charge neutral section of the bulk face-centered cubic crystal structure: 9 atomic layers by 9 atomic layers by 6 atomic layers thick. The basis set used was a standard 6-311G. Polarization functions were not added to the basis set. The wavefunction was calculated at the density functional level of theory using the Becke3LYP hybrid method. For the CRYSTAL95 and TOPOND calculations, an electron core pseudopotential (ECP) basis set was used. Specifically, a LANL2DZ (REFS) set was used in which the net core charges attributed to the Fe ( $1s,2s,2p$ ) and the S ( $1s,2s,2p$ ) orbitals are mimicked by pseudopotential functions. This is justified because these orbitals are not expected to play a significant role in molecular orbital states near the Fermi level. The basis set was modified by removing diffuse functions with gaussian exponents  $< 0.1$ , which are usually not appropriate for the crystalline case (see Pisani, 1996),

and energy optimized the exponent of the most diffuse function on Fe. The sensitivity of the calculated DOS and projected DOS to changes in this exponent was tested and it was found that the basis set effects were negligible. The wavefunctions were calculated at the DFT level of theory using the Lee-Yang-Parr (Lee *et al.*, 1988) correlation potential and the Becke (Becke, 1988) exchange potential in the Kohn-Sham computational approach. 45 k-points (Monkhorst net) were sampled in the irreducible part of the Brillouin zone. Fock matrix mixing and Fermi-level shifting techniques were implemented to overcome slow SCF convergence.

Local densities of states (LDOS) were calculated for comparison with experimental normalized tunneling spectra using the methods similar to those described in Becker and Hochella (1996). The comparison can only be made under the assumption that the effect of the tip electronic structure is negligible. The LDOS of the sample at locations of the tip was computed by summation of the contributions of the atomic orbitals to the molecular orbitals that fall within a specified energy range (the bias voltage). Because the basis sets are gaussian functions which tail-off relatively quickly, they poorly describe the decay of wavefunctions normal to the surface. This means that the calculated LDOS at the location of the tip at normal tunneling distances of 3-10 Å from the surface is nil. Although there are more sophisticated ways to attack this problem (Becker and Hochella, 1996), a reduced tip-sample distance of 1 Å was used to obtain an approximation of the LDOS of surface sites. Also, because the cluster is treated from a molecular orbital theory approach and not a periodic approach, the state densities were convoluted with gaussian functions (FWHM = 0.5), with unity areas and centered at eigenvalues, in order to mimic the dispersion of states into bands and account for the resolution of the experimental spectra.

## RESULTS AND DISCUSSION

### Surface Microtopography and Atomic Structure

Bulk pyrite is face-centered cubic with a structure that is reminiscent of the rocksalt structure type (Fig. 1). A unique aspect of the pyrite structure is the  $S_2$  anion pair which is oriented along body diagonals of the cubic cell. Prediction of the surface structure largely revolves around the question of whether or not the S-S bond preferentially remains intact during cleavage. Since it is known that bond strength is proportional to the electron density at the bond critical point (bcp) and is inversely related to bond length (Feynman, 1939; Boyd *et al.*, 1988), we used TOPOND/CRYSTAL95 to perform an analysis of the critical point properties of the Fe-S and S-S bonds. The results show that the valence electron density is 29% higher at the S-S bcp relative to that for the Fe-S bond. As compared to the Fe-S bond (2.26 Å), the S-S bond (2.14 Å) is a relatively short, more strongly covalent bond that should not be expected to be pervasively broken during cleavage. Pyrite fracture surfaces are predominantly conchoidal but there is indistinct cleavage quality along cubic faces, which is a reflection of planes in the structure which pass through the least number of disulfide pairs.

LEED patterns of the freshly fractured surface were bright and sharp, but tended to degrade to weaker patterns in a matter of a few tens of seconds due to electron beam damage. The patterns were dominated by intense diffraction points characteristic of the reciprocal face centered cubic cell (Fig. 2). Less intense points with twice the periodicity are  $S_2$  derived diffraction points (Pettenkofer *et al.*, 1991). Calculation of the surface cell constant from the LEED patterns yields a value of 5.45 Å which compares reasonably well with the bulk lattice constant of 5.417 Å (Fuji *et al.*, 1986). Although lateral relaxation appears to be insignificant, relaxation to some degree perpendicular to the plane of the surface is likely because it is well known that crystal structures have a tendency to structurally relax in this direction to compensate for lost bonding symmetry (Jaegermann and Tributsch, 1988; Hochella, 1990; Zangwill, 1988). The magnitude of relaxation does not appear to be significant in case of the

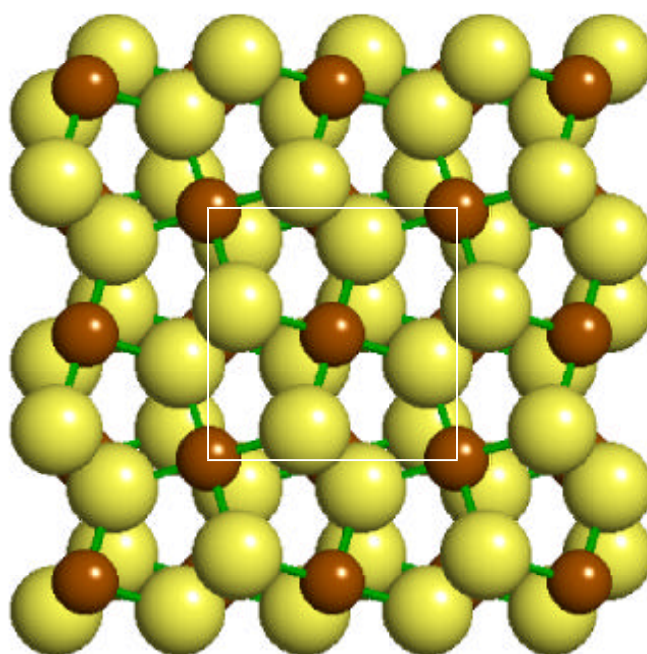


Figure 1: Ball and stick model of the pyrite  $\{100\}$  surface. Fe and  $S_2$  centers are arranged in a face-centered cubic lattice. A surface cell is indicated.

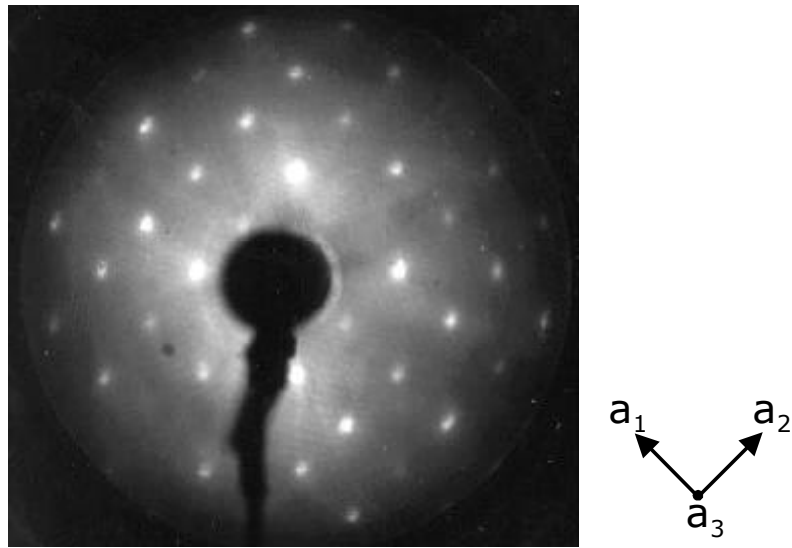


Figure 2: LEED image of in-vacuum cleaved pyrite  $\{100\}$ . The image was collected using a beam energy of  $134.6 \text{ eV}$ . The crystal was oriented as indicated by the axes.

pyrite {100} surface. *Ab-initio* cluster calculations on the 27-atom pyrite cluster were performed with lifted symmetry constraints to investigate the magnitude of structural relaxation. It was found that the lowest energy configuration involved minimal structural displacement with a maximum atomic coordinate displacement of less than 0.1 Å. Collectively, the LEED and cluster suggest that the {100} surface structure can be regarded as bulk-terminated.

Topographic, or Z-piezo voltage, UHVSTM images at scales of several hundred nanometers demonstrate that the microtopography of the cleavage surfaces is dominated by stepped terraces. The images in Figure 3 show the flat surfaces that are generated by fracture, terminated by unit cell high steps. The images and LEED results suggest that pyrite cleaves rather well along the cubic axes at this scale, exposing {100} surfaces. Furthermore, it is noteworthy that crystallographic control is demonstrated in preferred step edge directions along the two dimensions of the surface, oriented along  $\langle 10 \rangle$  and/or  $\langle 21 \rangle$ . In Figure 3a the prevalent step edge direction is  $\langle 10 \rangle$ , in Figure 3b it is a combination, and in Figure 3c, the edge propagation is along  $\langle 21 \rangle$ . Less common areas were also found where the step density was relatively high as in Figure 4, although the step edge direction is still along a principal crystallographic axis. Step edge control was, for the most part, pronounced, but not exclusive as shown in Figure 5 where curved steps were found, indicating a high kink density along these step edges. Areas on the large, flat terraces of the surface were targeted for the high resolution UHV STM/STS data collection in this study.

## Bulk and Surface Electronic Structure

The electronic structure of bulk pyrite has been studied at length (Li *et al.*, 1974; Ogawa *et al.*, 1974; Schlegel and Wachter, 1976; Van der Heide *et al.*, 1980; Bullett, 1982; Folmer *et al.*, 1988; Ferrer *et al.*, 1990; Huang *et al.*, 1993; Mosselmans *et al.*, 1995; Bocquet *et al.*, 1996; Charnock *et al.*, 1996; Evert *et al.*, 1998) and will only be summarized here as a starting point for this discussion of the surface electronic structure. The upper part of the valence band consists

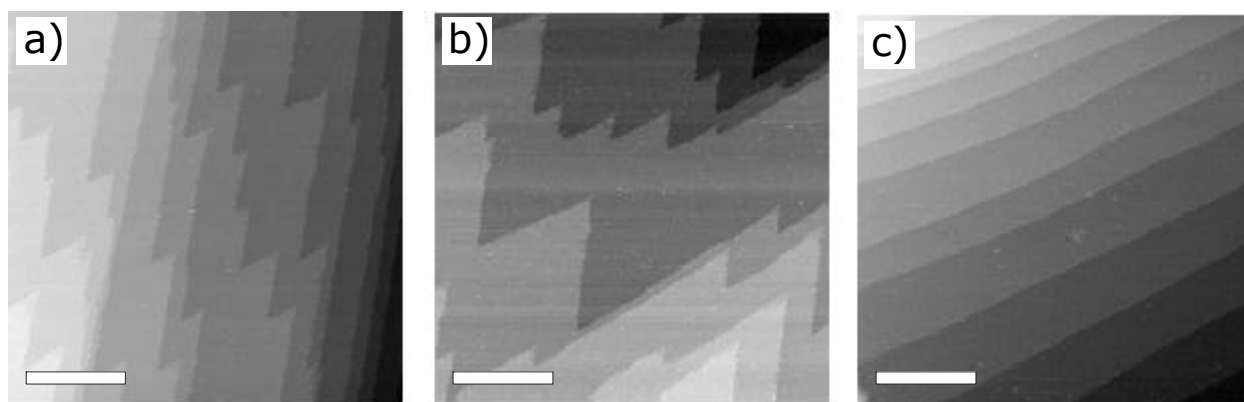


Figure 3: Topographic UHV STM images showing pyrite cleavage surface microtopography.

The scale bars represent 100 nm. Unit cell high steps run along primarily  $\langle 10 \rangle$  (a)

$\langle 10 \rangle$  and  $\langle 11 \rangle$  (b), and  $\langle 11 \rangle$  directions.

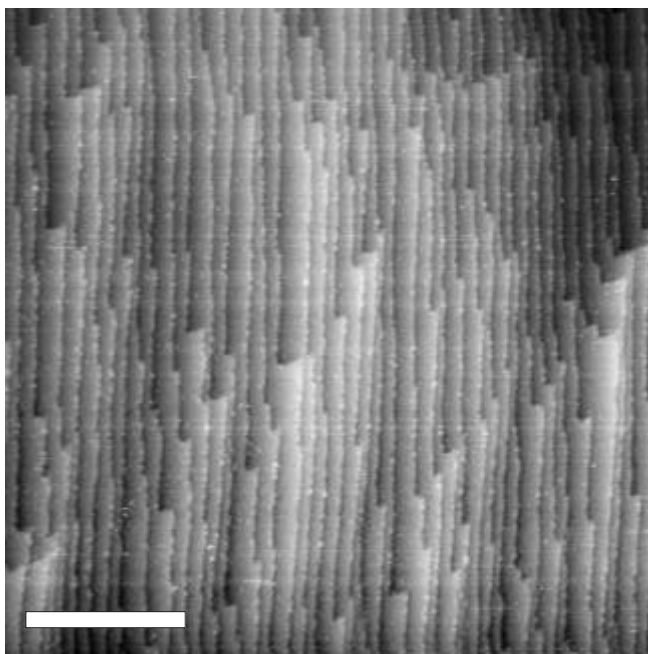


Figure 4: Topographic UHV STM image showing the high step density that was also commonly found on cleaved pyrite. The scale bar represents 100 nm.

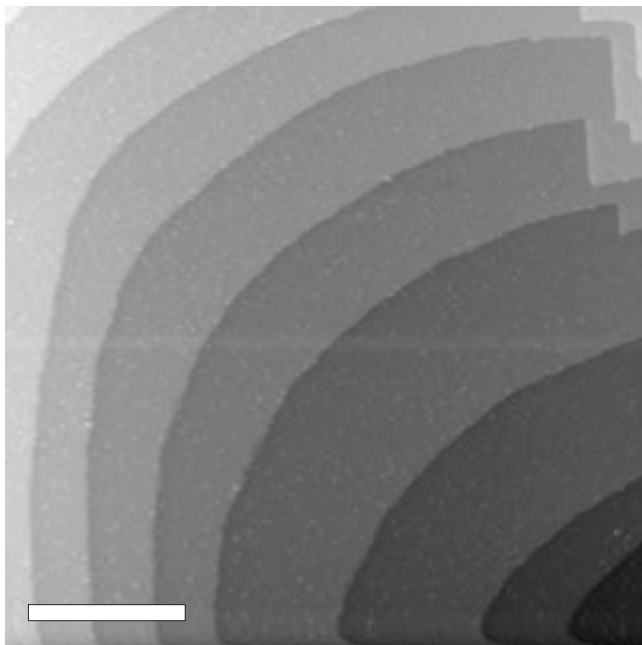


Figure 5: Topographic UHV STM image showing flat  $\{100\}$  terraces separated by curved unit-cell high step edges. The scale bar represents 100 nm. The cubic axes are approximately aligned with the image edges.

of predominantly a non-bonding Fe 3d  $t_{2g}$  band which lies above a bonding S 3p - Fe 3d  $e_g$  band. The lower part of the conduction band is well regarded to be dominated by Fe 3d  $e_g^*$  - like states, although there are arguments for the presence of S 3p states (Evert *et al.*, 1998). The bulk band gap is 0.9 eV. As measured using UPS, there is a characteristic peak in the density of states at the top of the valence band at approximately 1.1 eV which has been overwhelmingly attributed primarily to the non-bonding  $t_{2g}$  - like states (Fig. 6). The states at the top of the valence band are important in the process of pyrite oxidation as they are the highest energy filled states and thus the most susceptible to oxidative attack. This is especially true at the mineral surface where oxidation begins, however we cannot assume that the surface electronic structure is identical to the bulk. Jaegermann and Tributsch (1988) first suggested that the energetic arrangement of Fe 3d states would be changed at the surface of pyrite due to disrupted bonding symmetry. In this study we investigate this possibility and discuss the implications on the way pyrite surfaces should react.

Using CRYSTAL95, we calculated the valence band density of states (DOS) for the bulk crystal (infinite in 3 dimensions) and the {100} surface (infinite in 2 dimensions) and projected the results onto atomic orbitals which could contribute state density to the top of the valence band, which are the Fe 3d and S 3p states. In the bulk case (Fig. 7), the top of the valence band is predominantly of non-bonding Fe 3d  $t_{2g}$  character, as has been previously determined (see references above), but consists of appreciable Fe 3d  $e_g$  and S 3p character as well (Fig. 7). These states lie above a bonding Fe 3d - S 3p band (3 - 7 eV) and S 3p band (7 - 10 eV). States below this latter band are not included in the calculation as they are modeled by core pseudopotentials. The results indicate that the  $e_g$  states form a relatively broad band (~ 6 eV wide) while the  $t_{2g}$  states are largely non-bonding and restricted to a narrow energy range (FWHM ~ 1 eV) at the top of the valence band. Like the  $e_g$  states, the S 3p states are widely dispersed between 1 - 8 eV.

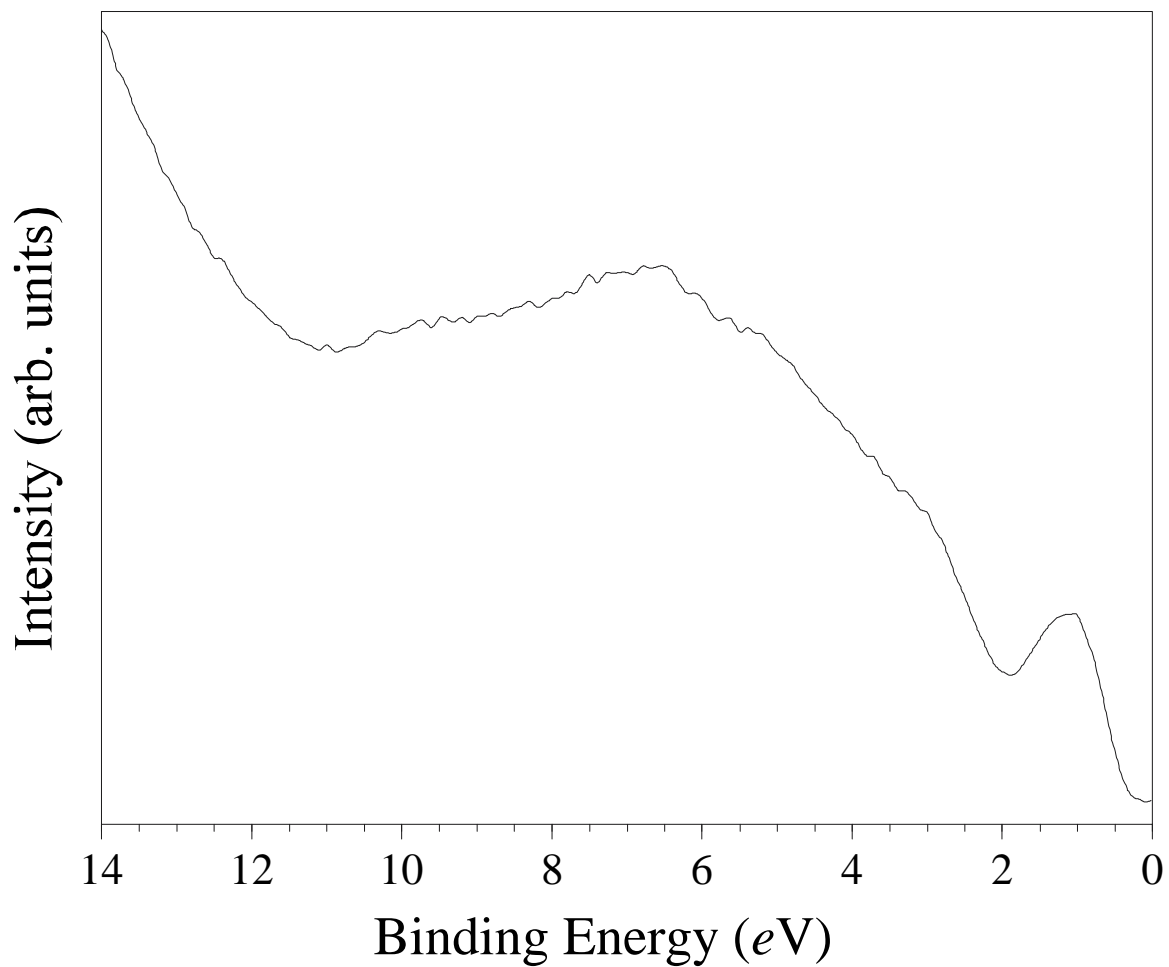


Figure 6: He I UPS valence band spectra of an in-vacuum cleaved pyrite {100} surface.

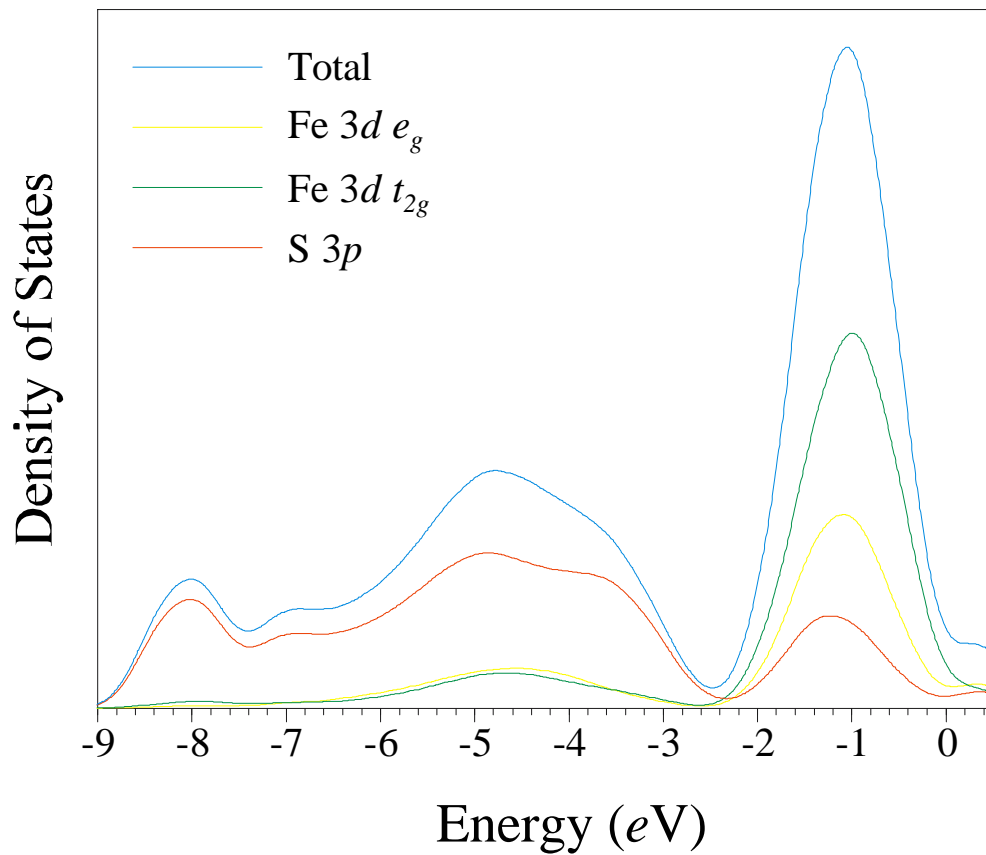


Figure 7: Calculated total and projected densities of states for the valence band of bulk pyrite. The contributions primarily arise from Fe 3d and S 3p states.

At the surface, the degeneracy of the  $t_{2g}$  and  $e_g$  states is lost as a consequence of the lower bonding symmetry. The effect of the reduction in the Fe coordination from the distorted octahedron to square pyramidal on the  $d$ -orbital states has been previously discussed from the semi-quantitative perspective of ligand-field theory (Jaegermann and Tributsch, 1988; Bronold *et al.*, 1994b). A nine monolayer thick slab was chosen to model the {100} surface electronic structure (Fig. 8). Upper valence band state density localized on Fe atoms at the surface were compared with that from Fe atoms located in the middle of the slab, which are fully coordinated and can be taken to represent the bulk sites. According to the slab calculations, the removal of an Fe-S bond and the loss of overlap with S  $3p$  orbitals destabilizes primarily Fe  $d_{z^2}$  states to higher energy and shifts state density into  $d_{x^2-y^2}$  ( $Z$  arbitrarily chosen normal to surface plane) (Fig. 9). The undercoordination of Fe also destabilizes the  $d_{xz}$  and  $d_{yz}$  states to higher energy due to the partial loss of longer range interaction with second nearest-neighbor S. The  $d_{xy}$  states remain largely unaffected as their local coordination environment is essentially unchanged at the surface. In contrast to the Fe  $3d$  states, surface S states show no energetic shift but respond only by a decrease in  $3p$  state density (Fig. 10).

The most significant difference between the bulk and surface electronic structures is then, at the surface, Fe  $d_{z^2}$  states are displaced to the top of the valence band, forming surface states. The calculations make no such indication for S  $3p$  states and so here, it is assumed that they contribute negligible surface state density. Normally, the presence of surface states leads to atomic reconstruction, reducing the surface free energy (see Zangwill, 1988). But based on surface structural evidence to the contrary in this case, these surface states should be preserved and are thus best described as dangling bonds. The symmetry and energy of these dangling bonds are such that they should dictate the surface chemical behavior and, because they are localized on Fe sites, imply an increased reactivity of Fe sites toward oxidation.

Surface environment

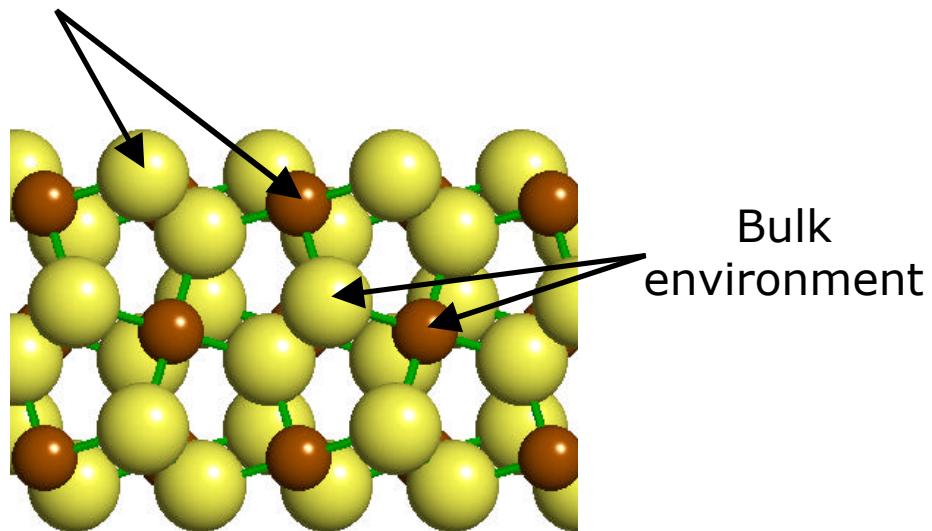


Figure 8: Cross-section of the 9-monolayer periodic slab used to calculate the projected densities of states for bulk and surface environments in pyrite.

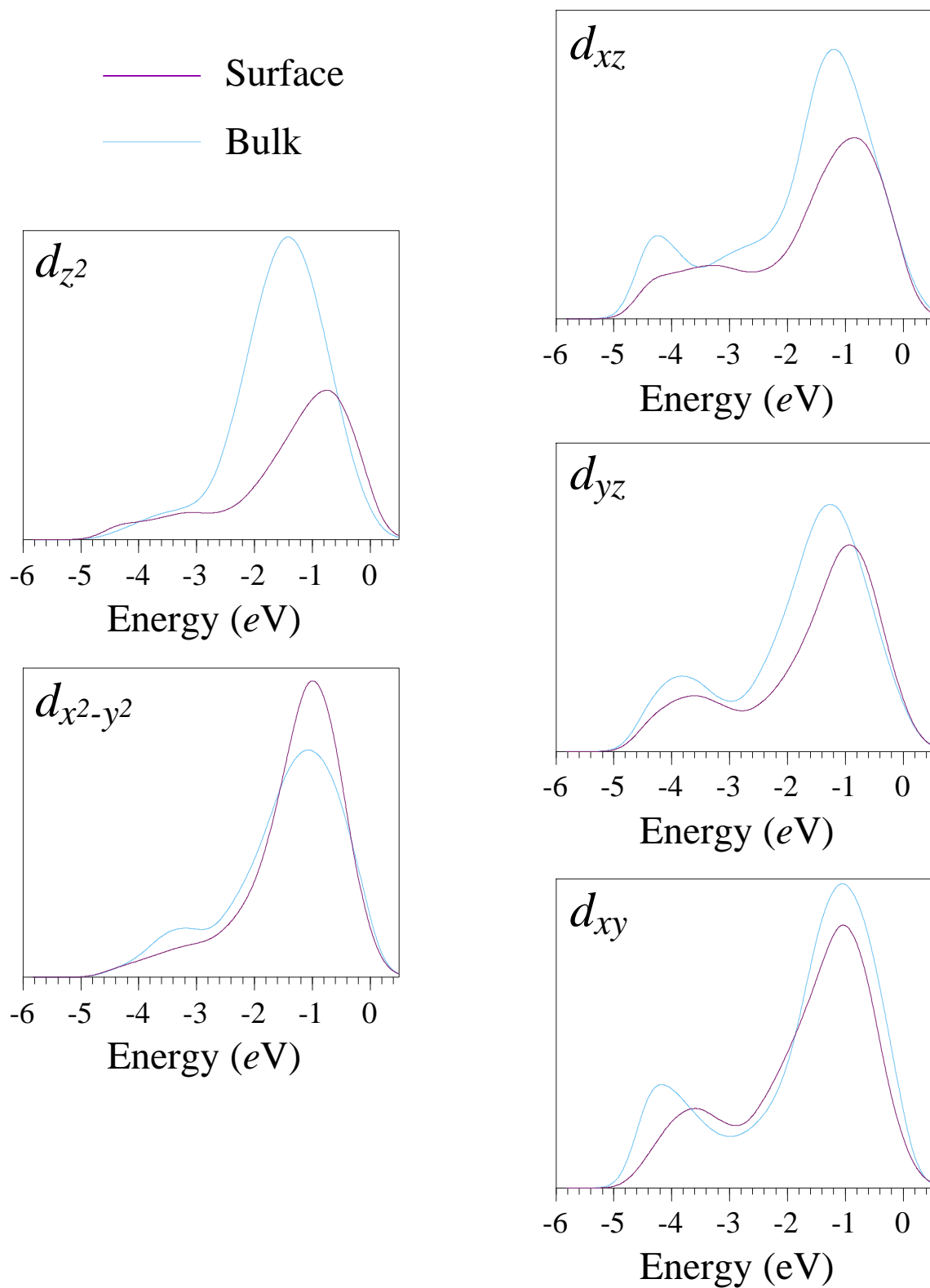


Figure 9: Calculated projected densities of states for the Fe 3d states in both bulk and surface environments in pyrite.

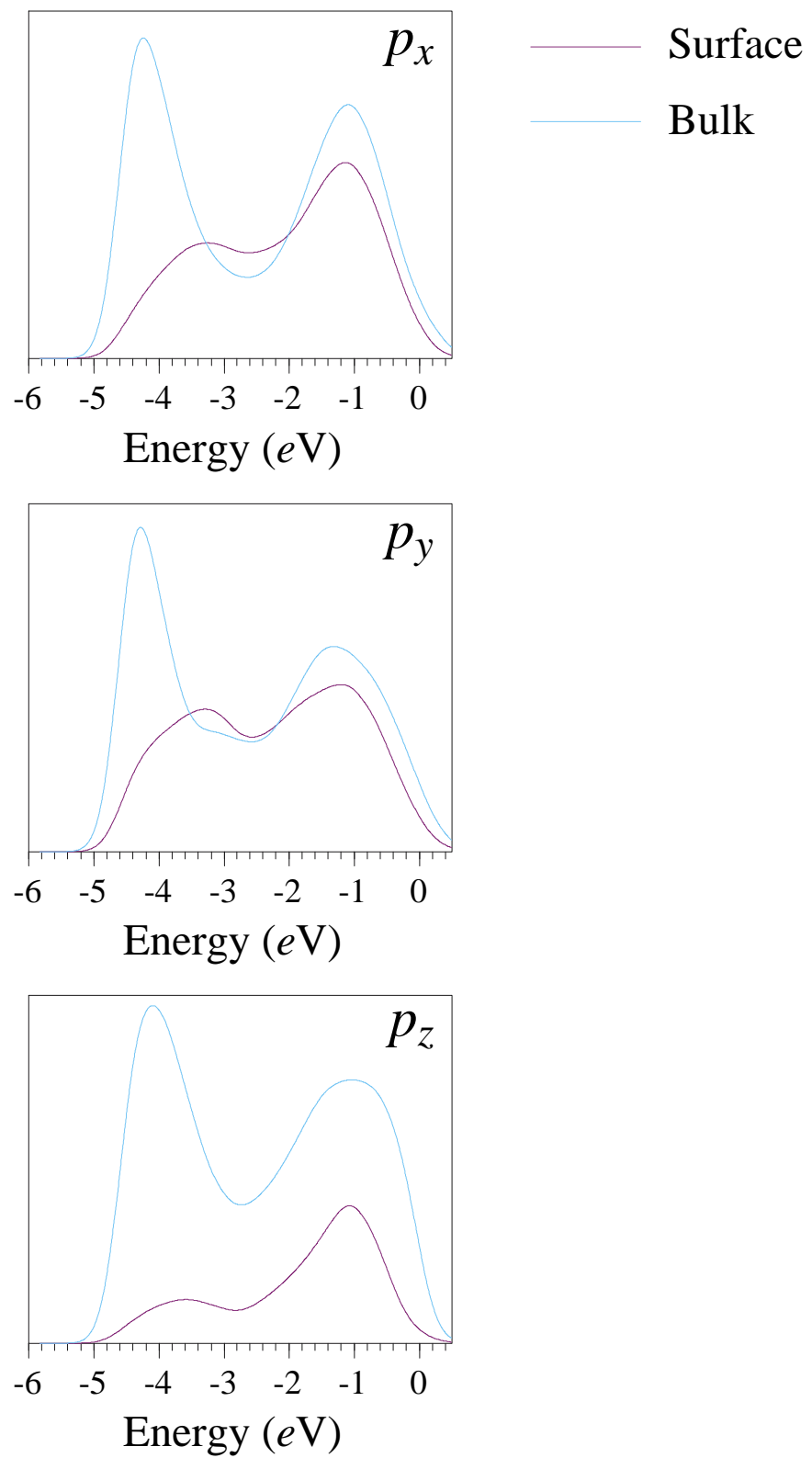


Figure 10: Calculated projected densities of states for the S 3p states in both bulk and surface environments in pyrite.

Mulliken population analyses of the charge distribution in the slab show that charge is preferentially shifted from surface S atoms into the bulk. This means that the charge on surface S atoms is slightly more electropositive than for equivalent sites in the bulk, consistent with the observation that S 3p states are depopulated at the surface. Furthermore, the possibility that the low spin property of bulk pyrite could be converted to high-spin at the surface was investigated (Bronold *et al.*, 1994b). This could have implications for the sorption of paramagnetic species such as O<sub>2</sub> (see Becker and Hochella, 1996). For the same 2-D periodic slab, the system was restricted to a spin-polarized solution for several initial SCF cycles, but the spin configuration always reverted to low spin when the restriction was lifted.

### **Atomic Scale Scanning Tunneling Microscopy**

The power of STM imaging lies in its ability to elucidate the electronic structure of a surface at the atomic scale. Surfaces of pyrite have been previously studied using STM in air (Eggleston and Hochella, 1990; Fan and Bard, 1991; Eggleston and Hochella, 1992; Siebert and Stocker, 1992; Eggleston, 1994; Eggleston *et al.*, 1996). Interpretation of the image data in chemical terms seldom is straightforward, but based on the theoretical calculations, some insight is available. By virtue of the fact that electrons occupying the highest energy filled states are the least tightly bound, they have the longest decay lengths away from the surface into the vacuum. For STM, the implications are that the states which are closest to the Fermi level of the negatively-biased electrode (either the sample or the tip) are the primary contributors to the tunneling current. In the case of a negatively biased sample, electrons tunnel primarily from a narrow energy range of the highest filled states of the sample into empty states of the tip. For a pristine pyrite {100} surface in vacuum, this means that Fe sites should be high tunneling current sites at negative bias because the highest energy filled states are Fe 3d dangling bonds. Furthermore, should the dangling bond states be only partially occupied, Fe sites should appear as high tunneling current sites at low positive bias voltage as well.

Atomic scale UHV STM observations are consistent with these assertions. The images show that the {100} surfaces are atomically flat over nanometer scales separated by half unit cell high steps (Figs. 3-5). Topographic (Z-piezo voltage data) and current image data show an array of high tunneling current sites, the symmetry and spacing of which are consistent with the face centered cubic array of Fe atoms within a {100} plane of the structure (Fig. 11). Figure 11c and 11d are low-pass FFT filtered images of the atomic corrugation in the raw Z and I images, respectively. In all the Figure 11 images, the image edges are roughly aligned with crystallographic axes of the single crystal sample. As shown best in Figure 11a, a step edge and corner is imaged in the lower right corner. The step height, as measured using a topographic profile, is  $\sim 2.5$  Å corresponding to roughly half of a unit cell edge. Figures 12a and 12b are topographic and current images, respectively, which show an atomically resolved, half-unit cell high step edge. The step edge direction along the surface for half unit cell high steps is usually preferential to  $\langle 11 \rangle$  directions although  $\langle 10 \rangle$  control has also been observed.

Images identical to those described above were obtained most successfully at a variety of low bias voltages within the bulk band gap (-400 to -20 mV and +20 to +140 mV) (Fig. 13). Attempts to collect images at biases lower than  $\pm 20$  mV resulted in tip scouring of the pyrite surface. Sets of images collected at positive and negative biases simultaneously (dual-mode STM) were also obtained down to within  $\pm 20$  mV of the Fermi level (Fig. 14). These images show 1 to 1 correspondence of the location of high tunneling current sites, indicating that both the highest occupied and the lowest unoccupied states are localized at surface Fe sites. The narrow voltage range used to collect these images is probably an indication that there is either a surface gap that is no greater than 40 meV, or that the density of surface states is continuous but somewhat reduced closer to the Fermi level. In either case, when combined with the slab calculation results, it can be logically argued that the high tunneling current sites in the dual-mode STM images correspond to partially filled Fe  $d_{z^2}$  - like dangling bond surface states. Their effect on the tunneling behavior of the pyrite surface is shown diagrammatically in

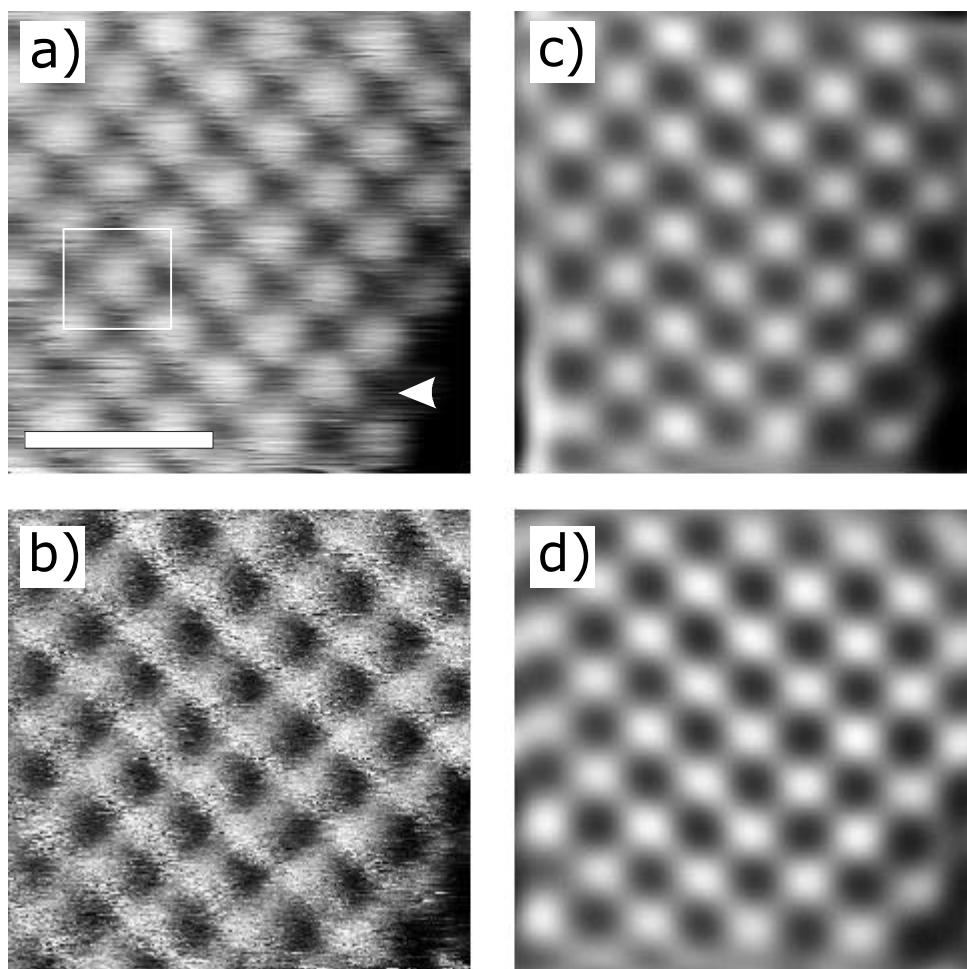


Figure 11: Atomic-scale raw topographic (a) and current (b) UHV STM images of in-vacuum cleaved pyrite {100}. The images in (c) and (d) are low-pass FFT filtered images of (a) and (b), respectively. The scale bar represents 10 Å. The lower-right corner of (a) shows a half-unit cell high step edge. The solid white arrow in (a) points to a corner site in the step edge. The tunneling conditions were -0.2 V bias and 2 nA setpoint current.

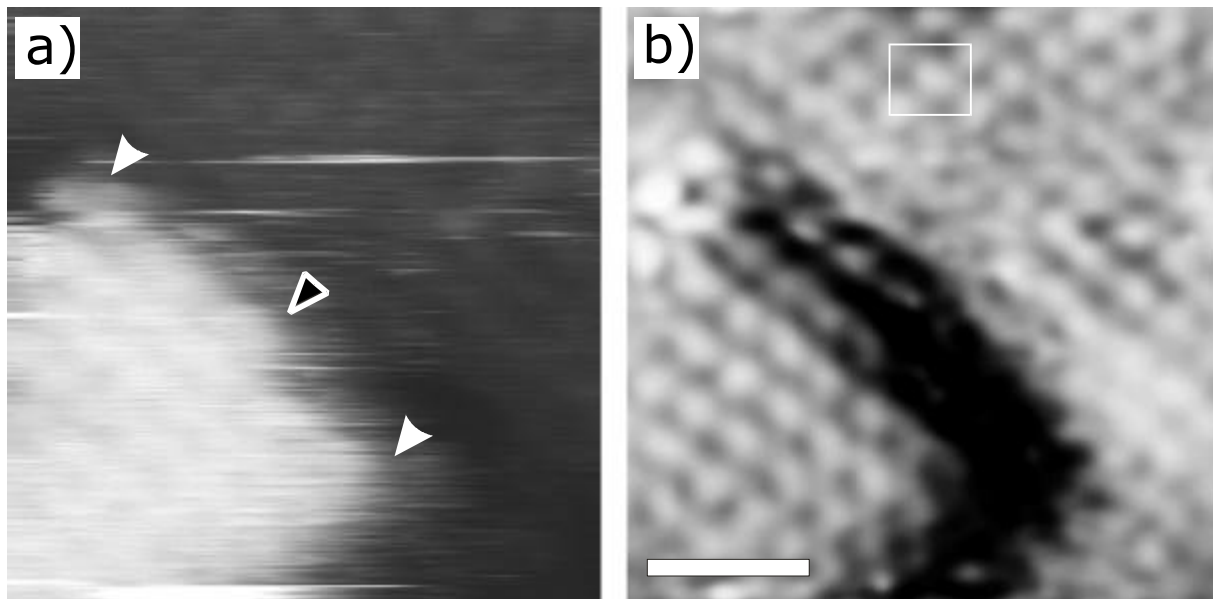


Figure 12: Atomic-scale topographic (a) and current (b) UHV STM images showing two terraces separated by a half-unit cell high step. Solid and outlined white arrows in (a) point to corner and kink sites along the step edge, respectively. The face-centered cubic surface cell (with some unavoidable image distortion) is outlined in (b). The step edge runs along Fe-Fe surface directions. The tunneling conditions were -0.1 V bias and 1.4 nA setpoint current.

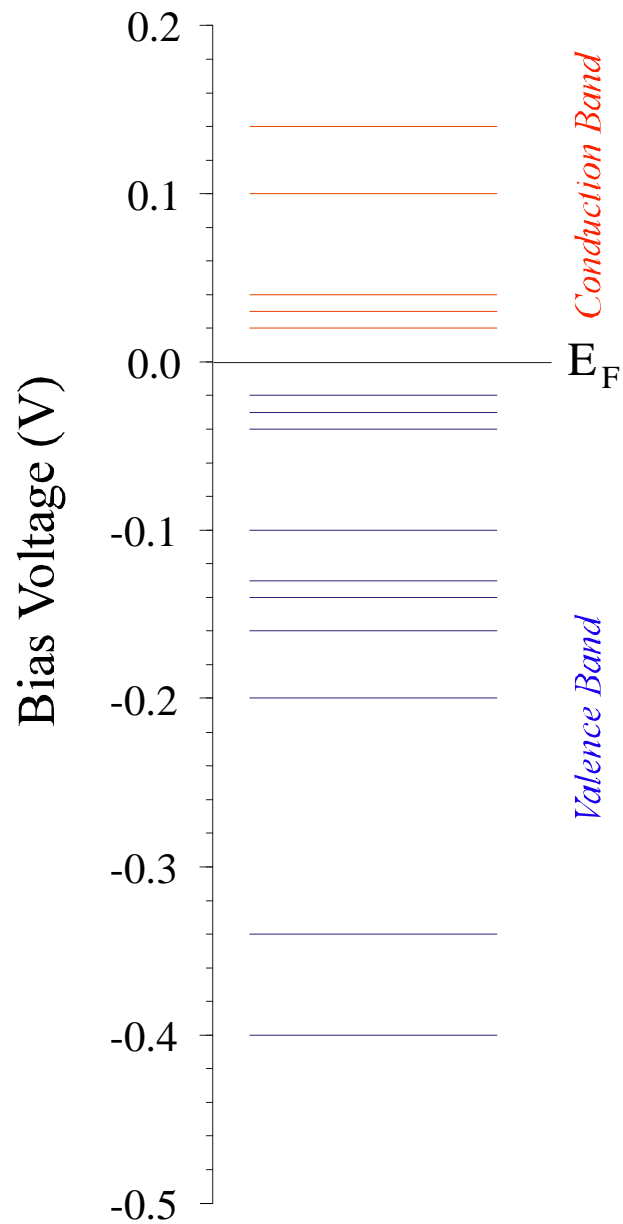


Figure 13: Diagram showing the bias voltage values corresponding to atomically resolved UHV STM images. All of the images showed a face-centered cubic array of bright and dark spots consistent with the expected distribution of surface Fe sites.

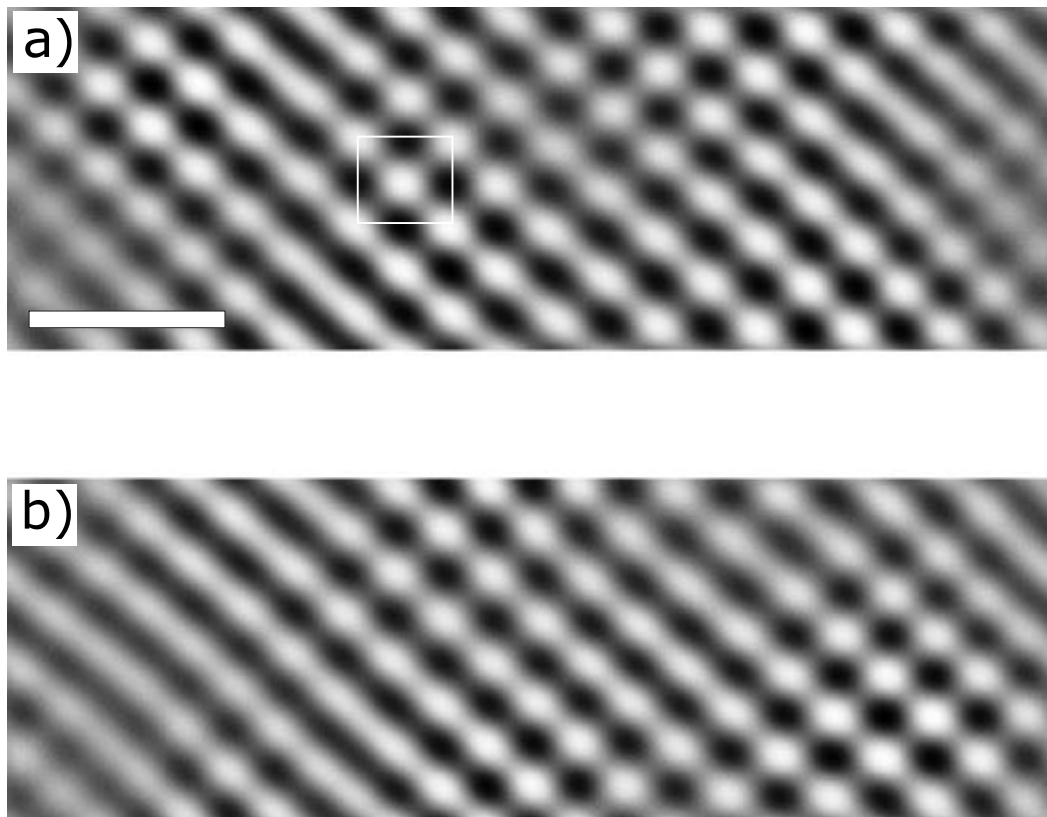


Figure 14: Dual-mode UHV STM images collected simultaneously at  $-0.14$  V bias and  $1.4$  nA setpoint current (a), and  $0.14$  V bias and  $1.0$  nA setpoint current (b). The scale bar represents  $10$  Å. Both images show a face-centered periodic array of bright and dark sites (outlined). The locations of the sites show approximate 1 to 1 correspondence between the images.

Figure 15 for *n*-type pyrite. Equilibration between the pyrite bulk and Fe dangling bond states, located in the bulk band gap, involves filling the surface states up to the position of the bulk Fermi level (Fig. 15a). The charge occupying the surface states constitutes a potential which repels bulk electrons from approaching the surface, resulting in an upward bending of the bulk bands at the surface (Fig. 15a). Equilibration between the tip and sample Fermi levels (Fig. 15b), and the application of bias voltage to the tunneling contact (Figs. 15c and 15d) involves essentially no change in surface electronic structure of the sample. Under conditions of applied bias, electrons originate from (small negative bias, Fig. 15c) or tunnel to (small positive bias, Fig. 15d) surface states at Fe sites. The fact that both the highest energy occupied states and the lowest energy unoccupied states at the surface are localized on Fe sites is an indication that both electron donor and acceptor species sorbed to the surface should interact primarily with Fe sites.

## Scanning Tunneling Spectroscopy

**Area-Averaged Spectra.** Area-averaged tunneling spectra were collected to elucidate the overall distribution of state density at the surface on both sides of the Fermi level. The normalized  $(dI/dV)/(I/V)$  spectrum in Figure 16 is the average of 90 spectra collected at random locations on the surface using several different samples freshly cleaved in UHV and several different etched W tips. The valence band DOS acquired using tunneling spectroscopy is in good agreement with that acquired using UPS (Fig. 6), especially when one considers the remarkable differences in the data acquisition mechanisms. Both spectra show a prominent feature at the top of the valence band, a peak that we have already been able to ascribe to mostly Fe 3*d* and minor S 3*p* states. It can be reasoned, however, that the relative contribution of atomic orbitals to the density of states as measured by the two methods should be somewhat different. The kinetic energy range of the photopeak at the top of the valence band equates to an electron attenuation length of  $\sim 20$  Å (Seah and Dench, 1979) which means that, although UPS is surface sensitive, there is an appreciable contribution of bulk states to the spectrum, *i.e.*

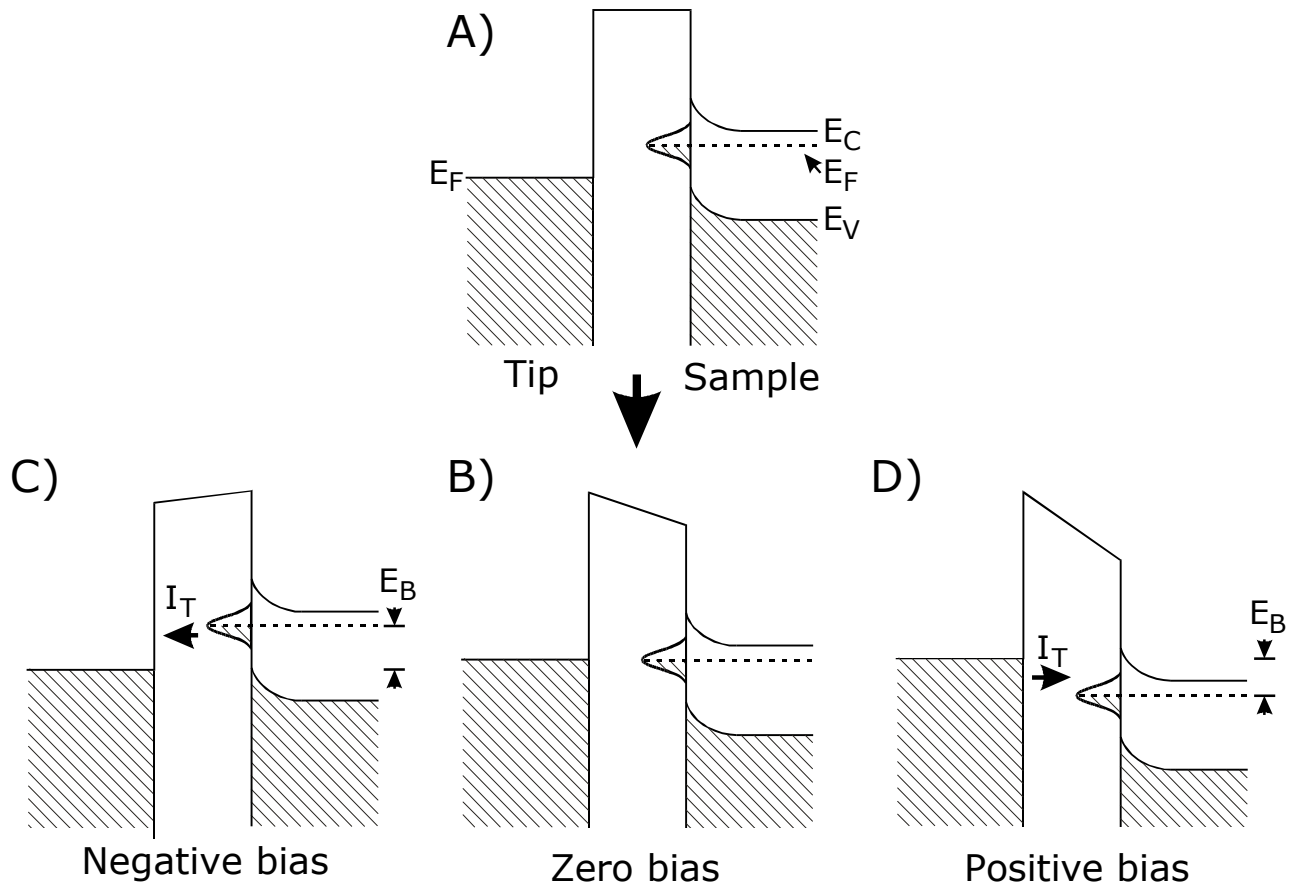


Figure 15: Schematic band structure diagrams modeling the tip-pyrite tunneling contact. a) Thermal disequilibrium between tip and  $n$ -type sample.  $E_C$  and  $E_V$  are the conduction and valence band edges, respectively. Bulk electrons at the Fermi energy infill the surface states, which are dangling bonds localized at Fe sites. Electrons occupying the surface states constitute a surface potential which causes an upward bending of the bulk bands at the surface. b) The zero-bias tip-sample tunneling contact. Under conditions of applied bias, electron tunneling ( $I_T$ ) is accommodated primarily by surface states at both small negative (c) and positive (d) sample bias.

the Fe  $3d t_{2g}$  states. In contrast, tunneling spectroscopy is sensitive only to sample states at the location of the tip, which in this case should be the dangling bond states and S  $3p$  states. The presence of surface state density within the bulk band gap has also been observed using tunneling spectroscopy on pyrite in air (Fan and Bard, 1991; Eggleston *et al.*, 1996).

Revealing the energetic location of the band edges using tunneling spectroscopy is a problematic task. As can be seen in the area-averaged spectrum (Fig. 16), the apparent width of the surface gap is much larger than the dual-mode STM images indicate. The reason for this is partly due to a low S/N ratio for large tip-sample distances, and partly due to a loss of spectral information arising from the well-known mathematical divergence of the  $(dI/dV)/(I/V)$  calculation at very low current values. For semiconductor surfaces, during the collection of  $I(V)$  spectra, the tunneling current approaches zero faster than the bias voltage as the voltage ramp approaches the Fermi level from either direction. Very low current values at finite bias voltages cause the denominator to go to zero and the normalized curve to have a spike in the gap. This artifact can be easily suppressed by adding a small constant to the denominator over the whole curve, at the expense of spectral information in the band gap region. At the same time, the steepness of the  $I(V)$  curve and the width of this flat, low current region is dependent on the tip sample distance. Large tip-sample separations give large low current regions around the Fermi level and thus poor S/N ratios for spectral information from the gap region. However, large separations are needed for wide dynamic range in the  $I(V)$  curve using a fixed tip-sample separation during data collection. Smaller tip-sample separations are needed for spectral data near the Fermi level, at the expense of wide dynamic range. For these reasons, the area-averaged spectrum in this study lacks spectral details near the Fermi level and gives an underestimation of the density of states within the bulk band gap.

**Single-Point Spectra.** Single-point spectra were also collected in an attempt to take advantage of the potential of tunneling spectroscopy to resolve LDOS features at specific

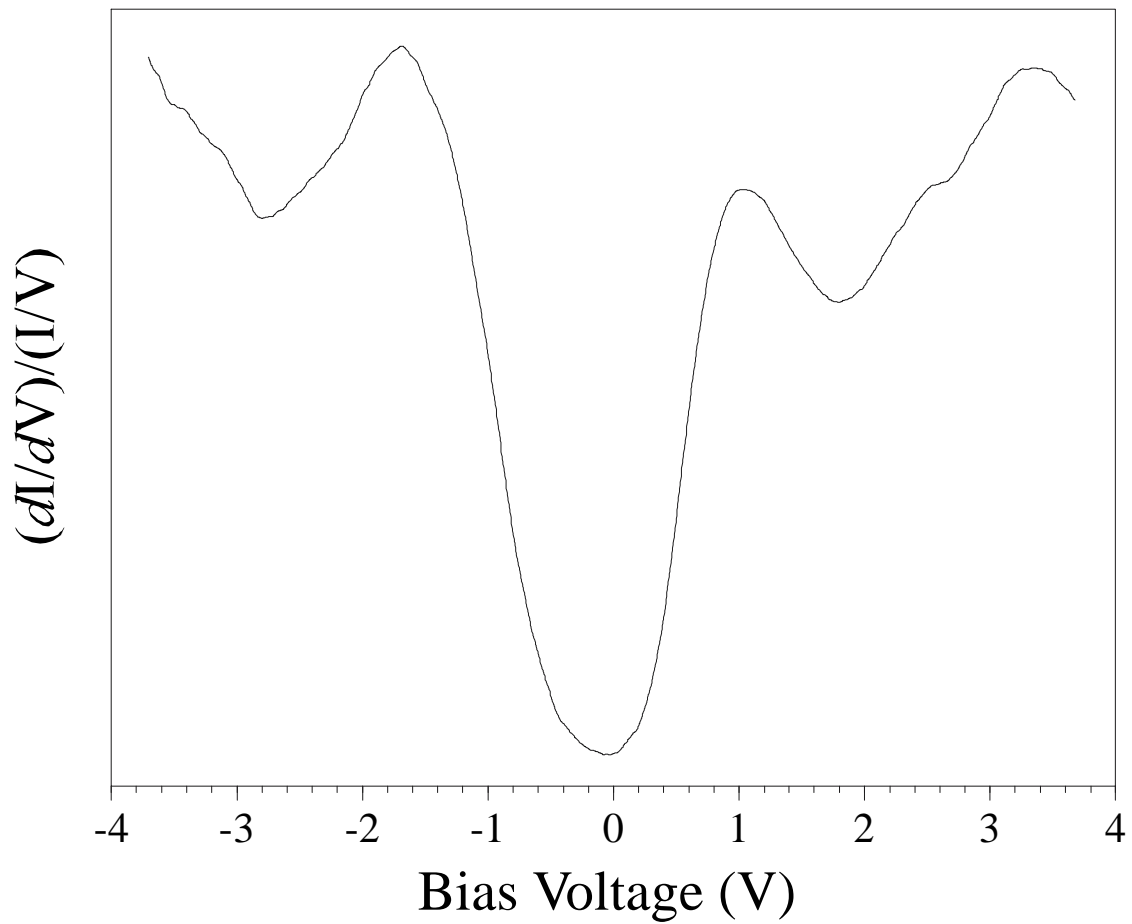


Figure 16: Area-averaged normalized  $(dI/dV)/(I/V)$  tunneling spectrum collected over a random distribution of points on in-vacuum cleaved pyrite. The spectrum is the average of 90 spectra collected with two separate W tips.

surface sites. For pyrite, unfortunately the optimal tunneling conditions for collecting atomically resolved images and that for wide dynamic range tunneling spectra are very different. Because of this, and because we could not implement the varying-gap method (see Methods section above), we collected tunneling spectra independent of atomically resolved images.

It should also be pointed out that collection of meaningful single-point spectra on freshly cleaved pyrite in UHV proved to be very difficult and only in the rarest cases were we able to attain stable tunneling contact during  $I(V)$  collection giving a high signal-to-noise ratio. Successful spectra collected were generally one of two types. Representative ones are shown in Figure 17a. The spectra show that the maximum intensity at the top of the valence is at approximately -0.8 or -2.0 eV, and the maximum intensity at the bottom of the conduction band is at 1.2 or 1.6 eV. The density of states near the Fermi level and the locations of the band edges are better represented by the single point spectra compared to the area-averaged spectrum, but they are still subject to the same difficulties as discussed above. Based on the STM imaging results and the insight provided by the *ab-initio* calculations indicating the presence of surface states localized on Fe, it can be asserted that the spectra showing a prominent peak at -0.8 eV (smaller surface gap) are probably collected over surface Fe sites (high tunneling current sites) and the spectra showing a prominent peak at -2 eV (larger surface gap) must be collected over  $S_2$  sites (low tunneling current sites).

The site-specific state density distributions elucidated by the single-point spectra are consistent with the STM observations in several ways. The filled component of the dangling bond states is the primary source of state density, and therefore tunneling current, on the order of bond lengths away from the surface, at negative bias voltage. Because electrons populating these states have the longest decay lengths and, at negative bias, the transmission probability is highest for states closest to the Fermi level of the sample (Hamers, 1993), they should dominate

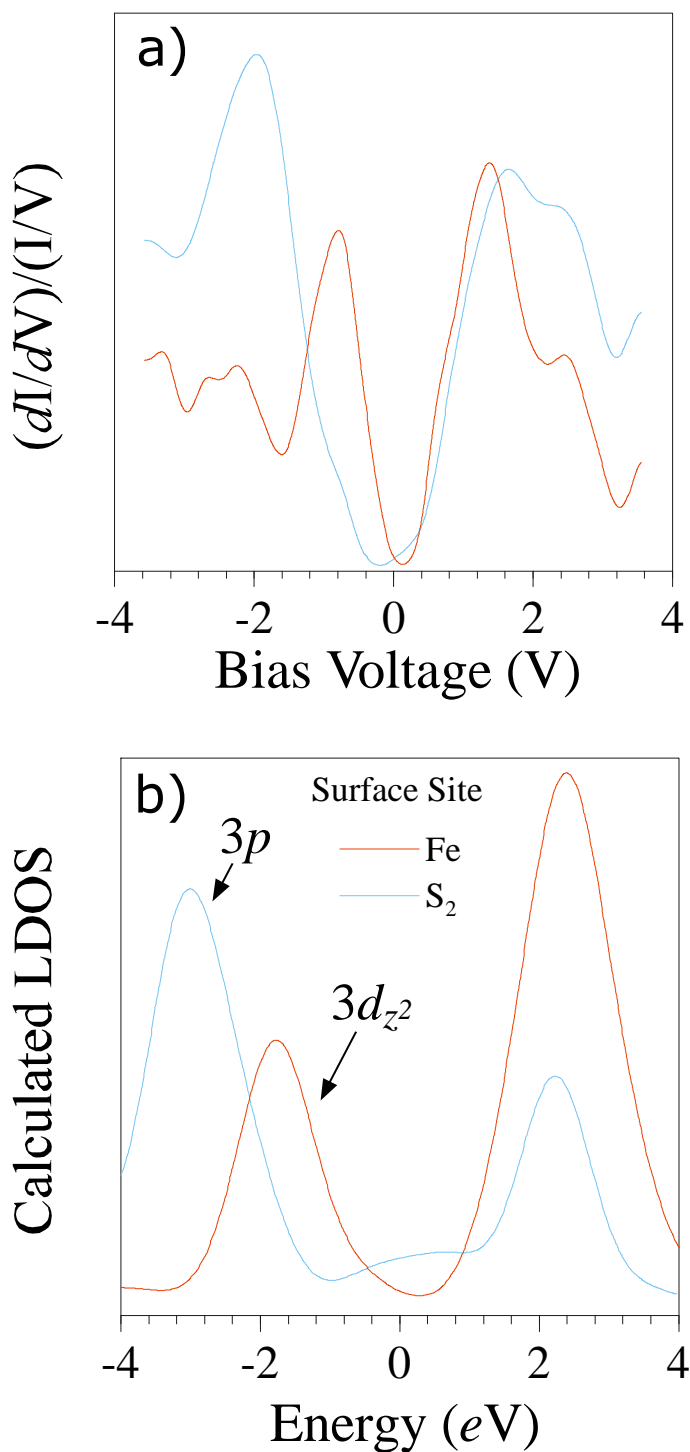


Figure 17: Single-point normalized  $(dI/dV)/(I/V)$  tunneling spectra collected on a pristine pyrite surface (a), and calculated local densities of states (LDOS) for tip positions over surface sites (b). Contributions to the LDOS over surface Fe and  $S_2$  sites originate primarily from Fe  $3d_{z^2}$  - like dangling bond states and S  $3p$  states, respectively.

the tunneling current at any negative bias voltage. Indeed, all the successful atomically resolved STM images collected in this study showed a face centered cubic arrangement of high tunneling current sites consistent with Fe sites. Along those same lines, it should be noted that one would not expect "contrast reversal" in the STM images at negative bias even though the LDOS over S sites becomes greater than that for Fe deeper in the valence band (Fig. 17a). However, at positive bias, the source of long decay length electrons is derived from the narrow portion of the top of the tip valence band (0 - ~ 0.3 eV (Hamers, 1993)) which probe unoccupied electronic states of the sample. This leads to somewhat higher resolution at positive sample bias than for negative (Hamers, 1993). Based on the single-point spectra, one could expect to see contrast reversal at high positive bias ( $\sim > +2$  V), where S sites should become brighter than Fe sites. Unfortunately, attempts to confirm this assertion have been unsuccessful so far.

The STM images are conclusive, though, on the point that the lowest energy unoccupied states are localized on Fe sites. This is a imaging result that is not readily revealed in the tunneling spectra due to the poor behavior of the  $(dI/dV)/(I/V)$  conversion near the Fermi level as previously discussed. The observation that the difference in the density of unoccupied states between Fe and S sites is small higher into the conduction band may explain the difficulties in achieving atomic resolution images higher at positive bias (up to  $\sim 1.2$  V). Atomic imaging requires significant tunneling current contrast between sites (Chen, 1993), as would not be the case for positive bias voltages in the vicinity of  $\sim +1$  V.

### Calculated Local Densities of States

For comparison with the experimental spectra, we calculated the LDOS for points positioned over Fe and S<sub>2</sub> dimer sites using GAUSSIAN94, and also calculated projected LDOS using atomic orbitals which could contribute to state density near the Fermi level (Fe 3d, S 3p) (Fig. 17b). It should be noted that calculations of the type used here often overestimate the band gap due to difficulties in the estimation of the energy attributed to correlation interaction

between electrons. Although the peak positions in the calculated LDOS are shifted, there are remarkable similarities with the experimental spectra. Both show a narrower gap over Fe sites, a 1.2 eV difference between the maxima for the top of the valence band over Fe vs. S sites, and that the bottom of the conduction band is at similar energies for both surface sites. Again it is interesting to note that this last observation provides an explanation for the fact that STM imaging at atomic resolution on pyrite is more difficult in UHV at positive bias voltage as opposed to negative.

The LDOS projected onto Fe  $3d$  and S  $3p$  orbitals show that, at surface Fe sites, the highest energy filled state is predominantly due to a  $3d_{z^2}$  - like dangling bond, and the conduction band minimum at the surface is due to antibonding Fe  $3d_{z^2}$  - S  $3p$  states. For the S states, which are not energetically displaced at the surface, this is consistent with the recent theoretical study showing that the bulk conduction band minimum consists of significant contributions from S  $3p$  orbitals (Evert *et al.*, 1998). The S site LDOS is composed of entirely S  $3p$  states on both sides of the Fermi level within the energy range shown. Non-bonding Fe  $3d$  states do not contribute significantly to the LDOS over surface Fe sites. However, they make small contributions for tip positions slightly displaced along surface Fe-Fe directions. This is consistent with the fact that the non-bonding orbitals are oriented along body diagonals of the unit cell and do not project perpendicular to the plane of the surface. In light of this, the smaller peaks which are observed in the experimental spectrum for surface Fe sites at  $\sim -2.4$  eV (Fig. 17a) may be derived from non-bonding Fe  $3d$  states, given the reasonable assumption that the spectrum was collected slightly off-center over an Fe site.

### **Beam-Induced Surface Alteration**

During the early stages of the UHV STM/STS experiments in this research, it became apparent that the tunneling spectroscopic behavior showed a dependence on whether or not the STM chamber was illuminated. It was discovered that incandescent light from a fiber optic

W-filament lamp could modify the  $I(V)$  behavior of the tunneling contact (Fig. 18). Illuminated, freshly cleaved samples tended to show more ohmic behavior with a more rapid rise in tunneling current as a function of bias voltage, especially for the positive bias ramp. Pyrite is well known to be photoactive, the effects of which can significantly alter the chemical behavior of its surfaces (Ennaoui *et al.*, 1986; Jaegermann and Tributsch, 1988; Schubert and Tributsch, 1990; Mishra and Osseo-Asare, 1992; Bronold *et al.*, 1994a). Previous work in this area has addressed the physical aspects of this photo-induced effect so a discussion here is not warranted. However, a related phenomenon was encountered that has not been previously discussed. It was found that the surface conductivity of in-vacuum cleaved pyrite {100} is altered by exposing the surface to UV light, as would be used for UPS measurements. The behavior was assessed during attempts to engage and image surfaces that had been previously analyzed using He I UPS. Establishing tunneling contact with such surfaces, usually using a bias voltage of +1 V and a setpoint current of 1 nA, repeatedly resulted in tip crashes, on samples that had been successfully imaged before they were irradiated with UV light. Similar behavior was observed for samples that had been exposed to Al  $K\alpha$  x-rays for XPS, and low-energy electron beams for LEED, except to a lesser degree. The tip would engage these surfaces, but the tunneling contact was invariably unstable which precluded the collection of high quality images. This effect is perhaps related to the experimental observation that the quality of LEED images would degrade in a matter of minutes after exposing the surface to the electron beam, which is not an uncommon behavior (Brundle, 1974). LEED images of the "altered" surface were qualitatively indistinguishable from the non-irradiated surface, so we suggest that the effect is purely electronic, with possible ties to changes in the energy and occupation of surface states due to photo-induced production of electron-hole pairs and charge trapping/de-trapping (Jaegermann and Tributsch, 1988; Osseo-Asare, 1993). We did not attempt to quantify this behavior for the purposes of this study, nor is it known whether or not this effect is reversible. At this point, we only suggest that such behavior is noteworthy and that it has obvious implications for future UHV surface studies of pyrite.

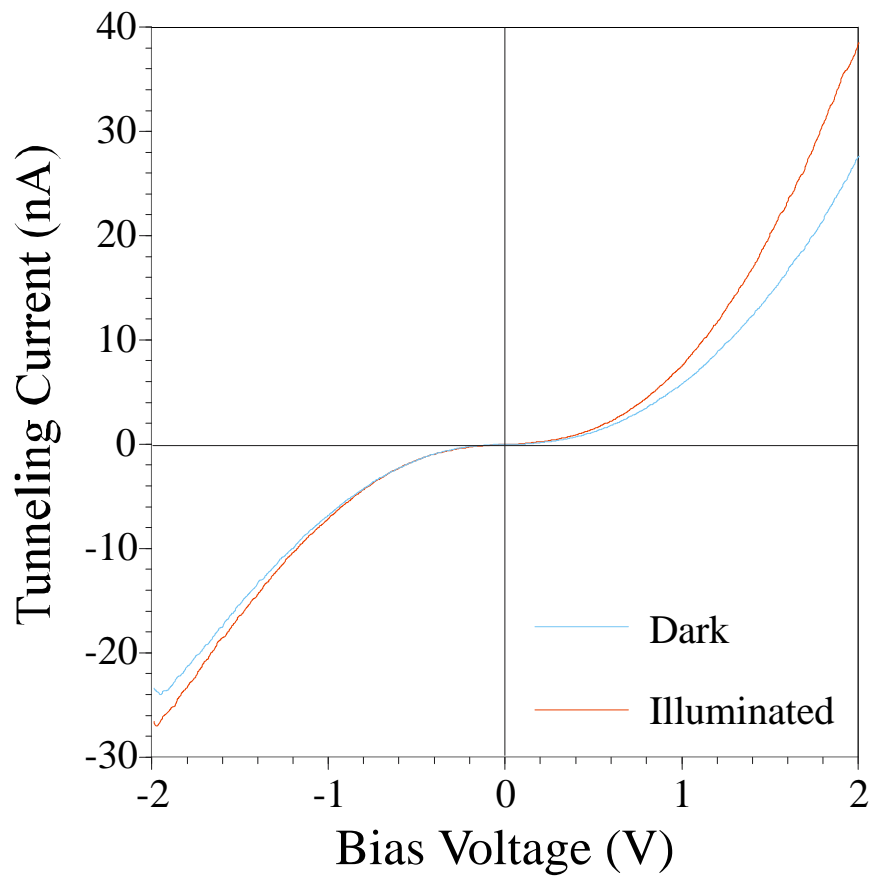


Figure 18: Area-averaged I(V) tunneling spectra collected on in-vacuum cleaved pyrite comparing the tunneling current response in the dark vs. illuminated conditions. Each spectrum is the average of 25 curves collected with a PtIr tip.

## SUMMARY

Collectively, the combined experimental and theoretical approach has provided new insight into the atomic and electronic structure of pyrite {100} surfaces. The surface structure is unreconstructed and well described as a simple termination of the bulk. The near-Fermi level electronic structure is primarily composed by Fe 3d dangling bond states. Normalized tunneling spectra are in good agreement with the UPS spectra. Normalized single-point tunneling spectra reveal localized state density differences between atomic sites on the surface, which are interpreted using *ab-initio* calculations of the surface LDOS. The occupied component of the surface state localized on Fe is clearly expressed in the single-point spectra. As it is the highest energy filled state at the surface, it is the most energetically favored source of electrons for oxidative attack by a sorbed species. The fact that surface states are present in the bulk band gap can significantly reduce activation energy barriers for electron transfer to redox couples interacting with surface Fe sites. At the same time, the dual mode STM results indicate that the lowest unoccupied states are also localized on Fe sites. This suggests that surface Fe sites are also favored for sorption of electron donor species. The fact that the surface electronic structure is dominated by dangling bond states means that at least the initial interactions between sorbing species and the surface will be driven by the quenching of high energy surface states at Fe sites. A companion paper follows on the interaction of these surfaces with H<sub>2</sub>O-O<sub>2</sub> mixtures (Rosso *et al.*, submitted).

## REFERENCES CITED

Bader, R.F.W (1990) *Atoms in molecules: A quantum theory*, 438 p. Oxford Science Publications, Oxford.

- Bakken, B.M., Hochella, M.F., Jr., Marshall, A.F., and Turner, A.M. (1989) High resolution microscopy of gold in unoxidized ore from the Carlin mine, Nevada. *Economic Geology*, 84, 171-179.
- Becke, A.D. (1988) Density-functional exchange-energy approximation with correct asymptotic behavior. *Physical Review A*, 38, 3098-3100.
- Becker, U., and Hochella, M.F., Jr. (1996) The calculation of STM images, STS spectra, and XPS peak shifts for galena: New tools for understanding mineral surface chemistry. *Geochimica et Cosmochimica Acta*, 60, 2413-2426.
- Bocquet, A.E., Mamiya, K., Mizokawa, T., Fujimori, A., Miyadai, T., Takahashi, H., Mōri, M., and Suga, S. (1996) Electronic structure of 3d transition metal pyrites  $MS_2$  (M=Fe, Co, or Ni) by analysis of the M 2p core-level photoemission spectra.
- Boyd, R., Knop, O., and Choi, S.C. (1988) *Journal of the American Chemical Society*, 110, 7299.
- Bullett, D.W. (1982) Electronic structure of 3d pyrite- and marcasite-type sulphides. *Journal of Physics C*, 15, 6163-6174.
- Bronold, M., Pettenkofer, C., and Jaegermann, W. (1994a) Surface photovoltage measurements on pyrite (100) cleavage planes: Evidence for electronic bulk defects. *Journal of Applied Physics*, 76, 5800-5808.
- Bronold, M., Tamm, Y., and Jaegermann, W. (1994b) Surface states on cubic d-band semiconductor pyrite ( $FeS_2$ ). *Surface Science Letters*, 314, L931-L936.
- Calmano, W., Förstner, U., and Hong, H. (1994) Mobilization and scavenging of heavy metals following resuspension of anoxic sediments from the Elbe river. In *American Chemical Society Symposium Series*, 550, 298-321.

- Charnock, J.M., Henderson, C.M.B., Mosselmans, J.F.W., and Patrick, R.A.D. (1996) 3d transition metal L-edge X-ray absorption studies of the dichalcogenides of Fe, Co, and Ni. *Physics and Chemistry of Minerals*, 23, 403-408.
- Chen, C.J. (1993) *Introduction to scanning tunneling microscopy*, 412 p. Oxford Science Publications, Oxford.
- Dovesi, R., Saunders, V.R., Roetti, C., Causà, M., Harrison, N.M., Orlando, R., and Aprà, E. (1996) *CRYSTAL95 user's manual*, 170 p. University of Torino, Torino.
- Eggleston, C.M. (1994) High resolution scanning probe microscopy: Tip-surface interaction, artifacts, and applications in mineralogy and geochemistry. In *Clay Minerals Society Workshop Lectures*, 7, 1-90.
- Eggleston, C.M., Ehrhardt, J.-J., and Stumm, W. (1996) Surface structural controls on pyrite oxidation kinetics: An XPS-UPS, STM, and modeling study. *American Mineralogist*, 81, 1036-1056.
- Eggleston, C.M., and Hochella, M.F., Jr. (1990) Scanning tunneling microscopy of sulfide surfaces. *Geochimica et Cosmochimica Acta*, 54, 1511-1517.
- Eggleston, C.M., and Hochella, M.F., Jr. (1992) Scanning tunneling microscopy of pyrite {100}: Surface structure and step reconstruction. *American Mineralogist*, 77, 221-224.
- Ennaoui, A., Fiechter, S., Jaegermann, W., and Tributsch, H. (1986) Photoelectrochemistry of highly quantum efficient single-crystalline *n*-FeS<sub>2</sub> (pyrite). *Journal of the Electrochemical Society*, 133, 97-106.
- Evert, V., Hock, K.-H., Fiechter, S., and Tributsch, H. (1998) Electronic structure of FeS<sub>2</sub>: The crucial role of electron-lattice interaction. *Physical Review B*, 57, 6350-6359.
- Fan, F.-R., and Bard, A.J. (1991) Scanning tunneling microscopy and tunneling spectroscopy of *n*-type iron pyrite (*n*-FeS<sub>2</sub>) single crystals. *Journal of Physical Chemistry*, 95, 1969-1976.

- Feenstra, R.M., Stroscio, J., and Fein, A., (1987) Tunneling spectroscopy of the Si (111)  $2 \times 1$  surface. *Surface Science*, 181, 295-306.
- Feenstra, R.M. (1994) Tunneling spectroscopy of the (110) surface of direct-gap III-V semiconductors. *Physical Review B*, 50, 4561-4570.
- Ferrer, I.J., Nevskaja, D.M., de las Heras, C., and Sánchez, C. (1990) About the band gap nature of FeS<sub>2</sub> as determined from optical and photo-electrochemical measurements. *Solid State Communications*, 74, 913-916.
- Feynman, R.P. (1939) Forces in molecules. *Physical Review*, 56, 340-343.
- Folmer, J.C.W., Jelinek, F., and Calis, G.H.M. (1988) The electronic structure of pyrites, particularly CuS<sub>2</sub> and Fe<sub>1-x</sub>CuSe<sub>2</sub>: An XPS and Mossbauer study. *Journal of Solid State Chemistry*, 72, 137-144.
- Frisch, M.J., Trucks, G.W., Schlegel, H.B., Gill, P.M.W., Johnson, B.G., Robb, M.A., Cheeseman, J.R., Keith, T.A., Petersson, G.A., Montgomery, J.A., Raghavachari, K., Al-Laham, M.A., Zakrzewski, V.G., Ortiz, J.V., Foresman, J.B., Cioslowski, J., Stefanov, B.B., Nanayakkara, A., Challacombe, M., Peng, C.Y., Ayala, P.Y., Chen, W., Wong, M.W., Andres, J.L., Replogle, E.S., Gomperts, R., Martin, R.L., Fox, D.J., Binkley, S., Defrees, D.J., Baker, J., Stewart, J.J.P., Head-Gordon, M., Gonzalez, C., and Pople, J.A. (1995) *Gaussian 94 (Revision C.2)* Gaussian, Inc., Pittsburgh PA.
- Fuji *et al.* (1986) High pressure compressibilities of pyrite and catterite. *Mineralogical Journal of Japan*, 13, 202-211.
- Gatti, C. (1997) *TOPOND96 User's Manual*, 15 p. CNR-CSR SRC Milano, Italy.
- Hamers, R.J. (1993) Methods of tunneling spectroscopy with the STM. In D.A. Bonnell, Ed., *Scanning tunneling microscopy and spectroscopy: Theory, techniques, and applications*, p. 51-103. VCH, New York.

- Hansma, P. (1982) Tunneling spectroscopy: Capabilities, applications, and new techniques, 493 p., Plenum, New York.
- Hiskey, J.B., and Schlitt, W.J. (1981) Aqueous oxidation of pyrite. In Proceedings of the 2<sup>nd</sup> SME-SPE International Solution Mining Symposium, Denver CO, 55-74.
- Hochella M.F., Jr., (1990) Atomic structure, microtopography, composition, and reactivity of mineral surfaces. In Mineral-water interface geochemistry, Reviews in Mineralogy, 23, 87-132.
- Hochella M.F., Jr., Rakovan J.F., Rosso K.M., Bickmore B.R., and Rufe E. (in press) New directions in mineral surface geochemical research using scanning probe microscopes. American Chemical Society Special Volume
- Huang, Y.S., Huang, J.K., and Tsay, M.Y. (1993) An electrolyte electroreflectance study of FeS<sub>2</sub>. Journal of Physics: Condensed Matter, 5, 7827-7836.
- Hyland, M.M., and Bancroft, G.M. (1989) An XPS study of gold deposition at low temperatures on sulphide minerals: Reducing agents. Geochimica et Cosmochimica Acta, 53, 367-372.
- Jaegermann, W., and Tributsch, H. (1988) Interfacial properties of semiconducting transition metal chalcogenides. Progress in Surface Science, 19, 1-167.
- Jambor, J.L., and Blowes, D.W. (1994) Short course handbook on environmental geochemistry of sulfide mine-wates, 438 p. Mineralogical Association of Canada.
- Jean, G.E., and Bancroft, G.M. (1985) An XPS and SEM study of gold deposition at low temperature on sulphide minerals. Geochimica et Cosmochimica Acta, 49, 979-987.
- Lee, C., Yang, W., and Parr, R.G. (1988) Development of the Colle-Salvetti correlation-energy formula into a functional of the electron density. Physical Review B, 37, 785-789.
- Li, E.K., Johnson, K.H., Eastman, D.E., and Freeouf, J.L. (1974) Localized and bandlike valence electron states in FeS<sub>2</sub> and NiS<sub>2</sub>. Physical Review Letters, 32, 470-472.

- Lowson, R.T. (1982) Aqueous oxidation of pyrite by molecular oxygen. *Chemical Reviews*, 82, 461-497.
- Mårtensson, P., and Feenstra, R.M. (1989) Geometric and electronic structure of antimony on the GaAs (110) surface studied by scanning tunneling microscopy. *Physical Review B*, 7744-7753.
- Mishra, K.K., and Osseo-Asare, K. (1992) Fermi-level pinning at pyrite (FeS<sub>2</sub>)/electrolyte junctions. *Journal of the Electrochemical Society*, 139, 749-752.
- Moore, J.N., and Luoma, S.N. (1990) Hazardous wastes from large-scale metal extraction. *Environmental Science and Technology*, 24, 1278-1285.
- Mosselmans, J.F.W., Patrick, R.A.D., van der Laan, G., Charnock, J.M., Vaughan, D.J., Henderson, C.M.B., and Garner, C.D. (1995) X-ray absorption near-edge spectra of transition metal disulfides FeS<sub>2</sub> (pyrite and marcasite), CoS<sub>2</sub>, NiS<sub>2</sub>, and CuS<sub>2</sub>, and their isomorphs FeAsS and CoAsS. *Physics and Chemistry of Minerals*, 22, 311-317.
- Nash J. T., Granger H. C., and Adams S. S. (1981) Geology and concepts of important types of uranium deposit. *Economic Geology*, 75th Anniversary Volume, 63-116.
- Nimick, D.A., and Moore, J.N. (1994) Stratigraphy and chemistry of sulfidic flood-plain sediments in the Upper Clark Fork Valley, Montana. In *American Chemical Society Symposium Series*, 550, 276-288.
- Nordstrom K. D. (1982) Aqueous pyrite and the consequent formation of secondary minerals. In *Acid Sulfate Weathering: Pedogeochemistry and Relationship to Manipulation of Soil Materials: Madison, Wisconsin* (ed. J. A. Kittrick, D. S. Fanning, and L. R. Hossner), pp. 37-56. Soil Science Society of America Press.
- Ogawa, S., Waki, S., and Teranishi, T. (1974) Magnetic and electrical properties of 3d transition-metal disulfides having the pyrite structure. *International Journal of Magnetism*, 5, 349-360.

- Osseo-Asare, K. (1993) Pyrite in aqueous systems: Semiconductor properties, oxidative dissolution, and environmental control. In First International Conference on Processing Materials for Properties, The Minerals, Metals & Materials Society.
- Pettenkofer, C., Jaegermann, W., and Bronold, M. (1991) Site specific surface interaction of electron donors and acceptors on FeS<sub>2</sub> (100) cleavage planes. *Berichte der Bunsen-Gesellschaft für Physikalische Chemie*, 95, 560-565.
- Pisani, C. (1996) Quantum-mechanical ab-initio calculation of the properties of crystalline materials, 327 p., Springer-Verlag, Berlin.
- Pridmore, D.F., and Shuey, R.T. (1976) The electrical resistivity of galena, pyrite, and chalcopyrite. *American Mineralogist*, 61, 248-259.
- Schlegel, A., and Wachter, P. (1976) Optical properties, phonons and electronic structure of iron pyrite (FeS<sub>2</sub>). *Journal of Physics C*, 9, 3363-3369.
- Seah, M.P., and Dench, W.A., (1979) Quantitative electron spectroscopy of surfaces: A standard data base for electron mean free paths in solids. *Surface and Interfacial Analysis*, 1, 2-11.
- Siebert, D., and Stocker, W. (1992) Investigation of a (100) surface of pyrite by STM. *Physica Status Solidi A*, 134, K17-K20.
- Starling, A., Gilligan, J.M., Carter, A.H.C., Foster, R.P., and Saunders, R.A. (1989) High-temperature hydrothermal precipitation of precious metals on the surface of pyrite. *Nature*, 340, 298-300.
- Van der Heide, H., Hemmel, R., van Bruggen, C.F., and Haas, C. (1980) X-ray photoelectron spectra of 3d transition metal pyrites. *Journal of Solid State Chemistry*, 33, 17-25.

## **Chapter Three**

### ***The Interaction of Pyrite {100} Surfaces with O<sub>2</sub> and H<sub>2</sub>O: Fundamental Oxidation Mechanisms***

#### **INTRODUCTION**

The geochemical, environmental, and technological significance of pyrite oxidation has resulted in many studies devoted to understanding this oxidation process. Low temperature aqueous solution experiments (Goldhaber, 1983; McKibben, 1984; Wiersma and Rimstidt, 1984; McKibben and Barnes, 1986; Moses *et al.*, 1987; Nicholson *et al.*, 1988; Moses and Herman, 1991; Williamson and Rimstidt, 1994) collectively have unraveled the general principles of the overall mechanism. One of the most notable characteristics of pyrite oxidation is that, in the end products, only sulfur is oxidized, whereas iron is ferrous in both the crystal and as a dissolved species in solution. The stepwise oxidation of sulfur from a -1 state in pyrite disulfide to a +6 state in sulfate involve very fast reactions and thus attempts to understand the sequential oxidation of sulfur have met with little success. Various sulfoxy species have been detected in solution in small quantities. However, the low concentration and the lability of these intermediate sulfur species make their analysis difficult. Important contributions to our understanding of this problem were provided from stable isotope tracer studies (Taylor *et al.*, 1984; Reedy *et al.*, 1991) which showed that oxygen in the end product SO<sub>4</sub><sup>2-</sup> is dominantly derived from H<sub>2</sub>O; both pH and temperature have minimal effects on this outcome. This means that dissociated H<sub>2</sub>O species play a key role as reactants in the overall oxidation process and any mechanistic model must take this into account.

The development of our understanding of individual reaction mechanisms at the pyrite surface has been based largely on surface analytical approaches. Several studies have been devoted to the oxidation of pyrite in air, most of which have relied heavily on X-ray

photoelectron spectroscopy (XPS) data (Buckley and Woods, 1987; Mycroft *et al.*, 1990; Karthe *et al.*, 1993; Nesbitt and Muir, 1994). Collectively, the results indicate that the initial air oxidation products are iron oxides and/or hydroxides, followed by iron sulfate, and finally an iron-deficient sulfide layer. The question then remains as to how these products form and why.

To begin to answer this question requires experimental observations of these reactions as they occur at the atomic scale. Studies at this scale are few (Eggleston, 1994; Eggleston *et al.*, 1996) but have given us a great deal of insight into site-specific oxidation reactions. STM observations of pyrite oxidizing in air show the initial development of oxidation products across the surface and the participation of iron states in oxidation (Eggleston *et al.*, 1996). However, our understanding of the fundamental oxidation reactions is restricted because of the lack of experimental techniques where surface-sensitive microscopic and spectroscopic observations of the oxidation process can be constrained with a suitable level of chemical isolation. Our capability to surmount these obstacles has been realized with the use of the scanning tunneling microscope when it is used in conjunction with standard ultra-high vacuum (UHV) systems. This experimental setup provides an opportunity for detailed examination of the surface and the fundamental surface reactions involved in the initial stages of pyrite oxidation. At the same time, chemical interpretations of tunneling microscopic and spectroscopic data are not unambiguous without supporting insight that can only be derived from theoretical calculations. This combined experimental and theoretical approach has been previously applied to a study of the electronic structure of pyrite surfaces (Rosso and Hochella, submitted). In this study, this combined approach is used to further develop our understanding of pyrite surface reactivity by investigating its interaction with O<sub>2</sub>, H<sub>2</sub>O, and mixtures thereof.

## METHODS

### Principal Instrumentation and Samples

Scanning tunneling microscopy (STM), scanning tunneling spectroscopy (STS), ultraviolet photoelectron spectroscopy (UPS), and low energy electron diffraction (LEED) were performed in a OMICRON compact UHV lab operating at a base pressure of  $1 \times 10^{-10}$  mbar. The main chamber is equipped with a dual anode (Al,Mg) x-ray source, UV lamp, ion gun, a reverse view LEED with a 1 keV electron gun, cylindrical sector electron energy analyzer, and a sample heater capable of heating to 750 °C. Natural pyrite single crystal cubes from Logroño, Spain were obtained from the Museum of Geological Sciences at Virginia Tech. The samples were cut into approximately  $5 \times 5 \times 10$  mm oriented prisms with faces parallel to the cubic axes. Samples showing any visible inclusions were discarded. The prisms were slightly notched to control the fracture propagation. The samples were mechanically mounted in custom stainless steel stubs and cleaved using an in-house built cleavage stage in the load-lock chamber, which is turbo-pumped to better than  $1 \times 10^{-7}$  mbar. Pyrite crystals cleaved in the load-lock chamber were transferred to the lower base pressure of the main chamber (low  $10^{-10}$  mbar range) in less than 30 seconds.

### Gas Dosing

The system is equipped with an in-house built gas leak manifold for controlled gas bleeds to various parts of the main chamber. Pure H<sub>2</sub>O vapor was prepared starting from de-ionized water in a fused quartz thimble attached to the gas introduction manifold. The water was purged of dissolved atmospheric gases by three cycles of freezing, pumping off the residual vapor, and then thawing. High purity O<sub>2</sub> (99.99%) was used for oxygen dosing experiments. Mixtures of O<sub>2</sub>-H<sub>2</sub>O were prepared in the gas introduction manifold prior to dosing by filling a closed section with the equilibrium vapor pressure of water at room temperature, and then introducing and adjusting the O<sub>2</sub> pressure until the desired mole ratio was reached. The total gas pressure was measured using a capacitance manometer and the gas composition was

estimated using ideal gas relationships. The gases were introduced to the main analytical chamber through a precision leak valve and the pressure was monitored using an ionization gauge. Typical dosing pressures were in the high  $10^{-8}$  to the low  $10^{-7}$  mbar range. The gas exposure was recorded in units of Langmuir ( $1\text{L} = 1.33 \times 10^{-6}$  mbar · sec) by integrating the pressure vs. time curve.

### **X-ray Photoelectron Spectroscopy**

XPS analyses were performed using a Perkin-Elmer 5400 equipped with a concentric hemispherical analyzer with a resolution of 0.9 eV as determined using the Ag  $3d_{5/2}$  line, dual anode (Al, Mg) X-ray source, and a base pressure of  $1 \times 10^{-8}$  mbar. Mg K $\alpha$  X-rays were used, and photoelectrons were collected at 45 degrees. High purity O<sub>2</sub> (99.99%) introduced through a precision leak valve was used for oxygen dosing experiments.

### **Ultra-violet Photoelectron Spectroscopy**

UPS spectra were collected using He I (21.2 eV) radiation and a pass energy of 10 eV. The sample surface was oriented normal to the lens axis of the analyzer. The sample stubs, the outer surface of the pyrite prism, and the notches in the prisms used in the UPS experiments were sputter coated with a visible layer of Au to isolate the Fe spectral data to that coming from the cleaved surface. Because UV radiation has been shown to alter pyrite surfaces to a non-conducting state (Rosso and Hochella, submitted), spectra were collected on individual samples that had been previously exposed to the gas(es) of interest but not to UV light. Samples exposed to UV radiation were subsequently found to be unusable for surface reaction studies. The absolute binding energy scale of the UPS spectra was referenced to the sample Fermi level, which was determined by subtracting 21.2 eV from the low kinetic energy photoelectron cutoff energy and adding the workfunction of the spectrometer. The low kinetic energy edge was designated at the energy half way between the 16% and 84% count rate levels

at the cutoff. The workfunction of the spectrometer is based on the measured position of the Ag  $3d_{5/2}$  photo peak.

### **Low Energy Electron Diffraction**

LEED patterns were acquired using 4-grid reverse view LEED optics (OMICRON) at beam energies between 70 - 300 eV. The electron gun has a spot size of approximately 1 mm. Patterns were collected immediately after turning up the beam energy because patterns collected on both in-vacuum cleaved and gas-dosed surfaces were found to degrade in a few minutes.

### **Scanning Tunneling Microscopy and Spectroscopy**

For STM experiments, tips were prepared by electrochemically etching W wire in 1 M KOH. Surfaces with large, flat terraces were targeted for atomic-scale imaging. Samples and tips were stored under base pressure in a carousel attached to the main chamber. Samples were shielded from light during all STM imaging and tunneling spectra data collection. All STM/STS data were collected at room temperature. Atomic scale images were processed using band pass FFT filtering to remove noise. Frequencies pertaining to atomic periodicity and low frequencies pertaining to “topographic” features were passed.

Tunneling spectra were collected on surfaces that had been incrementally dosed with oxygen. Each of the spectra on oxygen exposed surfaces represent the average of 125 curves collected over the period of 5 minutes over a  $1 \text{ nm}^2$  area on the surface, between oxygen exposures. This approach is based on the idea that, over the course of the 5 minutes, piezo-drift will cause the tip to be displaced over a random distribution of locations on the surface. At each spectroscopy point, the tip raster was paused, the feedback loop was turned off, the voltage ramp was applied, the loop was re-engaged, and imaging resumed. The time required to collect each spectrum was 63 ms including 50  $\mu\text{s}$  delays between each spectral datum to let

capacitive transients die out. Because the most successful imaging conditions were at low bias for atomically resolved images, the tip-sample distance was relatively small. Therefore, during the voltage ramp at a spectral point, the exponentially increasing tunneling current quickly saturated the current-to-voltage converter. Because of the tunneling electronics were incompatible with simultaneously adjusting the tip-sample separation during the voltage ramp, the varying-gap spectroscopic method could not be implemented (Mårtensson and Feenstra, 1989; Feenstra, 1994). This precluded the simultaneous collection of spectra with atomically resolved images, so the spectra were collected without knowledge of whether the tip was located in either an oxidized or unoxidized area of the surface. In order to collect wider dynamic range spectra, tunneling conditions were re-optimized for a large tip-sample separation specifically for spectral data collection. Using a bias voltage of 4 V and a setpoint current of 7 nA allowed a -4 to +4 V dynamic range in the voltage ramp. The raw  $I(V)$  curves were converted to  $(dI/dV)/(I/V)$  data using a least-squares moving window fit. The mathematical spike at low bias was suppressed by adding a small constant to  $I/V$  before the conversion.

### **Ab-initio Calculations**

*Ab-initio* calculations of adsorption reactions on pyrite clusters were performed using GAUSSIAN94 (Frisch *et al.*, 1995). The calculations were performed on a 27-atom stoichiometric cluster used to successfully model the pyrite {100} surface (Rosso and Hochella, submitted). An electron core pseudopotential basis set known as SBKJC VDZ ECP was chosen for both Fe (Stevens *et al.*, 1992) and S (Stevens *et al.*, 1984). Regarding the iron basis set, several minor modifications were made. The most diffuse (exponent 0.04) *sp* function was removed to save unwarranted computational expense and the exponents of the most diffuse *sp* and *d* functions were energy optimized simultaneously. The optimal exponent for these gaussian functions was 0.161 which was similar to the original 0.1213 (*sp*) and 0.1382 (*d*). For oxygen and hydrogen, a standard LANL2DZ ECP basis set was used. The calculations were performed at

the unrestricted Hartree-Fock level of theory. Geometry optimizations of the full cluster have demonstrated the stability of the structure and a resistance to significantly reconstruct, in agreement with the known surface structure (Pettenkofer *et al.*, 1991; Rosso and Hochella, submitted). Therefore, for purposes of reducing computational costs, geometry optimizations in this study were restricted to the position of the adsorbate molecule with respect to the fixed cluster coordinates.

## RESULTS / DISCUSSION

### Photoelectron Spectroscopy / LEED

He I UPS valence band spectra of pyrite {100} exposed to O<sub>2</sub>, H<sub>2</sub>O, mixtures of O<sub>2</sub>/H<sub>2</sub>O, and air were collected to observe changes in the valence band structure of the surface. Samples exposed to pure O<sub>2</sub> show a progressive oxidation and an apparent passivation towards oxidation by approximately 20 L exposure. The oxidation of the surface is generally manifested as a decrease in the density of filled states near the top of the valence band and a concomitant appearance of peaks deeper in the valence band (Fig. 1a). These features are more clearly revealed by subtracting the spectra and plotting the difference intensity (Fig. 1b). In the negative intensity region of the difference spectra, it can be seen that the decrease in the DOS at the top of the VB is focused between 0 - 5 eV binding energy and this decrease is divided into two regions by a feature which can be described as a less negative “peak” centered at about 2 eV. The DOS decrease in the lower binding energy region at about 1 eV can be attributed primarily to the oxidative consumption of a filled surface state that has Fe 3d character (Rosso and Hochella, submitted). This mid-gap state has been shown to be a dangling bond state localized on surface Fe sites that is due to the undercoordination of those Fe atoms. The loss of Fe 3d e<sub>g</sub> - S 3p bonding overlap results in a destabilization of a d<sub>z<sup>2</sup></sub>-like state at the top of the valence band. Because this is the highest energy filled state, electrons populating this state are the least tightly bound and have the longest decay lengths from the surface into the vacuum.

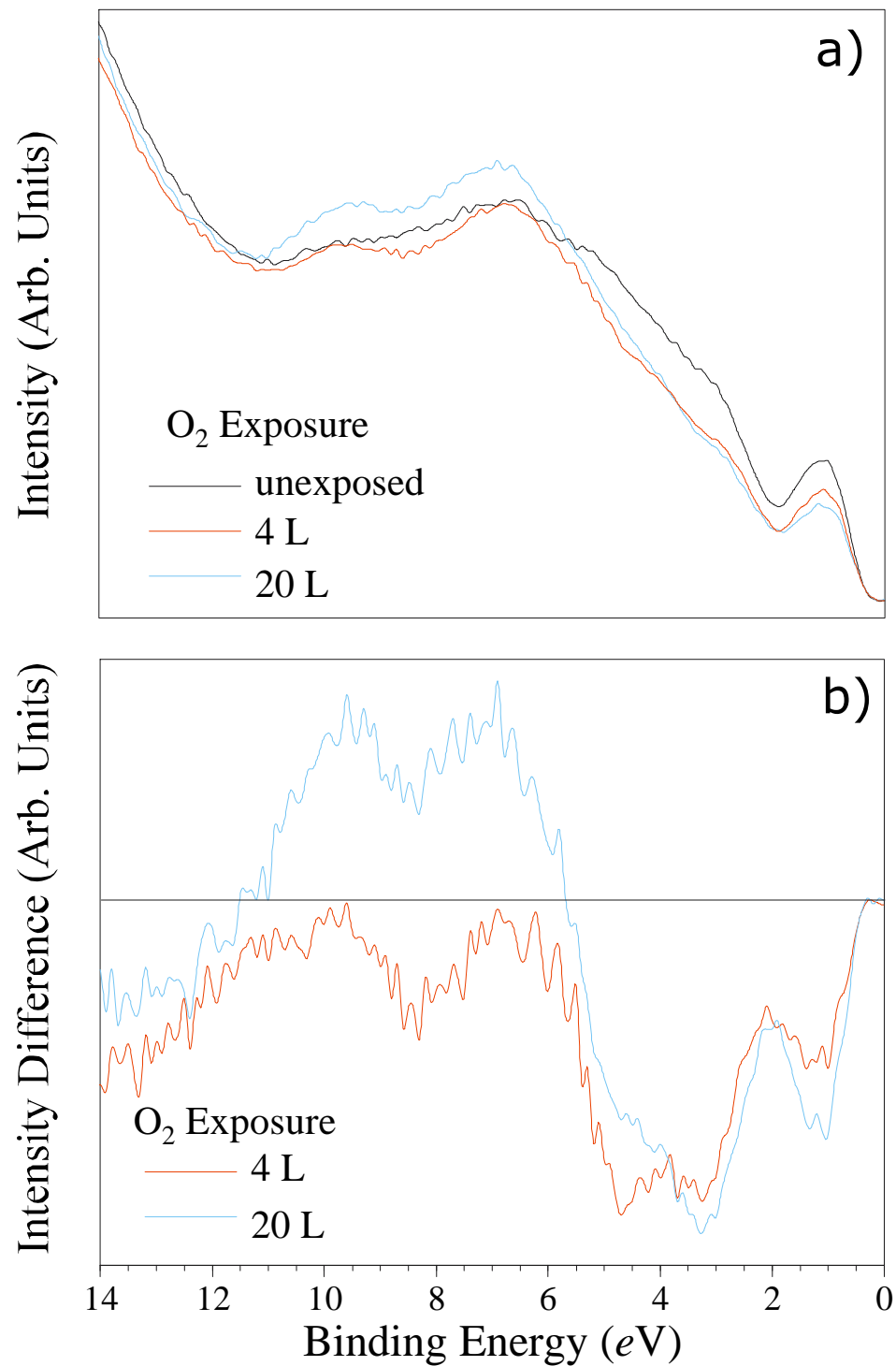


Figure 1: He I UPS valence band spectra (a), and difference spectra (b) for pristine pyrite surfaces and those exposed to O<sub>2</sub> gas. Difference spectra = reacted - pristine spectra.

At the same time, the symmetry of the  $d_{z^2}$  orbital contributing to this state is such that it projects out nearly normal to the plane of the surface, providing significant potential overlap for sigma-like interaction with a sorbing oxidant. Taken altogether, this surface state should be the primary source of electrons at the surface and should be the most reactive state towards oxidation. Based on these observations and the UPS difference spectra, we can begin to assert that incoming  $O_2$  interacts primarily with the surface state at Fe sites. In the process, sorbed O species depopulate the non-bonding Fe 3d states which are concentrated at 1 eV (Li *et al.*, 1971; Bullett, 1982; Van der Heide *et al.*, 1980; Rosso and Hochella, submitted).

The difference peak at 2 eV (Fig. 1b) represents a loss of state density which is less sensitive to the presence of sorbed O species. Calculations of the surface electronic structure using band theory predict that S 3p orbitals contribute state density over a wide range of binding energies with the highest energy S 3p states overlapping the Fe 3d non-bonding states at 1 eV (Rosso and Hochella, submitted). States that lie just below the energy of the non-bonding Fe 3d states should be primarily derived from these S 3p orbitals. This is true for bulk and surface environments as it has been shown that surface S 3p states are not energetically shifted from their bulk band energies (Rosso and Hochella, submitted). If it is assumed at this point that sorbed O species primarily depopulate Fe 3d states, then the peak shown in the UPS difference spectra at 2 eV binding energy represents surface S 3p states. This issue, however, will be developed further below.

The energy range between about 3 - 5 eV (Fig. 1b) falls within the predicted 3 -6 eV range corresponding to Fe 3d - S 3p bonding states (Rosso and Hochella, submitted). Under the same assumption as above, the depopulation of Fe 3d states would cause the loss of state density in this energy range. It was shown (Rosso and Hochella, submitted) that the loss of a coordinating S at surface Fe sites caused state density to shift from the previously bonding  $d_{z^2}$  states into the remaining bonding  $d_{x^2-y^2}$  states. The sorption of  $O_2$ -derived species at surface Fe

sites involves re-establishing a bonding interaction for the Fe  $3d_{z^2}$  state and consequently state density shifts back out of the  $d_{x^2-y^2}$  states to populate this bond.

The UPS difference spectra also show an increased DOS deeper in the valence band appearing as peaks at approximately 7 and 10 eV (Fig. 1b). These increases can be attributed to the development of new states due to chemical interaction between sorbed O species and surface Fe sites. Except in a few cases, the spectra do not, however, provide unambiguous information regarding the specific sorbed species on the surface, *i.e.*  $O_2$ ,  $O_2^-$ ,  $O^-$ , or  $O^{2-}$ . However, valence band DOS increases in the energy range indicated by the UPS difference spectra are common for sorbed O containing species on sulfides and oxides (see Brundle, 1974; Pettenkofer *et al.*, 1991; Henrich and Cox, 1994; Eggleston *et al.*, 1996). In the spectra for the pure  $O_2$  exposures, the presence of two photopeaks may possibly be a reflection of bonding overlap between the Fe dangling bond state and the  $2p_z$  orbital of oxygen at 10 eV, and the degenerate, non-bonding  $2p_x$  and  $2p_y$  oxygen orbitals at 7 eV (see Pettenkofer *et al.*, 1991). The formation of this bond comes at the expense of negative charge from the filled dangling bond on Fe.

LEED analyses of the surface structure of the in-vacuum cleaved {100} surface have been performed previously (Pettenkofer *et al.*, 1991; Rosso and Hochella, submitted). Because sorbed O species are expected to interact with surface Fe sites, one might expect such a superstructure to be evident in the LEED patterns in the case that O atoms were uniformly distributed in an “on top” geometry over Fe sites. However, the intensity and sharpness of the diffraction spots were qualitatively indistinguishable between the clean and  $O_2$  exposed surfaces (4 - 43 L  $O_2$ ).

Surfaces exposed up to 10 L of pure  $H_2O$  showed no detectable change in the valence band structure. This was not a surprising result as it has been previously shown that  $H_2O$  only

sorbs to pyrite surfaces at low temperature and desorbs at room temperature (Guevremont *et al.*, 1997; Pettenkofer *et al.*, 1991). In Pettenkofer *et al.* (1991), water physisorbed molecularly to Fe sites at 100 K and reversibly desorbed upon heating to room temperature.

Valence band spectra of surfaces exposed to certain mixtures of O<sub>2</sub> and H<sub>2</sub>O showed that the combination of the two gases most aggressively oxidized the surface. Similar changes in the valence band structure were observed for surfaces exposed to O<sub>2</sub>/H<sub>2</sub>O mixtures relative to pure O<sub>2</sub>, but more than an order of magnitude less exposure was found to produce state density losses of the same intensity (Fig. 2). Surfaces oxidized by 0.1 L of 50 mol% O<sub>2</sub> mixtures showed an equivalent reduction in state density between 0 - 5 eV as that for 20 L of pure O<sub>2</sub>. At the same time, this exposure also resulted in a more rapid build-up of state density in the energy range of 5 - 11 eV. The degree of surface oxidation due to this exposure is roughly the same as that caused by a 30 second exposure to air (uncontrolled humidity) (Fig. 2). He I photoemission from 2*p* states of chemisorbed oxygen have been documented as a broad feature at 6 eV for sorbed O on Si (111) (Wagner and Spicer, 1974) and at 7 and 11 eV for molecular H<sub>2</sub>O on TiO<sub>2</sub> (110) (Kurtz *et al.*, 1989). Pettenkofer *et al.* (1991) documented valence band peaks at 7, 10, and 13 eV for physisorbed H<sub>2</sub>O on pyrite {100}. Similar to the case for pure O<sub>2</sub> exposures, the close spacing between photopeaks derived from O 2*p* states in the binding energy range where we see DOS increases precludes the determination of the surface speciation of the adsorbate molecules. Because the distinction between the possible types of sorbed species is not explicit in the UPS data, this issue will be addressed further in a theoretical discourse below.

The 1 to 1 mole ratio of O<sub>2</sub>/H<sub>2</sub>O mixture turned out to be the most facile at effecting oxidative changes in the valence band spectra. Figure 3 shows valence band difference spectra for surfaces that were exposed to 0.1 L of three different mole ratios of mixed O<sub>2</sub>/H<sub>2</sub>O, compared with data for 20 L of pure O<sub>2</sub>. Similar difference features can be seen for oxidation

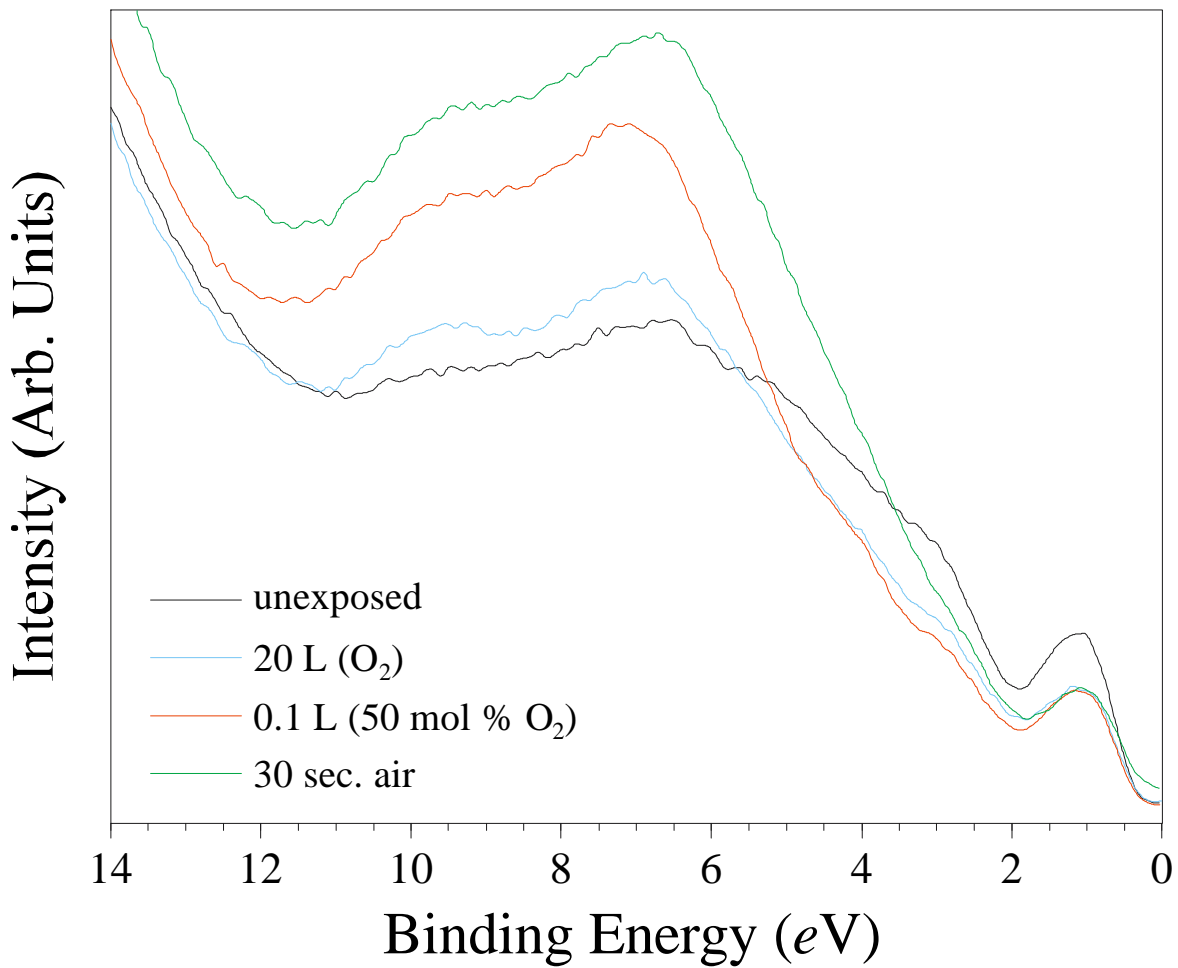


Figure 2: He I UPS valence band spectra comparing pristine pyrite surfaces with those exposed to O<sub>2</sub>, O<sub>2</sub>-H<sub>2</sub>O, and air.

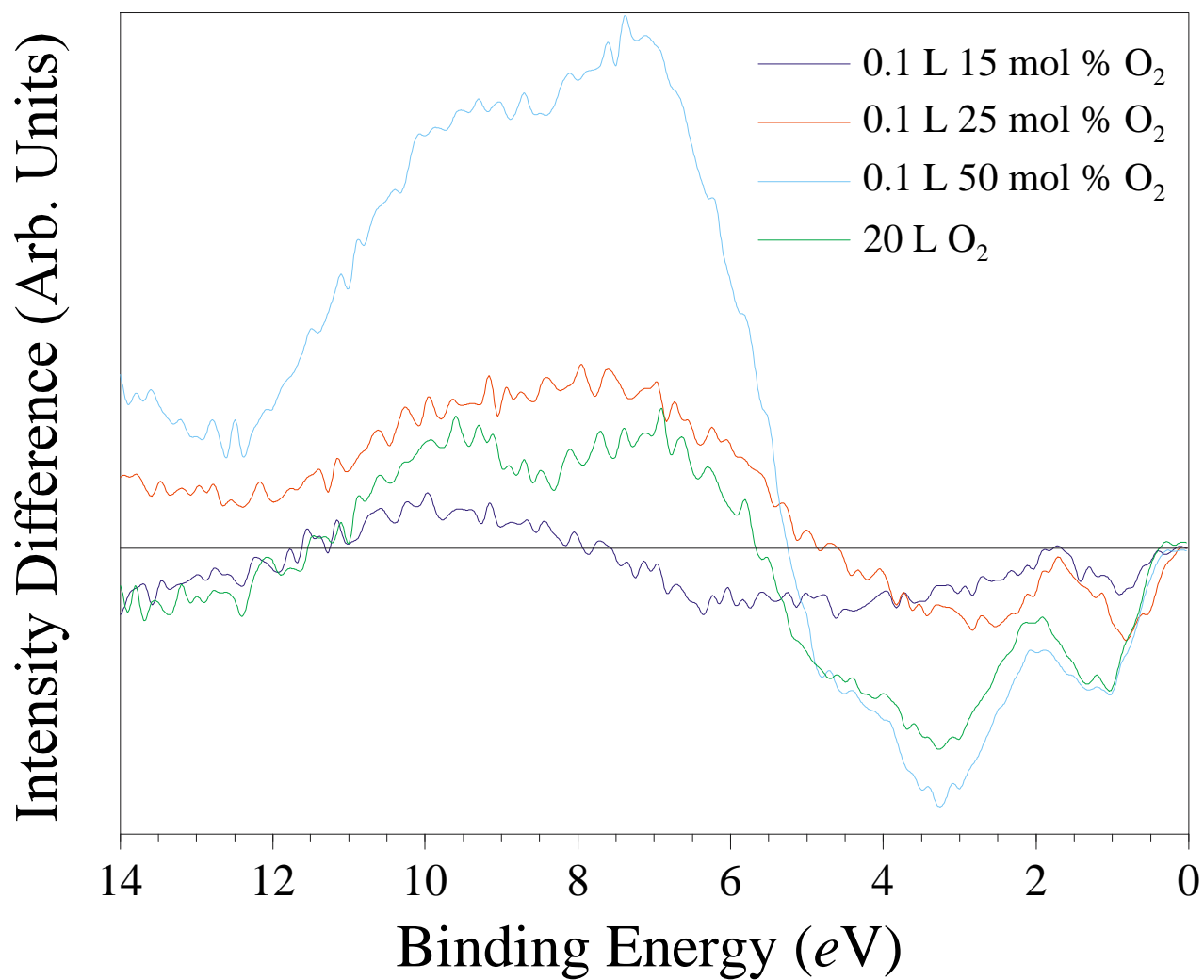


Figure 3: He I UPS valence band difference spectra of pyrite surfaces that were exposed to similar doses of different mixtures of O<sub>2</sub>-H<sub>2</sub>O, and a surface that was exposed to a much larger dose of pure O<sub>2</sub>.

by O<sub>2</sub> and by O<sub>2</sub>/H<sub>2</sub>O mixtures. As the concentration of O<sub>2</sub> in the mixture is reduced, the difference spectra approach that for pure H<sub>2</sub>O, *i.e.* no change. On the other hand, the pure O<sub>2</sub> end-member results in oxidation of a much lesser degree.

In Rosso and Hochella (submitted), it was shown that exposure of the pyrite surface to low energy electron beams and X-ray and UV incident radiation, especially UV radiation, alters the electronic structure of the surface towards a non-conductive state. Thus, it was of interest to examine the effect of this alteration on the surface reactivity. Samples were analyzed using UPS before exposure to various O<sub>2</sub> doses, and reanalyzed between each dose. It turned out that samples that were initially UV irradiated displayed no change in the upper valence band DOS when exposed up to 166 L O<sub>2</sub> (Fig. 4). The alteration of the surface to a non-conductive state is apparently accompanied by an inertness of the surface towards oxidation by O<sub>2</sub>. The possibility that this could be related to photo-enhanced oxidation of the surface by background gases in the analytical chamber can be ruled out based on the good agreement between our He I UPS spectra of the unexposed in-vacuum fractured surface and identical analyses performed elsewhere (Li *et al.*, 1974; Van der Heide, 1980; Pettenkofer *et al.*, 1991). The idea that the UV altered surface would be less reactive was tested by irradiating the upper half of an in-vacuum cleaved sample to He I UV radiation, removing it from the instrument along with the non-UV irradiated lower half, and let the entire sample oxidize in air for 7 days. The UV exposure for the upper half was that for typical UPS data collection on the system (approx. 10 minutes) which has been shown to cause the surface to become non-conductive as determined by failed attempts to engage tunneling contact between the tip and the surface with UHV STM. XPS analyses of Fe 2*p*, S 2*p*, O 1*s*, and C 1*s* are shown in Figure 5 for both portions of the sample. The O 1*s* counts are higher for the UV irradiated sample and Fe 2*p* and S 2*p* counts are lower, suggesting more oxygen coverage at the surface and a higher susceptibility to oxidation in air for the irradiated sample. At this time, no tested explanation can be offered for this surprising result, and an in-depth investigation into this behavior is beyond the scope of this study.

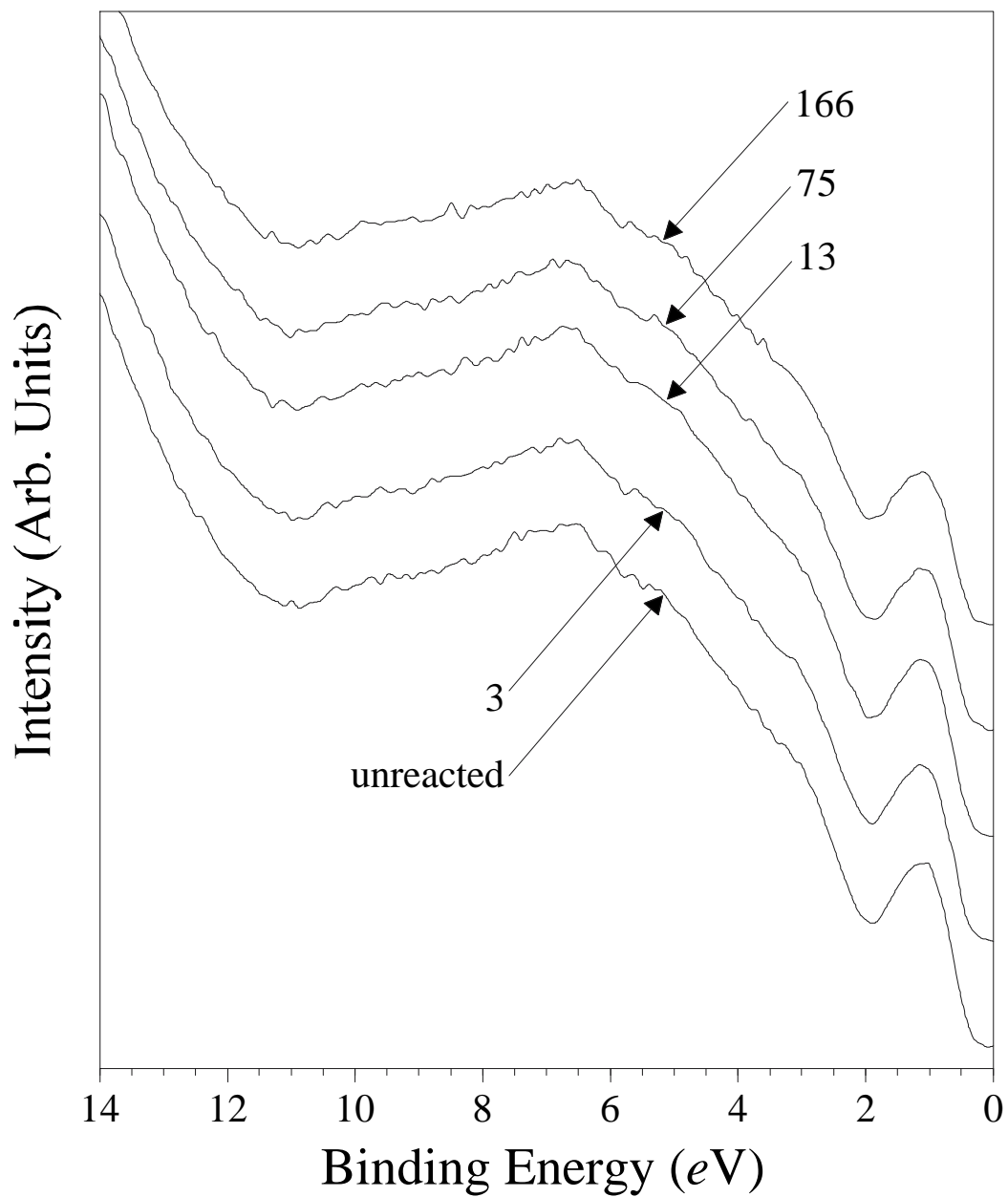


Figure 4: He I UPS spectra showing no change in the valence band structure of a pyrite surface exposed to various doses of O<sub>2</sub> (L) after the surface had been irradiated with He I UV light.

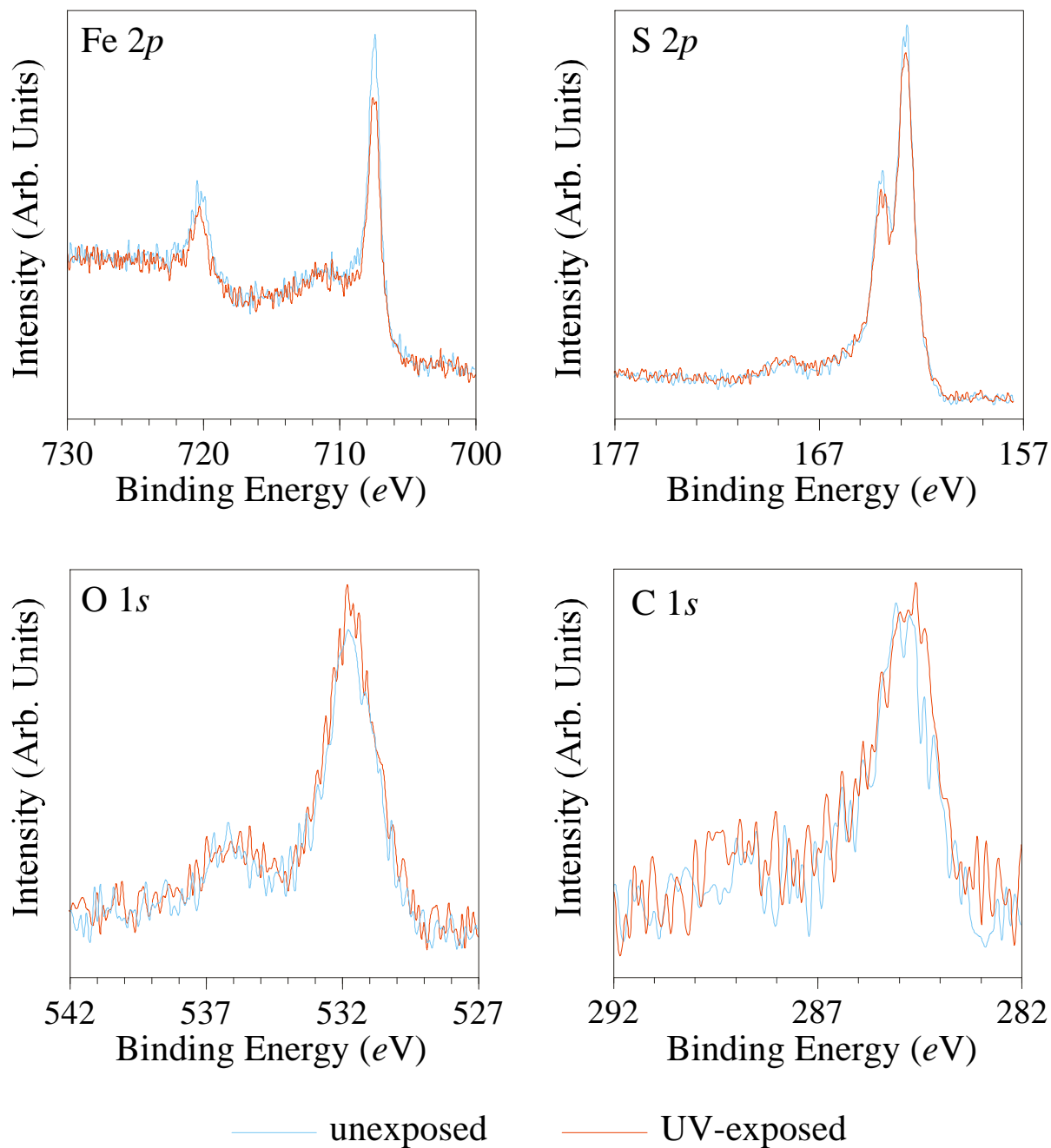


Figure 5: XPS spectra of UV-exposed and unexposed pyrite allowed to oxidize in air for 7 days.

However, the change in the surface electronic structure may be related to photo-enhanced generation of electron-hole pairs and charge trapping/de-trapping, which can alter the energy and occupation of surface states (see Jaegermann and Tributsch, 1988; Osseo-Asare, 1993).

### Scanning Tunneling Microscopy

STM is a very sensitive and local probe of the electronic density of valence and conduction bands states near the Fermi level. Atomically resolved UHV STM images of pyrite at low negative or positive bias display a face-centered cubic array of high tunneling current sites (bright sites) at Fe centers (Rosso and Hochella, submitted). The S<sub>2</sub> dimer is located at the lower tunneling current sites (dark sites). The higher relative tunneling current at Fe sites at negative or positive bias voltage arises primarily from the dangling bond surface state which dominates the top of the valence band and forms the bottom of the conduction band at the surface. The interaction of these states with oxygen should therefore involve the formation of Fe-O bonds which quench the surface state and decrease the tunneling current over reacted Fe sites at either bias.

Indeed, images collected on O<sub>2</sub> exposed samples show the development of distinct dark “patches” (Fig. 6) where surface Fe sites have been oxidized. Likewise, images collected simultaneously at both negative and positive bias (dual-mode STM) show the reduction of surface state density at both the valence and conduction band edges, localized on Fe (Fig. 7). Because imaging pyrite at the atomic scale is a relatively difficult task, “real-time” observations of oxidation progress were not feasible. However, successful observations of the atomic scale oxidation features, for both O<sub>2</sub> and O<sub>2</sub>/H<sub>2</sub>O dosed surfaces, showed a consistent set of characteristics. For the small range of tunneling conditions that led to the clearest atomic imaging, the tunneling current decrease from the average bright site to within a dark patch is the same within error as the difference between the bright Fe and the dark S<sub>2</sub> sites. The patches are more often than not bounded by surface {11} or Fe-Fe directions, in agreement with air

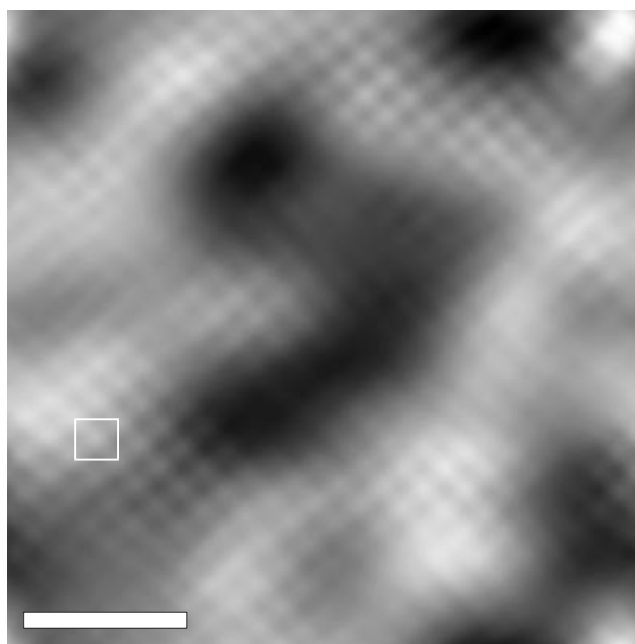


Figure 6: Atomic-scale topographic UHV STM image of an in-vacuum cleaved pyrite {100} surface after exposure to 4 L oxygen. The tunneling conditions were -0.1 V bias and 3 nA setpoint current. The image was band pass FFT filtered to remove noise. The scale bar represents 20 Å. A unit cell is outlined. The image shows oxidation features in the form of dark "patches" where Fe sites have reacted with oxygen.

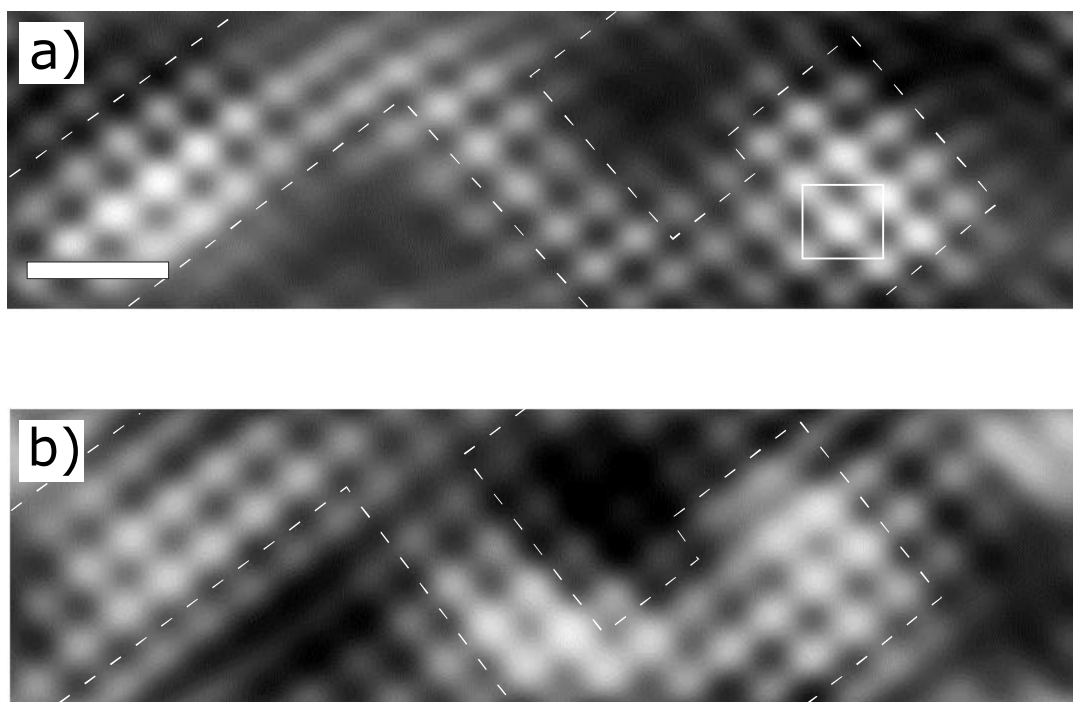


Figure 7: Dual-mode current UHV STM images collected simultaneously on pyrite {100} exposed to 4 L oxygen. The tunneling conditions were -20 mV bias and 3 nA setpoint current (a), and 20 mV bias and 3 nA setpoint current (b). The scale bar represents 10 Å. The images were band pass FFT filtered to remove noise. Dark patches due to oxidation occur in both images indicating that state density is removed from both the valence and conduction band edges. A local reduction in the tunneling current at sites neighboring a patch can be generally seen as circumscribed by white dashed lines. Oxidation patches are generally bounded by  $\langle 11 \rangle$  directions across the surface.

oxidation observations (Eggleston *et al.*, 1996). In the higher quality images of the oxidation patches, a decrease in tunneling current is observable at Fe sites bordering a patch (Figs. 7, 8, 9, and 10). This observation of atomic structure at the transition between oxidized and unoxidized domains is most readily apparent in the current images, rather than the topographic, or Z-piezo voltage images (*e.g.* Fig. 7). This may indicate that the oxidation of an Fe site may also draw state density from neighboring Fe sites, or there may be a decrease in the tunneling transmission probability due to an increase in the local workfunction at sites neighboring a patch. Workfunction increases are the general rule where sorbing species form a surface dipole with the negative end towards vacuum. This effect has been documented for the adsorption of Br<sub>2</sub> on in-vacuum cleaved pyrite (Pettenkofer *et al.*, 1991), although no significant workfunction change was observed in this study using UPS. Therefore, the observation that decreased tunneling current sites border an oxidation patch probably equates to a strong local influence of oxidized Fe on the density of states of surrounding sites. This is similar to the effects predicted in calculated STM images of a PbS surface with sorbed oxygen (Becker and Hochella, 1996).

In all the UHV STM images collected on O<sub>2</sub> exposed surfaces, unreacted areas on the surface were found, even for O<sub>2</sub> doses of up to 600 L, much greater than the point at which UPS indicated that the surface had "stopped" reacting (20 L). This means that between 0 - 20 L O<sub>2</sub>, changes in the valence band structure observed by UPS is a reflection of the relatively rapid development of discrete oxidation patches. At higher doses, the surface oxidizes much more slowly. This is consistent with the observation that the progression of oxidation of the surface in air progresses slowly over the period of days using STM and UPS (Eggleston *et al.*, 1996) and XPS (Nesbitt and Muir, 1994). We interpret this to mean that the initial formation of oxidation patches involves surface sites of somewhat higher affinity for oxygen, possibly surface defects.

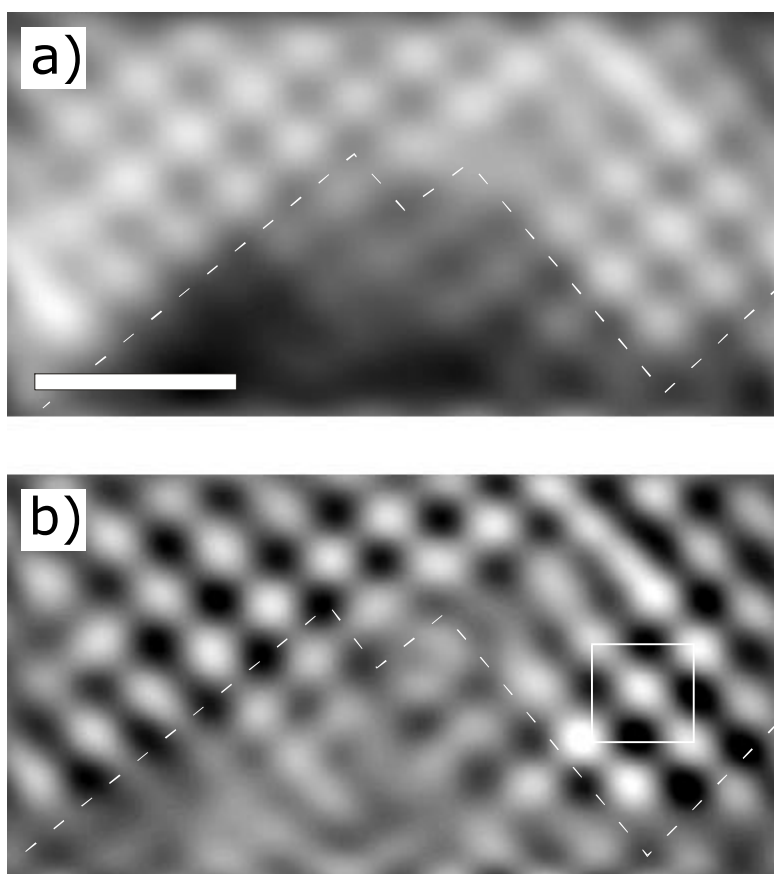


Figure 8: Topographic (a) and current (b) UHV STM images collected on pyrite {100} exposed to 4 L oxygen. The tunneling conditions were -0.1 V bias and 3 nA setpoint current. The scale bar represents 10 Å. The images were band pass FFT filtered to remove noise. White dotted lines outline an oxidation patch.

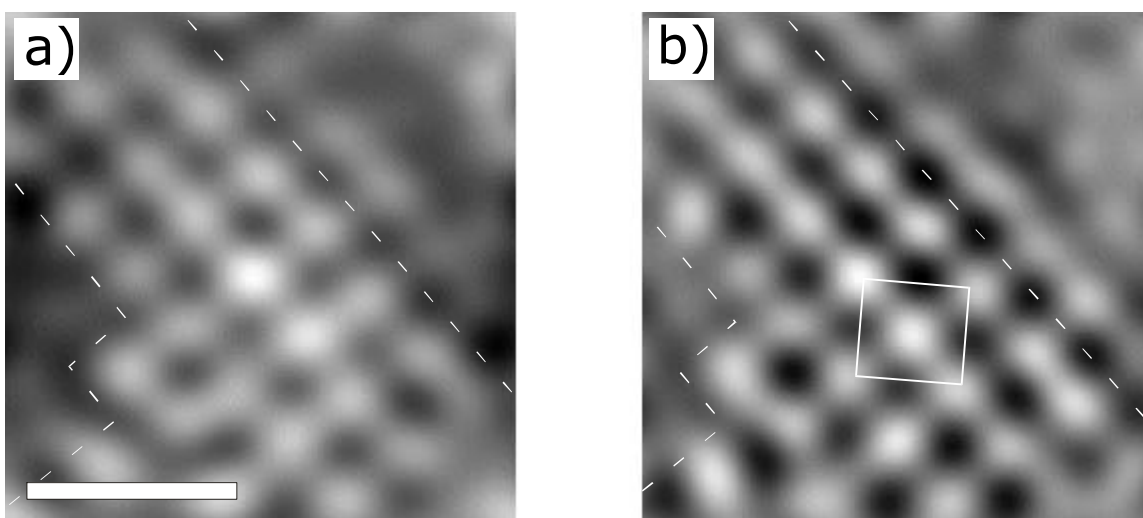


Figure 9: Topographic (a) and current (b) UHV STM images collected on pyrite {100} exposed to 4 L oxygen. The tunneling conditions were -0.1 V bias and 3 nA setpoint current. The scale bar represents 10 Å. The images were band pass FFT filtered to remove noise. White dotted lines outline oxidation patches.

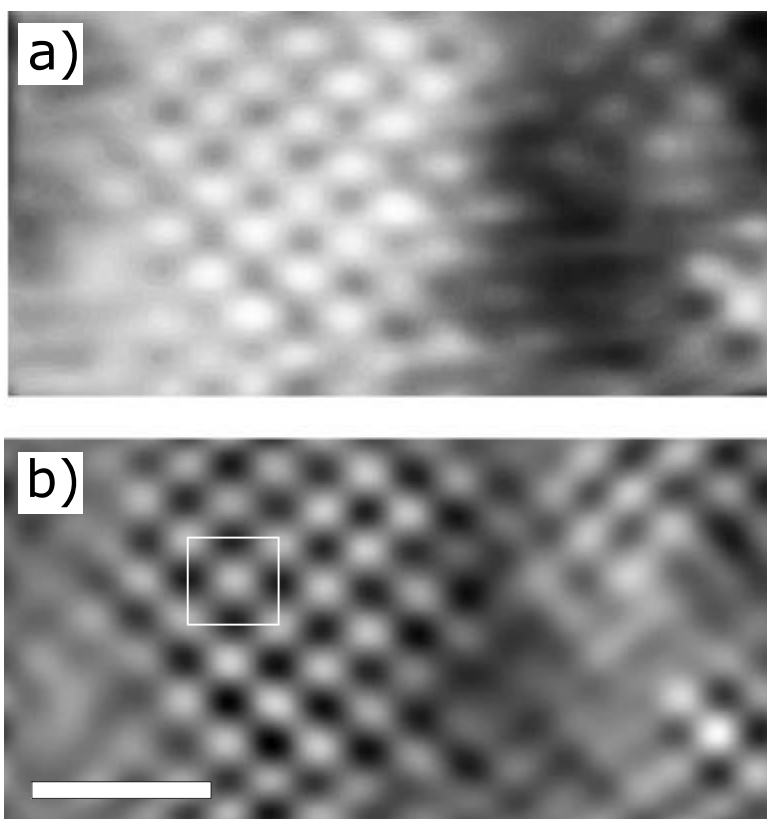


Figure 10: Topographic (a) and current (b) UHV STM images collected on pyrite {100} exposed to 0.4 L 40 mol % O<sub>2</sub> (O<sub>2</sub> - H<sub>2</sub>O). The tunneling conditions were -0.1 V bias and 2 nA setpoint current. The scale bar represents 10 Å. The images were band pass FFT filtered to remove noise. An oxidation patch is shown on the right of both images.

The occurrence and reactivity of defects has been a focal point in recent studies of pyrite surfaces. The presence of linear defects at the atomic scale at an estimated occurrence of 0.05 defects per surface Fe site have been demonstrated using STM in air (Eggleston *et al.*, 1996). Although we observed no linear defects, a small proportion of point defects were found which we interpret as Fe vacancies attributed primarily to cleavage induced surface damage (see Rosso *et al.*, in preparation). The Fe 2p XPS tail-off intensity (Karthe *et al.* 1993) and the specific adsorption behavior of H<sub>2</sub>O on UHV cleaned pyrite (Guevremont *et al.*, 1997; Guevremont *et al.*, 1998) has been attributed to S-deficient defect sites, which likewise have been projected to be present in the bulk crystal (Bronold *et al.*, 1994) at 1% concentration (Birkholz *et al.*, 1991). Since, in this study, no direct evidence for a significantly high concentration of surface defects was found, we can only tenuously ascribe the more reactive surface sites responsible for the birth of oxidation patches as similar to those described above.

From the UHV STM image data of surfaces exposed to low doses of O<sub>2</sub>, the initial reactivity of the surface can be addressed, cast in terms of the sticking probability for O<sub>2</sub>. The sticking probability is the fraction of the molecules that impinge on a surface and stick divided by the total number of impinging molecules. From the 4 L images (see Figs. 6, 7, 8, and 9), we estimate that, on average, 30% surface Fe sites have been oxidized. The exposure in Langmuirs (L) can be converted to molecules/cm<sup>2</sup> (*Ex*) by the relation (Masel, 1996):

$$Ex = \frac{2.97 \cdot 10^{16}}{\sqrt{MWT_g}} L$$

where MW is the molecular weight of the gas (AMU) and T<sub>g</sub> is the gas temperature (K). Using this equation, we calculate  $\sim 1 \times 10^{15}$  molecules/cm<sup>2</sup> impinge on the surface for a 4 L exposure of O<sub>2</sub>. Using Fe sites as the adsorption sites, then there are  $6.8 \times 10^{14}$  sites/cm<sup>2</sup> on a flat {100} terrace. Assuming for the moment that O<sub>2</sub> dissociatively sorbs (see *ab-initio* section below),

then a sticking probability of 0.1 is calculated for O<sub>2</sub> impinging on a pristine UHV-cleaved surface at room temperature.

### Scanning Tunneling Spectroscopy

I(V) tunneling spectroscopy involves measuring the dependence of the tunneling current on the bias voltage, which, when differentiated and normalized, can be nearly directly related to the sample density of states. Local and area-averaged I(V) tunneling spectra have been collected on these surfaces and have been successfully related to the surface DOS (Rosso and Hochella, submitted). Averaged I(V) tunneling spectra, showed a “flattening” in the shape of current response curve with O<sub>2</sub> exposure indicating an increasing insulating character to the surface (Fig. 11). Likewise, differential normalized tunneling spectra showed the progressive decrease in the DOS at the top of the valence band and the bottom of the conduction band (Fig. 12a), in agreement with the UPS observations. The loss of state density at the valence and conduction band edges is consistent with the consumption of the dangling bond states localized at Fe sites.

Difference tunneling spectra (exposed minus unexposed) (Fig. 12b) show that the DOS decreases are focused at  $\sim -1.5$  and  $+1$  eV, and increases occur at  $-3$  and  $2.5$  eV. In regards to the valence band changes, the trends between the UPS (Fig. 1b) and STS data (Fig. 12b) are similar in that the loss of state density is at a maximum in the vicinity of  $-1$  eV, which we attribute to electron transfer from surface states to oxygen. Likewise, this is followed by a more positive feature at between  $-2$  to  $-3$  eV ( $-2$  eV from UPS data,  $-3$  eV from STS data) that is attributed to S  $3p$  states. There are some differences here, however, that should be addressed. The difference intensity of the S  $3p$  feature is negative overall in the UPS data but positive in the STS spectra. This discrepancy is most likely due to the relative surface sensitivities of UPS compared with STS. The kinetic energy of the He I UPS photoelectrons from these S  $3p$  states equates to an electron attenuation length of approximately  $25 \text{ \AA}$  (Seah and Dench, 1979). Therefore, the UPS

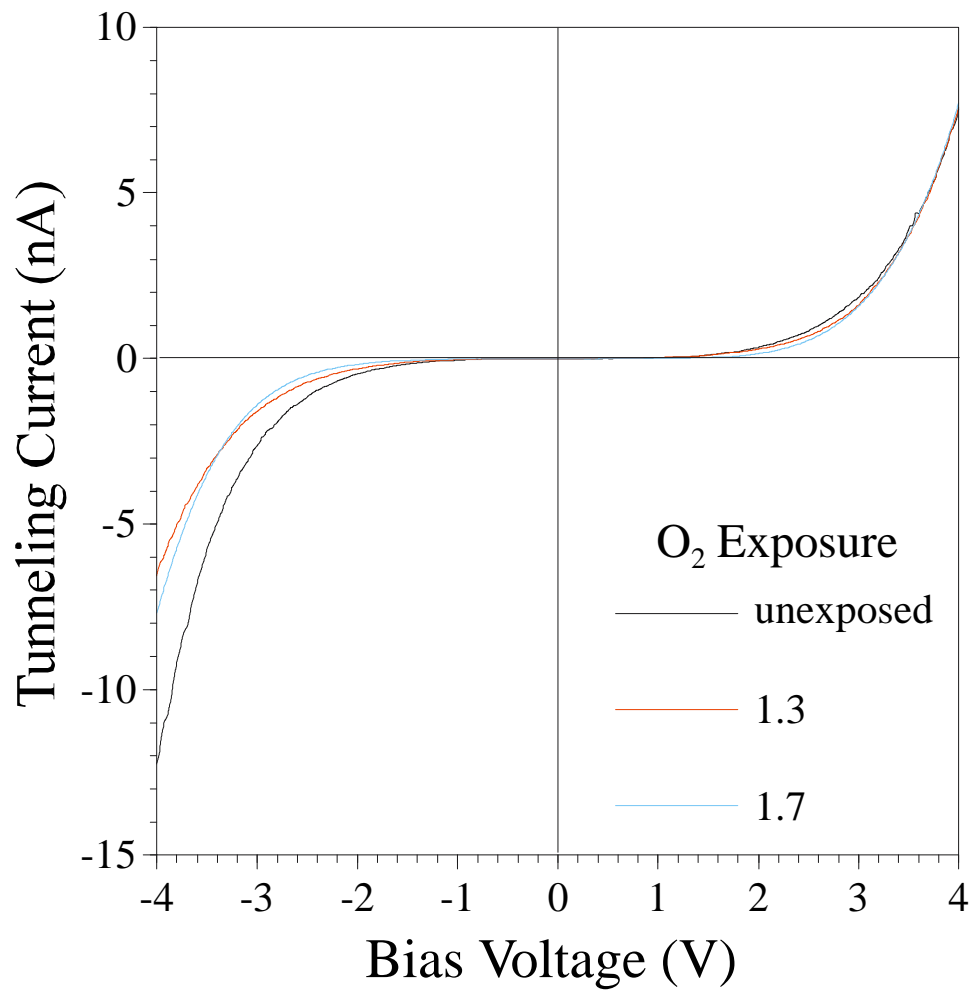


Figure 11:  $I(V)$  area-averaged tunneling spectra collected over a random distribution of points on pristine and  $O_2$  exposed surfaces. Each spectrum is the average of 125 spectra (see Methods section). The tunneling conditions were 4 V bias and 7 nA setpoint current.

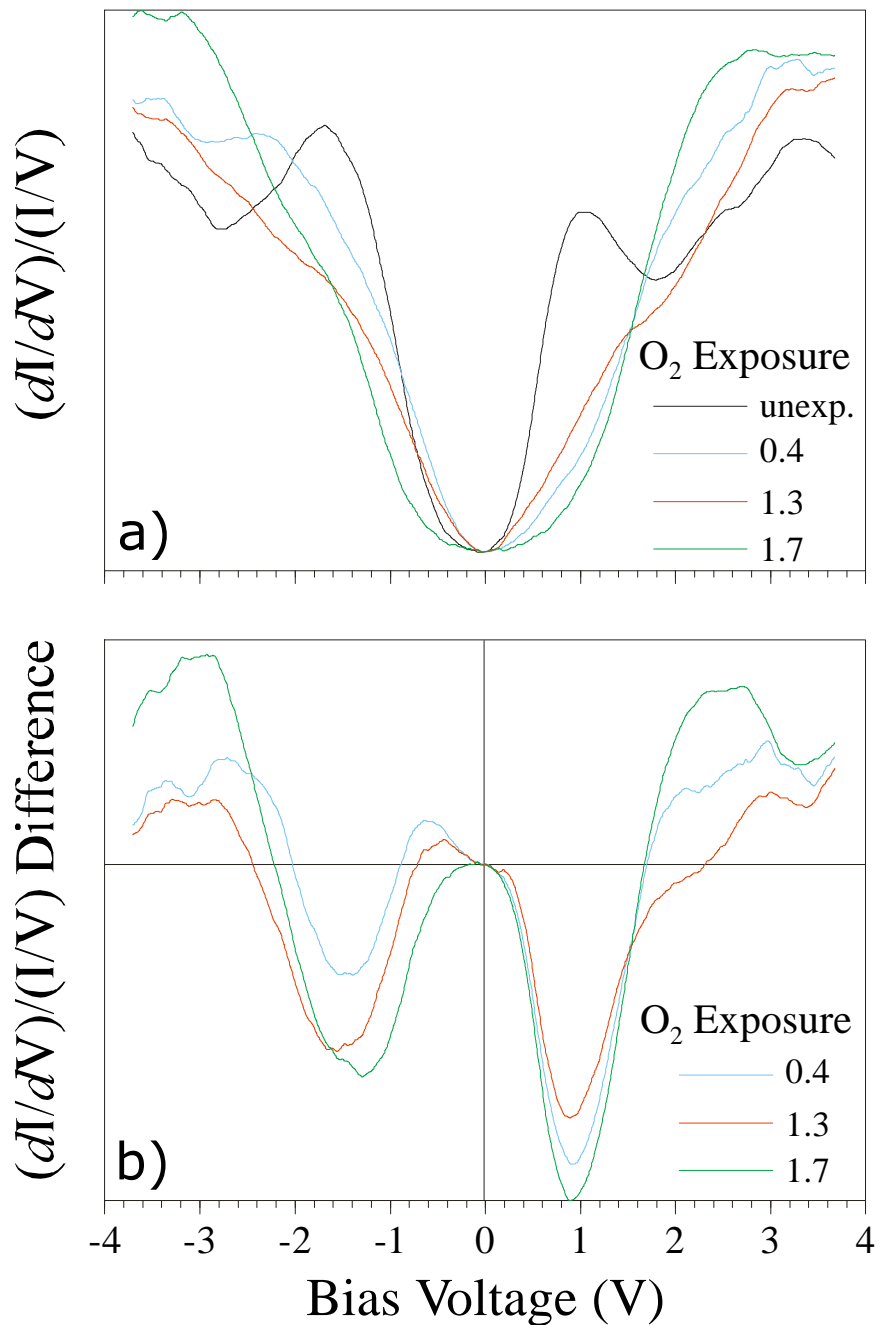


Figure 12: Area-averaged  $(dI/dV)/(I/V)$  tunneling spectra (a), and difference spectra (reacted - unreacted) (b) collected over a random distribution of points on pristine and  $O_2$  exposed surfaces (L). Each spectrum for oxygen exposed surfaces is the average of 125 spectra (see Methods section). The tunneling conditions were 4 V bias and 7 nA setpoint current.

data contain significant contributions from non-bonding Fe 3d states, which are progressively depopulated by sorbed O species causing a net loss in state density in the overlapping S 3p states. STS, on the other hand, is sensitive only to states that decay into the vacuum on the order of a few bond lengths ( $< 10 \text{ \AA}$ ) from the plane of the surface. Tunneling spectra of the in-vacuum cleaved surface show that contributions to state density in this range arise predominantly from dangling bond states and S 3p states (Rosso and Hochella, submitted). The non-bonding Fe 3d states contribute only minor state density because, in the language of molecular orbital theory, the non-bonding  $d_{xz}$ ,  $d_{yz}$ , and  $d_{xy}$  orbitals do not project normal to the plane of the surface. Thus, the S 3p feature in the difference STS spectra is less negative than that for the UPS data. An additional variable which may factor into the intensity discrepancy is related to the  $(dI/dV)/(I/V)$  conversion, which becomes less accurate when the tunneling conductance begins to diverge from a perfect exponential relationship (Hamers, 1993). The  $I(V)$  curves show a slight deviation from true exponential behavior, which could not be avoided (Fig. 11).

The discrepancies of the electron binding energy peak positions between the difference UPS and STS data can be related to a couple of factors. The first is due to difficulties in accurately unveiling the locations of the band edges in the conversion from  $I(V)$  to  $(dI/dV)/(I/V)$ . The conversion mathematically diverges near the Fermi level for semiconductors because  $I$  approaches zero faster than  $V$ , causing a spike in the gap region. A simple but effective strategy for suppressing the spike is to add a small constant to the  $(I/V)$  denominator across the spectrum. This invariably has the effect of shifting the apparent energies of the band edges away from the Fermi level slightly.

Another factor is related to the effects of the varying electric field between the tip and the sample during the voltage ramp, usually referred to as tip-induced band bending. It has been shown that the high field between the tip and sample can significantly alter the positions of the

bulk bands near the surface of wider band gap materials (Kaiser *et al.*, 1988; Weimer *et al.*, 1989). The effect spreads out the energies of the spectral features away from the Fermi level (Hamers, 1993). In general, a high concentration of occupied dangling bond states on the surface of a semiconductor tends to fully screen the effects of this field on the band positions by changing the occupation of the surface states somewhat (Kaiser *et al.*, 1988). Thus, in these experiments, the unexposed pyrite surface was most likely immune to the effects of tip induced band bending (Hamers, 1993). However, as sorbed O species consume the dangling bond states, the screening potential of the surface states is reduced and the effects of tip-induced band bending may then become significant. The end result is an artificial displacement of the energy of the tunneling spectral features, like the valence band S 3p feature, away from the Fermi level.

### **Ab-initio Calculations**

To this point, the effects of exposing pyrite surfaces to O<sub>2</sub>/H<sub>2</sub>O on the electronic structure of the surface have been presented. The adsorption behavior of mixtures of O<sub>2</sub> and H<sub>2</sub>O strongly suggest that there is an enhancement in the sticking probability for O<sub>2</sub>, or for H<sub>2</sub>O, or both. It becomes difficult to advance the interpretation of this behavior further, however, without submitting the observations to calculation. Because the interactions of these gases with the surface involves electron transfer, the problem must be approached with *ab-initio* calculations. Because pyrite is a transition metal sulfide, cluster calculations were necessary for investigating the reactivity of the surface due to the unwieldy computational costs that would be required to model adsorption reactions on this mineral with *ab-initio* periodic calculations. Cluster calculations have been successfully used to model adsorption on other systems (*e.g.* Hermann and Bagus, 1978; Siegbahn and Wahlgren, 1991; Becker and Hochella, 1996). For modeling surface sites, the cluster chosen contains one 5-coordinated Fe site and two 3-coordinated S sites on one surface (Fig. 13) which are the respective bonding environments for the uppermost surface Fe and S sites on a flat terrace. Corner Fe sites (coordinated by 3 S

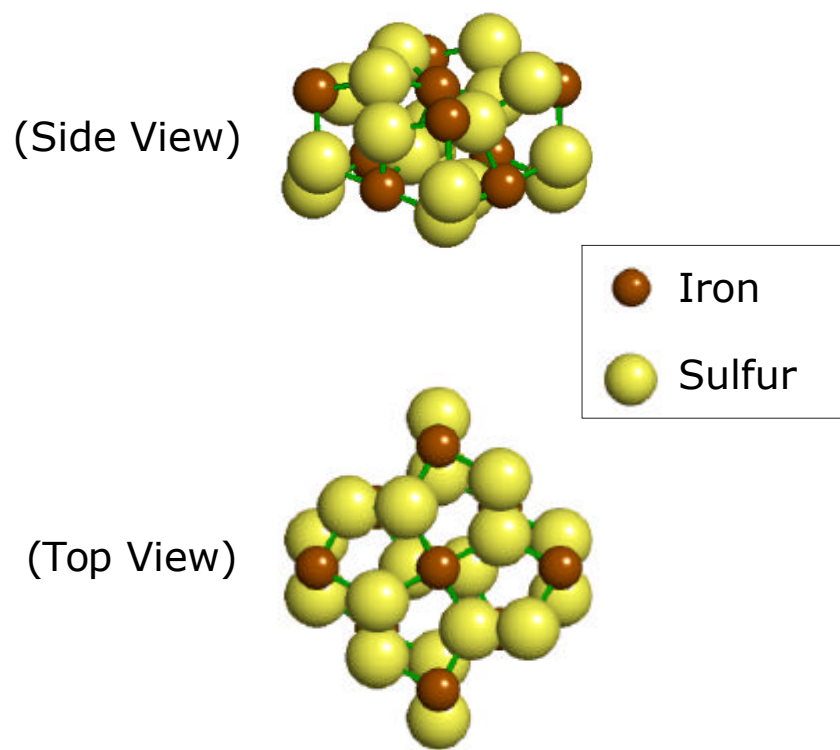


Figure 13: 27-atom cluster of pyrite used for *ab-initio* calculations of the interaction of the {100} surface with oxygen and water species.

atoms) were utilized as a basic model for surface “defect” sites consistent with the prevailing understanding that the {100} surface contains significant fractions of S-deficient defects (Birkholz *et al.*, 1991; Karthe *et al.* 1993; Guevremont *et al.*, 1997; Guevremont *et al.*, 1998). Since the structure of these defects is not yet known, the coordinatively undersaturated environment for a corner Fe site in the cluster can only be considered as a simplistic analogy.

**Oxygen.** Geometry optimizations of the position of an O<sub>2</sub> molecule over the surface show that the adsorption of an O<sub>2</sub> molecule (spin multiplicity = 3) to a surface Fe site is energetically downhill by 9.2 kcal/mol. O<sub>2</sub> takes up a tilted “end-on” geometry with the O closest to the Fe centered (Fe-O = 1.98 Å) along the Z-axis of the C<sub>4v</sub> symmetry bonding environment, restoring the distorted octahedral environment of bulk Fe (Fig. 14a). Mulliken population analyses show that the O bonded to the Fe has a net charge of -0.49 and essentially no  $\alpha$ - $\beta$  spin density, while the upper O is -0.13 and has a net spin density of 1. The charge drawn to the O bonded to the Fe leads to spin pairing of one of the unpaired spins in the  $\pi^*$  orbital of the O<sub>2</sub> molecule, but also effectively lowers the bond order from 2 to 1.5. This loss of bond strength is reflected in the longer O-O bond length for sorbed O<sub>2</sub> (1.38 Å) vs. that calculated for gaseous O<sub>2</sub> (1.21 Å). Likewise, the dissociation energy for sorbed O<sub>2</sub> is calculated to be 40% of that for free O<sub>2</sub>, which suggests that O<sub>2</sub> is more prone to dissociate on the surface.

The sorbed O<sub>2</sub> molecule (Fig. 14a) aligns itself between the largest separations of uppermost S sites, along Fe-Fe directions, owing to electrostatic repulsion between negatively charged O and S atoms. We tested the possibility that O<sub>2</sub> would dissociatively chemisorb by splitting the O<sub>2</sub> molecule into monatomic O atoms over Fe sites along the Fe-Fe direction. Geometry optimizations of these O atoms show that this configuration (Fig. 14a) is strongly thermodynamically favored over sorbed molecular O<sub>2</sub>, consistent with the predominant experimental observation of dissociative chemisorption for O<sub>2</sub> on a wide range of surfaces (see Zangwill, 1990; Benzinger, 1991; Henrich and Cox, 1994). The two O atoms compete for

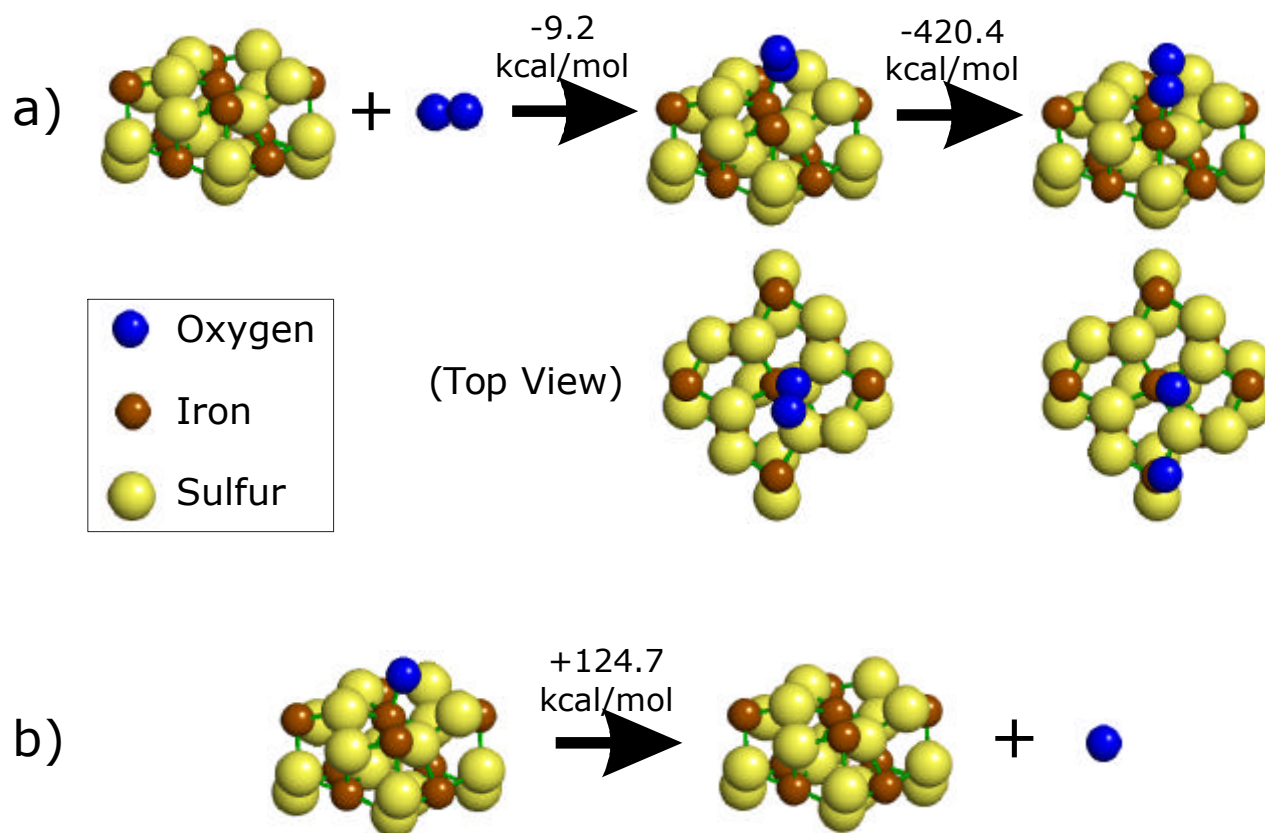


Figure 14: Optimized cluster configurations and reaction energies for the interaction of the pyrite {100} surface with  $O_2$  (a) and  $O$  (b). A negative reaction energy means that the respective arrow points in the downhill direction. The calculations indicate that oxygen dissociatively chemisorbs to Fe sites.

electrons from the cluster. The O atom bonded to the corner Fe, coordinated to 3 S atoms, is best characterized as chemisorbed  $O^-$  based on the 1.90 Å Fe-O bond length, -0.61 net charge, and one unpaired spin. The O atom on the center Fe, coordinated to 5 S atoms is best characterized as physisorbed O based on the longer bond length of 2.29 Å, near neutral charge of +0.12 owing mostly to polarization, and a spin density of 2. This is consistent with the premise that the oxidation of pyrite surface is more aggressive at S-deficient defect sites on the surface where Fe is coordinated to less than five S atoms.

To investigate the properties of sorbed  $O^-$  at a Fe site on a “defect-free” surface, we utilized clusters shown in Figure 14b. Monatomic oxygen sorbs in an “on-top” configuration over the center Fe site, with a Fe-O bond length of 1.96 Å and a bond energy of 124.7 kcal/mol. The sorbed  $O^-$  draws charge from the cluster, reducing it to a Mulliken charge value of -0.61, and has one unpaired spin. Taken altogether, the calculation results for the adsorption behavior of  $O_2$  are consistent with our experimental observations and those of Pettenkofer *et al.* (1991) for the sorption of the oxidant  $Br_2$  on pyrite {100}.

**Water.** Geometry optimizations of  $H_2O$  and related species are shown in Figure 15. The calculations indicate that the sorption of molecular  $H_2O$  at surface Fe sites is thermodynamically favorable, but with much less driving force than that for  $O_2$ . The  $H_2O$  molecule sorbs with the negative end of its dipole towards the surface, in agreement with the experimental observations of Pettenkofer *et al.* (1991) at lower temperature. The sorbed  $H_2O$  molecule is best characterized as physisorbed since the sum of the Mulliken charges for the  $H_2O$  molecule is 0.03, indicating no charge transfer. The adsorption energies for molecular  $H_2O$  over the center (Fig. 15a) and a corner (Fig. 15b) Fe site are estimated to be 50.8 and 57.8 kcal/mol respectively (exothermic processes), energetically downhill processes at room temperature given that  $kt \sim 0.5$  kcal/mol. In a recent study by Guevremont *et al.* (1998), the desorption energy difference for molecular  $H_2O$  from surface Fe sites and S-deficient defect

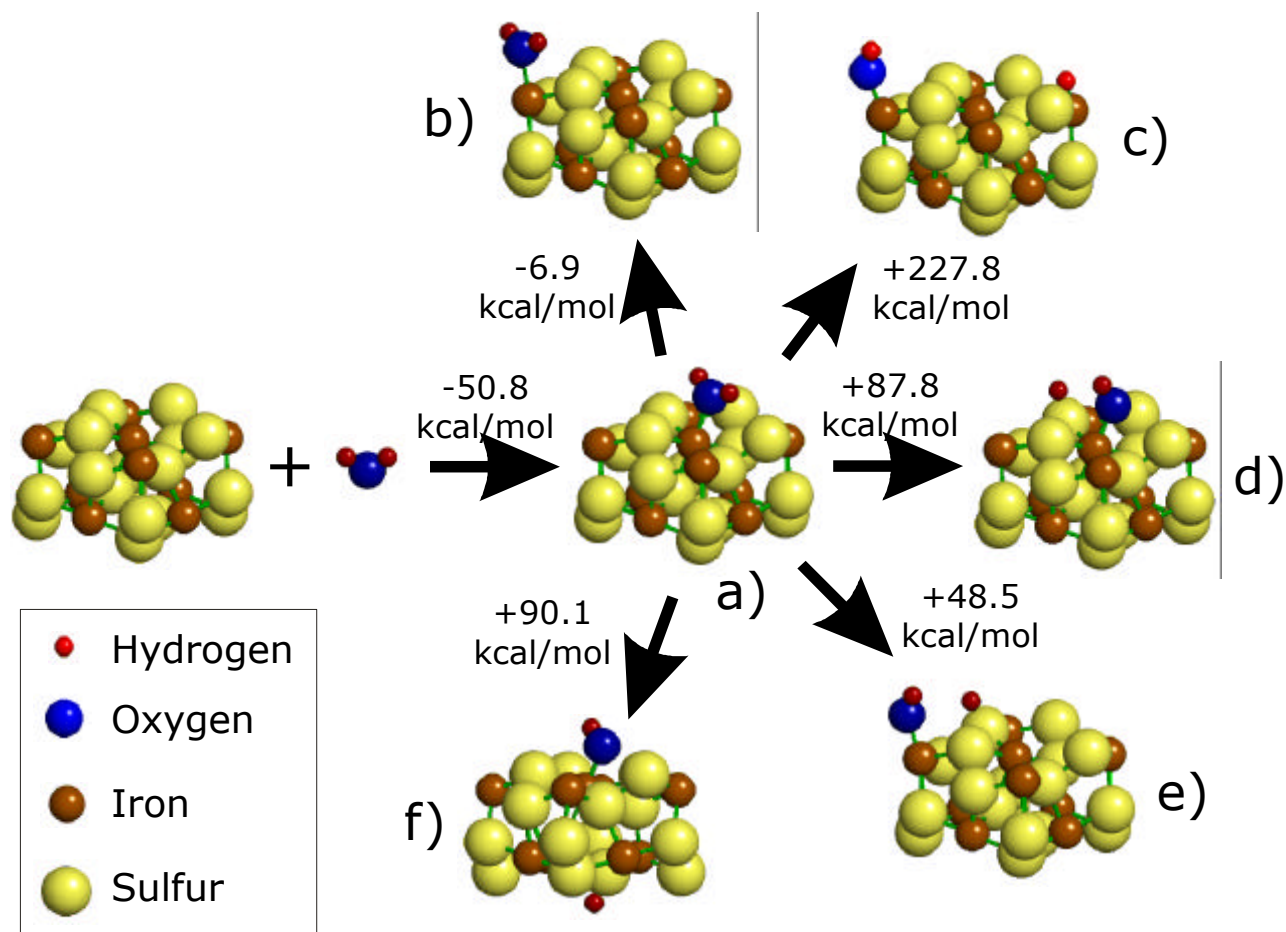


Figure 15: Optimized cluster configurations and reaction energies for the interaction of the pyrite {100} surface with water (a, b) and dissociated water (c, d, e, f) species. A negative reaction energy means that the respective arrow points in the downhill direction. The calculations indicate that water molecularly physisorbs to Fe sites.

sites was measured to be 5 kcal/mol using temperature programmed desorption. Thus, although the calculations incorrectly predict that H<sub>2</sub>O should molecularly sorb to the pyrite surface at room temperature, the direct comparison of cluster energies gives values consistent with experiment. Comparison of the energies of the molecularly sorbed H<sub>2</sub>O cases with various optimized configurations of dissociated H<sub>2</sub>O species (Fig. 15c-f) indicate that the dissociation of H<sub>2</sub>O on the surface is not thermodynamically favored, in agreement with experiment (Pettenkofer *et al.*, 1991; Guevremont *et al.*, 1998).

**Oxygen and Water.** Various configurations of H<sub>2</sub>O, H<sub>2</sub>O-derived species, and O<sup>-</sup> were geometry optimized on the upper surface of the cluster (Fig. 16), and the total cluster energies were compared. Because the dissociative chemisorption of O<sub>2</sub> is strongly downhill, monatomic O was optimized over the center Fe site along with OH<sup>-</sup> and H<sup>+</sup> at either corner Fe sites or surface S sites. The co-adsorption of molecular H<sub>2</sub>O and O<sup>-</sup> at Fe sites is calculated to be thermodynamically downhill by 42.5 kcal/mol (Fig. 16a). However, the adsorption energy is lower than for the individual H<sub>2</sub>O and O<sup>-</sup> adsorption cases, which may suggest that co-adsorption reactions for surfaces exposed to O<sub>2</sub>/H<sub>2</sub>O mixtures is an activated process. The most thermodynamically favorable configuration, however, turns out to be the case where O<sup>-</sup> and dissociated H<sub>2</sub>O species are sorbed to Fe sites (Fig. 16b). In the comparison of Figures 16a and 16b, the geometry optimized configuration in Figure 16b is favored by 23.6 kcal/mol. The O<sup>-</sup> is more strongly sorbed to the center Fe for the dissociated H<sub>2</sub>O case (1.96 Å, Fig. 16c) than for the molecular H<sub>2</sub>O case (2.02 Å, Fig. 16b). Likewise, the O-H bond lengths for the case shown in Figure 16b are 0.96 Å and 0.94 Å, which, when compared with the O-H distance in free H<sub>2</sub>O (0.95 Å), indicates a slight strengthening of one O-H bond and a slight weakening of the other. Collectively, these observations mean that although the dissociation of H<sub>2</sub>O on the H<sub>2</sub>O-exposed surface is energetically uphill (>48.5 kcal/mol), it is downhill on the O<sub>2</sub>/H<sub>2</sub>O exposed surface. This can be understood based on simple charge budget arguments. In the configuration in Figure 16b, electrons drawn into the sorbed O<sup>-</sup>, which has a -0.61 Mulliken

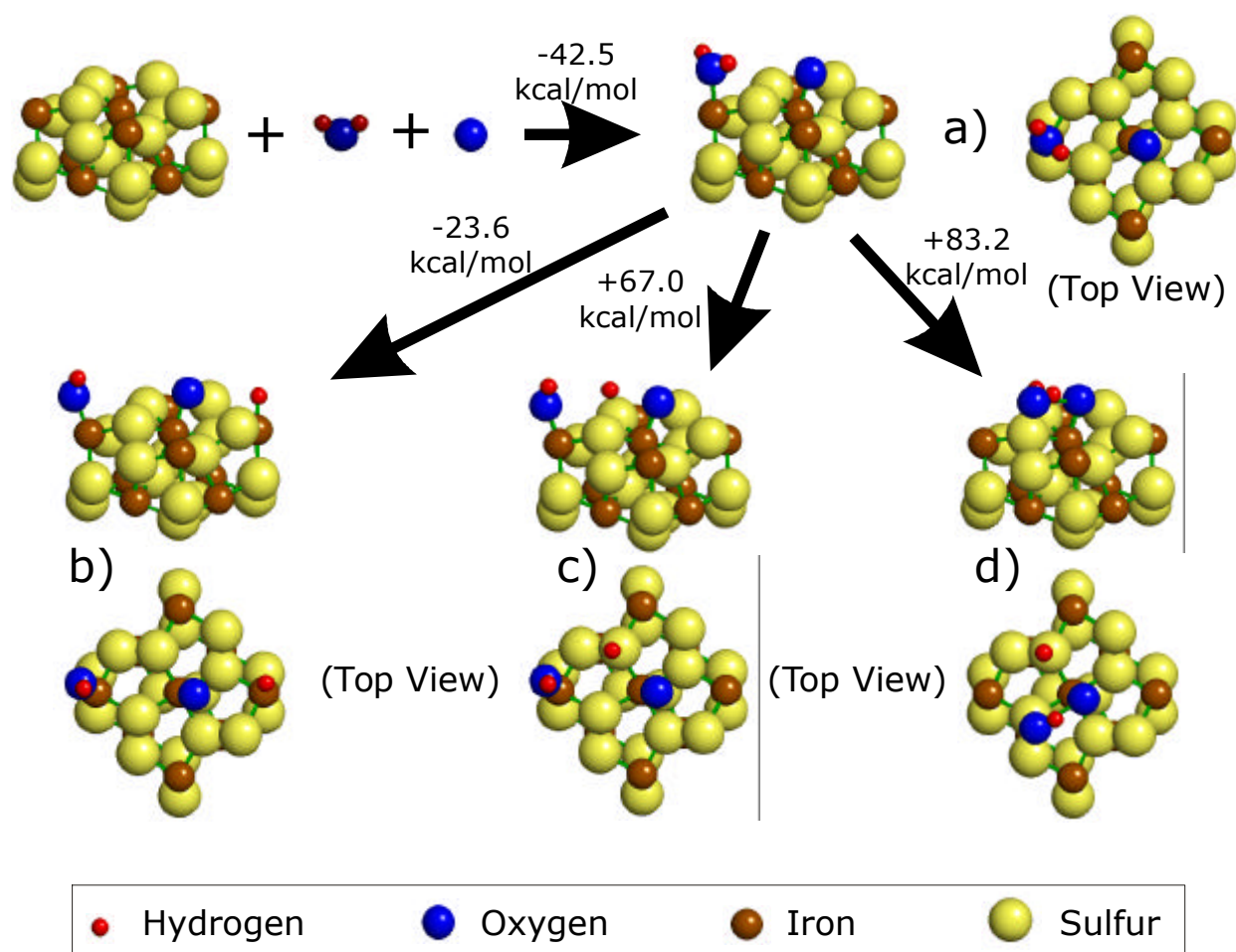


Figure 16: Optimized cluster configurations and reaction energies for the interaction of the pyrite {100} surface with oxygen and water species. A negative reaction energy means that the respective arrow points in the downhill direction. The calculations indicate that the co-adsorption of water and oxygen (O<sup>•</sup>) on surface Fe sites is energetically downhill (a). Sorbed water preferentially dissociates on the surface when co-adsorbed with oxygen (b).

charge, are replenished by dissociated H<sub>2</sub>O species, which effectively donate -0.43 charges back into the cluster. The approximate balancing of charge transfers to and from the surface with the combination of sorbed O<sub>2</sub> and H<sub>2</sub>O-derived species is the most energetically favorable method to quench Fe dangling bonds.

In the adsorbed O<sup>-</sup> calculations (Fig. 14), Mulliken population analyses of the upper surface atoms show that the electronic charge that is drawn from the cluster to populate the sorbed O<sup>-</sup> atom depletes the Fe and the two 3-coordinated S sites. The formation of Fe-O bonds at the expense of negative charge at S sites may increase the susceptibility of surface S sites to hydrophilic attack. Such a mechanism would be consistent with the experimental observations of Taylor and Wheeler (1984) and Reedy *et al.* (1991) that oxygen in the end-product sulfate is primarily derived from dissociated H<sub>2</sub>O. This question was tested by geometry optimizing the coordinates of an OH<sup>-</sup> over a surface S site, with and without the presence of sorbed O<sup>-</sup> at the center Fe site. In the case without any sorbed O present on the cluster, the OH<sup>-</sup> does not sorb to surface S. However, with O<sup>-</sup> sorbed, OH<sup>-</sup> sorbed to a surface S site is a stable configuration (Fig. 16d), partly stabilized by the charge depletion due to sorbed O<sup>-</sup> and partly due to hydrogen bonding to the sorbed O<sup>-</sup> (OH-O = 1.71 Å). But this configuration is thermodynamically unfavorable. The sorbed OH<sup>-</sup> is trapped in a local minimum, the global minimum for which is the case shown in Figure 16b. These calculations demonstrate that the proposed hydrolysis of surface S is chemically plausible in the presence of sorbed O<sup>-</sup>, but the question of whether or not this mechanism becomes dominant at more advanced stages of surface oxidation is difficult to address currently due to the required increase in computational costs.

## SUMMARY AND IMPLICATIONS

By comparison with the many previous studies of the oxidation of pyrite surfaces, this investigation elucidates surface reactions occurring at the earliest stages of oxidation, at the most chemically fundamental level. These results are largely consistent with the body of work on the oxidation of pyrite surfaces in both air and air saturated solutions. The high density of Fe 3d dangling bonds across the surface dictates the sorption behavior of both O<sub>2</sub> and H<sub>2</sub>O. Fe 3d<sub>z<sup>2</sup></sub> - O 2p<sub>z</sub> orbital bonding overlap increases the DOS at deeper levels in the valence band at the expense of surface state density from both the valence and conduction band edges. This process is likely to be more rapid at surface defect sites, in the case where the defects are S-deficiencies. The formation of Fe-O<sup>-</sup> and Fe-OH<sup>-</sup> bonds across the surface are precursors to the formation of iron oxides and oxyhydroxides, which have been experimentally observed using XPS to form on air oxidized pyrite before the formation of S oxidation products such as sulfate using XPS (Nesbitt and Muir, 1994).

Atomic-scale images of oxidation features show a local influence of oxidized Fe sites on the density of states of neighboring Fe sites. This effect is generally limited to nearest and next nearest neighbors adjacent to an oxidation patch. Its effect on the overall reactivity of the surface is difficult to quantify. Eggleston *et al.* (1996) modeled surface oxidation patches as discrete semiconducting phases with state density within the bulk band gap of pyrite. Our STM/STS data demonstrates that, at least for the initial stages of oxidation, surface state density decreases with oxidation progress. However, the adsorption and electron transfer reactions investigated here pertain only to the development of incipient product phases, whereas in the study by Eggleston *et al.* (1996), oxidation progress was possibly more advanced.

The theoretical prediction of preferential interaction of O<sub>2</sub> and H<sub>2</sub>O derived species with Fe 3d states, and not S 3p states, is in agreement with the appearance of a more positive S 3p

DOS feature just below the valence band edge, as indicated by UPS and STS difference spectra. Population analyses of  $O^-$  sorbed cluster calculations show that surface S sites are partially depopulated by the formation of Fe-O bonds and thereby the S sites become slightly more electropositive. This increases the susceptibility of surface S site to hydrophyllic attack and may eventually lead to the production of S-O bonds on the surface, as precursors to sulfate, consistent with the observation that oxygen, in the end product sulfate, is largely derived from  $H_2O$ .

This behavior would be consistent with an electrochemical oxidation mechanism where electron transfers to and from the surface take place at distinct anodic and cathodic sites. Perhaps the most salient outcome of this investigation is the evidence that such a mechanism can occur. Both the experiments and modeling calculations point to the importance of the roles of  $O_2$  and  $H_2O$  as combined reactants for the most effective adsorption to the surface, with Fe sites mediating as both anodic and cathodic sites. The cathodic reaction is the dissociative chemisorption of  $O_2$ , and the anodic reaction is the dissociation of molecularly sorbed  $H_2O$ . The coupled reactions provide a probable mechanism for the production of dissociated  $H_2O$  species at the pyrite surface, a necessary precursor to the development of sulfate.

### REFERENCES CITED

- Becker, U., and Hochella, M.F., Jr. (1996) The calculation of STM images, STS spectra, and XPS peak shifts for galena: New tools for understanding mineral surface chemistry. *Geochimica et Cosmochimica Acta*, 60, 2413-2426.
- Benzinger, J.B. (1991) Thermochemical methods for reaction energetics on metal surfaces. In *Metal-surface reaction energetics* (ed. E. Shustorovich), 53-107.

- Birkholz, M., Fiechter, S., Hartmann, A., and Tributsch, H. (1991) Sulfur deficiency in iron pyrite ( $\text{FeS}_{2-x}$ ) and its consequences for band-structure models. *Physical Review B*, 43, 11926-11936.
- Brundle, C.R. (1974) The application of electron spectroscopy to surface studies. *Journal of Vacuum Science and Technology*, 11, 212-224.
- Buckley, A.N., and Woods, R. (1987) The surface oxidation of pyrite. *Applied Surface Science*, 27, 437-452.
- Bullett, D.W. (1982) Electronic structure of 3d pyrite- and marcasite-type sulphides. *Journal of Physics C*, 15, 6163-6174.
- Bronold, M., Pettenkofer, C., and Jaegermann, W. (1994) Surface photovoltage measurements on pyrite (100) cleavage planes: Evidence for electronic bulk defects. *Journal of Applied Physics*, 76, 5800-5808.
- Eggleston, C.M. (1994) High resolution scanning probe microscopy: Tip-surface interaction, artifacts, and applications in mineralogy and geochemistry. In *Clay Minerals Society Workshop Lectures*, 7, 1-90.
- Eggleston, C.M., Ehrhardt, J.-J., and Stumm, W. (1996) Surface structural controls on pyrite oxidation kinetics: An XPS-UPS, STM, and modeling study. *American Mineralogist*, 81, 1036-1056.
- Feenstra, R.M. (1994) Tunneling spectroscopy of the (110) surface of direct-gap III-V semiconductors. *Physical Review B*, 50, 4561-4570.
- Frisch, M.J., Trucks, G.W., Schlegel, H.B., Gill, P.M.W., Johnson, B.G., Robb, M.A., Cheeseman, J.R., Keith, T.A., Petersson, G.A., Montgomery, J.A., Raghavachari, K., Al-Laham, M.A., Zakrzewski, V.G., Ortiz, J.V., Foresman, J.B., Cioslowski, J., Stefanov, B.B., Nanayakkara, A., Challacombe, M., Peng, C.Y., Ayala, P.Y., Chen, W., Wong, M.W., Andres, J.L., Replogle, E.S., Gomperts, R., Martin, R.L., Fox, D.J., Binkley, S., Defrees, D.J., Baker, J.,

- Stewart, J.J.P., Head-Gordon, M., Gonzalez, C., and Pople, J.A. (1995) Gaussian 94 (Revision C.2) Gaussian, Inc., Pittsburgh PA.
- Goldhaber M. B. (1983) Experimental study of metastable sulfur oxyanion formation during pyrite oxidation at pH 6-9 and 30°C. *American Journal of Science* 283, 193-217.
- Guevremont, J.M., and Strongin, D.R., and Schoonen, M.A.A. (1997) Effects of surface imperfections on the binding of CH<sub>3</sub>OH and H<sub>2</sub>O on FeS<sub>2</sub> (100): Using adsorbed Xe as a probe of mineral surface structure. *Surface Science*, 391, 109-124.
- Guevremont, J.M., and Strongin, D.R., and Schoonen, M.A.A. (1998) Photoemission of adsorbed Xenon, X-ray photoelectron spectroscopy, and temperature-programmed desorption studies of H<sub>2</sub>O on FeS<sub>2</sub> (100). *Langmuir*, 14, 1361-1366.
- Hamers, R.J. (1993) Methods of tunneling spectroscopy with the STM. In D.A. Bonnell, Ed., *Scanning tunneling microscopy and spectroscopy: Theory, techniques, and applications*, p. 51-103. VCH, New York.
- Henrich, V.E., and Cox, P.A. (1994) *The surface science of metal oxides*, 464 p. Cambridge, Cambridge.
- Hermann, K., and Bagus, P.S. (1978) Cluster studies of the interaction of oxygen with the lithium (100) surface. *Physical Review B*, 17, 4082-4099.
- Jaegermann, W., and Tributsch, H. (1988) Interfacial properties of semiconducting transition metal chalcogenides. *Progress in Surface Science*, 19, 1-167.
- Kaiser, W.J., Bell, L.D., Hecht, M.H., and Grunthaner, F.J. (1988) Scanning tunneling microscopy characterization of the geometric and electronic structure of hydrogen-terminated silicon surfaces. *Journal of Vacuum Science and Technology A*, 6, 519-523.
- Karthe, S., Szargan, R., and Suoninen, E. (1993) Oxidation of pyrite surfaces: A photoelectron spectroscopic study. *Applied Surface Science*, 72, 157-170.

- Kurtz, R.L., Stockbauer, R., Madey, T.E., Román, E., and de Segovia, J.L. (1989) Synchrotron radiation studies of H<sub>2</sub>O adsorption on TiO<sub>2</sub> (110). *Surface Science*, 218, 178-200.
- Li, E.K., Johnson, K.H., Eastman, D.E., and Freeouf, J.L. (1974) Localized and bandlike valence electron states in FeS<sub>2</sub> and NiS<sub>2</sub>. *Physical Review Letters*, 32, 470-472.
- Mårtensson, P., and Feenstra, R.M. (1989) Geometric and electronic structure of antimony on the GaAs (110) surface studied by scanning tunneling microscopy. *Physical Review B*, 7744-7753.
- Masel, R.I. (1996) *Principles of adsorption and reaction on solid surfaces*, 804 p., Wiley, New York.
- McKibben M. A. and Barnes H. L. (1986) Oxidation of pyrite in low temperature acidic solutions: Rate laws and surface textures. *Geochimica et Cosmochimica Acta* 50, 1509-1520.
- Moses C. O., Nordstrom D. K., Herman J. S., and Mills A. L. (1987) Aqueous pyrite oxidation by dissolved oxygen and by ferric iron. *Geochimica et Cosmochimica Acta* 51, 1561-1571.
- Moses C. O. and Herman J. S. (1991) Pyrite oxidation at circumneutral pH. *Geochimica et Cosmochimica Acta* 55, 471-482.
- Mycroft J. R., Bancroft G. M., McIntyre N. S., Lorimer J. W., and Hill I. R. (1990) Detection of sulphur and polysulphides on electrochemically oxidized pyrite surfaces by X-ray photoelectron spectroscopy and Raman spectroscopy. *Journal of Electroanalytical Chemistry* 292, 139-152.
- Nesbitt, H.W., and Muir, I.J. (1994) X-ray photoelectron spectroscopic study of a pristine pyrite surface reacted with water vapor and air. *Geochimica et Cosmochimica Acta*, 58, 4667-4679.
- Nicholson R. V., Gillham R. W., and Reardon E. J. (1988) Pyrite oxidation in carbonate-buffered solution: I. Experimental kinetics. *Geochimica et Cosmochimica Acta* 52, 1077-1085.

- Osseo-Asare, K. (1993) Pyrite in aqueous systems: Semiconductor properties, oxidative dissolution, and environmental control. In First International Conference on Processing Materials for Properties, The Minerals, Metals & Materials Society.
- Pettenkofer, C., Jaegermann, W., and Bronold, M. (1991) Site specific surface interaction of electron donors and acceptors on FeS<sub>2</sub> (100) cleavage planes. *Berichte der Bunsen-Gesellschaft für Physikalische Chemie*, 95, 560-565.
- Reedy B. J., Beattie J. K., and Lowson R. T. (1991) A vibrational spectroscopic <sup>18</sup>O tracer study of pyrite oxidation. *Geochimica et Cosmochimica Acta* 55, 1609-1614.
- Rosso, K.M., Becker, U., and Hochella, M.F., Jr. (in preparation) "Real-time" UHVSTM observation and molecular modeling of surface defect healing on pyrite.
- Rosso, K.M, and Hochella, M.F., Jr. (submitted) Atomically resolved electronic structure of pyrite {100} surfaces: An experimental and theoretical investigation with implications for reactivity.
- Seah, M.P., and Dench, W.A., (1979) Quantitative electron spectroscopy of surfaces: A standard data base for electron mean free paths in solids. *Surface and Interfacial Analysis*, 1, 2-11.
- Siegbahn, P.E.M., and Wahlgren, U. (1991) Cluster modeling of chemisorption energetics. In *Metal-surface reaction energetics* (ed. E. Shustorovich), 1-52.
- Stevens, W.J., Basch, H., Krauss, M. (1984) *Journal of Chemical Physics*, 81, 6026.
- Stevens, W.J., Krauss, M., Basch, H., Jasien, P.G. (1992) Relativistic compact effective potentials and efficient, shared-exponent basis-sets for the 3<sup>rd</sup>-row, 4<sup>th</sup>-row, and 5<sup>th</sup>-row atoms. *Canadian Journal of Chemistry*, 70, 612-630.
- Taylor B. E. and Wheeler M. C. (1984) Stable isotope geochemistry of acid mine drainage: Experimental oxidation of pyrite. *Geochimica et Cosmochimica Acta* 48, 2669-2678.

- Van der Heide, H., Hemmel, R., van Bruggen, C.F., and Haas, C. (1980) X-ray photoelectron spectra of 3d transition metal pyrites. *Journal of Solid State Chemistry*, 33, 17-25.
- Wagner, L.F., and Spicer, W.E. (1974) Photoemission study of the effect of bulk doping and oxygen exposure on silicon surface states. *Physical Review B*, 9, 1512-1515.
- Weimer, M., Kramar, J., and Baldeschwieler, J. (1989) Band bending and the apparent barrier height in scanning tunneling microscopy. *Physical Review B*, 39, 5572-5575.
- Wiersma C. L. and Rimstidt J. D. (1984) Rates of reaction of pyrite and marcasite with ferric iron at pH 2. *Geochimica et Cosmochimica Acta* 48(1), 85-92.
- Williamson M. A. and Rimstidt J. D. (1994) The kinetics and electrochemical rate-determining step of aqueous pyrite oxidation. *Geochimica et Cosmochimica Acta* 58, 5443-5454.
- Zangwill, A. (1988) *Physics at surfaces*, 454 p. Cambridge University Press, Cambridge.

## **Chapter Four**

### ***A UHVSTM/STS and Ab-Initio Investigation of Covellite {001} Surfaces***

#### **INTRODUCTION**

Covellite (CuS) has drawn the interest of many researchers due to its unique structural and electrical characteristics. It has a layered structure where copper is distributed into both tetrahedral and trigonal planar sites, and disulfide groups bind the layers. Its electrical properties are also extraordinary in that it is a very low resistivity ( $\sim 10^{-7} \Omega \cdot \text{m}$ , Meissner, 1929), moderate band gap semiconductor at room temperature ( $\sim 1 \text{ eV}$ , Shuey, 1975) and, after a subtle phase transformation at 55 K (Fjellvåg *et al.*, 1988), becomes a superconductor at 1.7 K (Meissner, 1929; Buckel and Hilsh, 1950). In these regards, covellite behaves curiously unlike many of its related counterparts so, the majority of all previous investigations have been directed at understanding its electronic structure (Narbutt, 1974; Nemnonov and Mikhailova, 1974; Sugiura *et al.*, 1974; Domashevskaya *et al.*, 1976; Nakai *et al.*, 1978; Tossell, 1978; Folmer and Jellinek, 1980; Vaughan and Tossell, 1980; Goble, 1985; Liang and Whangbo, 1993; Li *et al.*, 1994). Covellite is also one of the most common naturally occurring copper sulfides. It is primarily associated with supergene enrichment zones in precious metal deposits but is also found as a primary mineral in hydrothermal deposits (Shuey, 1975; Guilbert and Park, 1986).

The combination of the layered structure type and electrical properties make this material unique among the binary sulfides. This also means that this material is an ideal candidate for the direct interrogation of its electronic structure at the atomic scale using scanning tunneling microscopy and spectroscopy (STM/STS). The use of STM/STS to elucidate the atomic scale electronic structure of mineral surfaces is still a relatively new endeavor, but has been and continues to be successfully applied to surfaces of important natural oxides and sulfides.

Covellite has been successfully imaged at larger scales using an electrochemical STM (Higgins and Hamers, 1996), but imaging at the atomic scale has never been performed to our knowledge.

Much of the success in applying STM/STS lies with the ability to interpret the results at the quantum mechanical level, a difficult task without *a priori* knowledge of the electronic structure at the surface of the material. In this respect, STM/STS experiments are most fruitful when combined with theoretical calculations. The impetus for this study is both to affirm this statement and to examine the {001} surface of covellite using STM/STS, ultra-violet photoelectron spectroscopy (UPS), low-energy electron diffraction (LEED), and *ab-initio* calculations.

## METHODS

### Principal Instrumentation and Samples

STM, STS, UPS, and LEED were performed in a OMICRON compact ultra-high vacuum (UHV) lab operating at a base pressure of  $1 \times 10^{-10}$  mbar. Natural covellite single crystals from Alghero, Sassari, Sardinia, Italy and Summit Mtn., Colorado, USA were acquired from the Museum of Geological Sciences at Virginia Tech (#83 and #M1895, respectively). The samples exhibited reflection pleochroism (Frenzel, 1959) which is diagnostic for covellite (CuS), distinguishing it from Blaubleibender covellite (Cu<sub>1+x</sub>S). The resistivity of one of the samples was measured to be  $2.6 \times 10^{-7}$  Ω·m. Thin tabular samples with a surface area of approximately 8 × 8 mm were cut with a razor blade from larger specimens. The samples were cleaved along the basal plane in air or in an N<sub>2</sub>-purged glove bag before being introduced to UHV. For the in-air cleaved samples, the duration of exposure to air was approximately 1 minute. The samples were mechanically mounted on titanium stubs with titanium spot-welded spring clips.

### Ultra-violet Photoelectron Spectroscopy

UPS spectra were collected using He I (21.2 eV) radiation and a pass energy of 10 eV. The sample surface was oriented normal to the lens axis of the analyzer. The absolute binding energy scale of the UPS spectra was referenced to the sample Fermi level, which was determined by subtracting 21.2 eV from the low kinetic energy photoelectron cutoff energy and adding the workfunction of the spectrometer. The low kinetic energy edge was designated at the energy half way between the 16% and 84% count rate levels at the cutoff. The workfunction of the spectrometer is based on the measured position of the Ag  $3d_{5/2}$  photo peak.

### Low Energy Electron Diffraction

LEED patterns were acquired using 4-grid reverse view LEED optics (OMICRON) at beam energies between 50 - 125 eV. The electron gun has a spot size of approximately 1 mm. Patterns were photographically recorded and used for the determination of the surface unit cell size and symmetry.

### Scanning Tunneling Microscopy and Spectroscopy

For STM experiments, tips were prepared by electrochemically etching W wire in 1 M KOH. Samples and tips were stored under base pressure in a carousel attached to the main chamber. Samples were shielded from light during all STM imaging and tunneling spectra data collection. STM/STS data were collected at room temperature. Atomic scale images were processed using band pass FFT filtering to remove noise. Frequencies pertaining to atomic periodicity and low frequencies pertaining to “topographic” features were passed. The most successful tunneling conditions for atomic scale images were (bias, setpoint) +0.08 V, 3 nA; +0.20 V, 1 nA; -0.8 V, 1 nA; -0.6 V, 1 nA; and -0.20 V, 1 nA. I(V) tunneling spectra were collected simultaneously while imaging using a variation of current imaging and tunneling spectroscopy (CITS) (Hamers *et al.*, 1987) on a well developed {001} terrace. Spectra were

collected on a square  $10 \times 10$  grid of points within the  $400 \times 400$  grid of imaging points. At each spectroscopy point, the tip raster was paused, the feedback loop was turned off, the voltage ramp was applied, the loop was re-engaged, and imaging resumed. Each spectrum consisted of 200 spectral points. The total acquisition time for each spectrum was 42 ms including 50  $\mu$ s delays between each datum to let capacitive transients die out.  $I(V)$  Spectra that happened to be collected directly over bright and dark sites were grouped and averaged together. Tunneling spectra were collected over a voltage ramp of -0.8 to +1 during atomic imaging at -0.2 V and 1 nA setpoint current.

### ***Ab-initio* Calculations**

*Ab-initio* calculations of the electronic structure of covellite were performed using CRYSTAL95 (Dovesi *et al.*, 1996) and topological properties of the electron density distribution were calculated from the CRYSTAL95 wavefunction using TOPOND (Gatti, 1997). The calculations were performed on the 3 dimensional periodic crystal structure using the structure refinement of Evans and Konnert (1976). Full basis sets were used that have been developed specifically for use in periodic systems. An 86-411d41G basis set was used for Cu (Towler *et al.*, 1995) and an 86-311G basis set was used for S (Lichanot *et al.*, 1993). For the S basis set, the most diffuse *sp* function was removed to save unwarranted computational expense and to avoid problems with convergence. Wavefunctions were calculated at the restricted Hartree-Fock level of theory. 50 k-points were sampled (Monkhorst net) in the irreducible part of the Brillouin zone. The system converges to a metallic state.

## **RESULTS / DISCUSSION**

### **Surface Atomic Structure**

The structure of covellite has been well described in previous investigations, from the first examination by Oftedal (1932) to the improved refinements Evans and Konnert (1976). The

following summary ensues with reference to these previous studies. Each structural sheet-like unit of covellite consists of three layers of hexagonal close packed S atoms with Cu disposed in the tetrahedral and trigonal interstices. Cu is trigonally coordinated and S is trigonal bipyramidal within the middle layer (Figure 1a). Both Cu and S are tetrahedrally coordinated in the layers above and below the middle layer. The {001} surfaces of the top and bottom layers are defined by corner sharing faces of Cu tetrahedra. Two of these 3-layer units stack to form the repeat unit along the *c*-axis, joined by S-S bonds (Figure 1a).

Covellite cleaves readily along {001} resulting in large, atomically flat terraces, similar to other layered structure transition metal sulfides like molybdenite. The question then arises regarding the structure of the basal surface, which turns out to be a difficult question to answer completely. In contrast to molybdenite where groups of equivalent layers are bound by weak van der Waals S-S interactions, layers in covellite are bound by either covalent Cu-S or S-S bonds parallel to the *c*-axis. The S-S bond length is relatively short (2.07 Å), significantly shorter than the S-S bond length of the  $S_2^{2-}$  anion group in pyrite (2.14 Å), and is expected to be likewise strongly covalent. As is the case for pyrite, the S-S bonds are expected to be much stronger than the metal-sulfur bonds and therefore should be least likely to cleave. This point can be addressed more quantitatively using the theory of Atoms-in-Molecules (Bader, 1990), where the electron density at the bond critical point (bcp) can be considered a measure of bond strength. Using TOPOND/CRYSTAL95, the electron density at the bcps of the symmetry unique bonds in covellite were calculated (Table 1). The electron density at the bcp of the  $S_2$  unit is 86% higher than that for the Cu-S bond parallel to the *c*-axis. Considering that these bonds occur the same number of times per unit cell, the logical conclusion is that the latter bond will be preferentially broken during cleavage along {001}, as indicated in Figure 1a, in agreement with previous assertions (Evans and Konnert, 1976). This is also consistent with the fact that the 55 K phase transformation from hexagonal to orthorhombic involves a slight

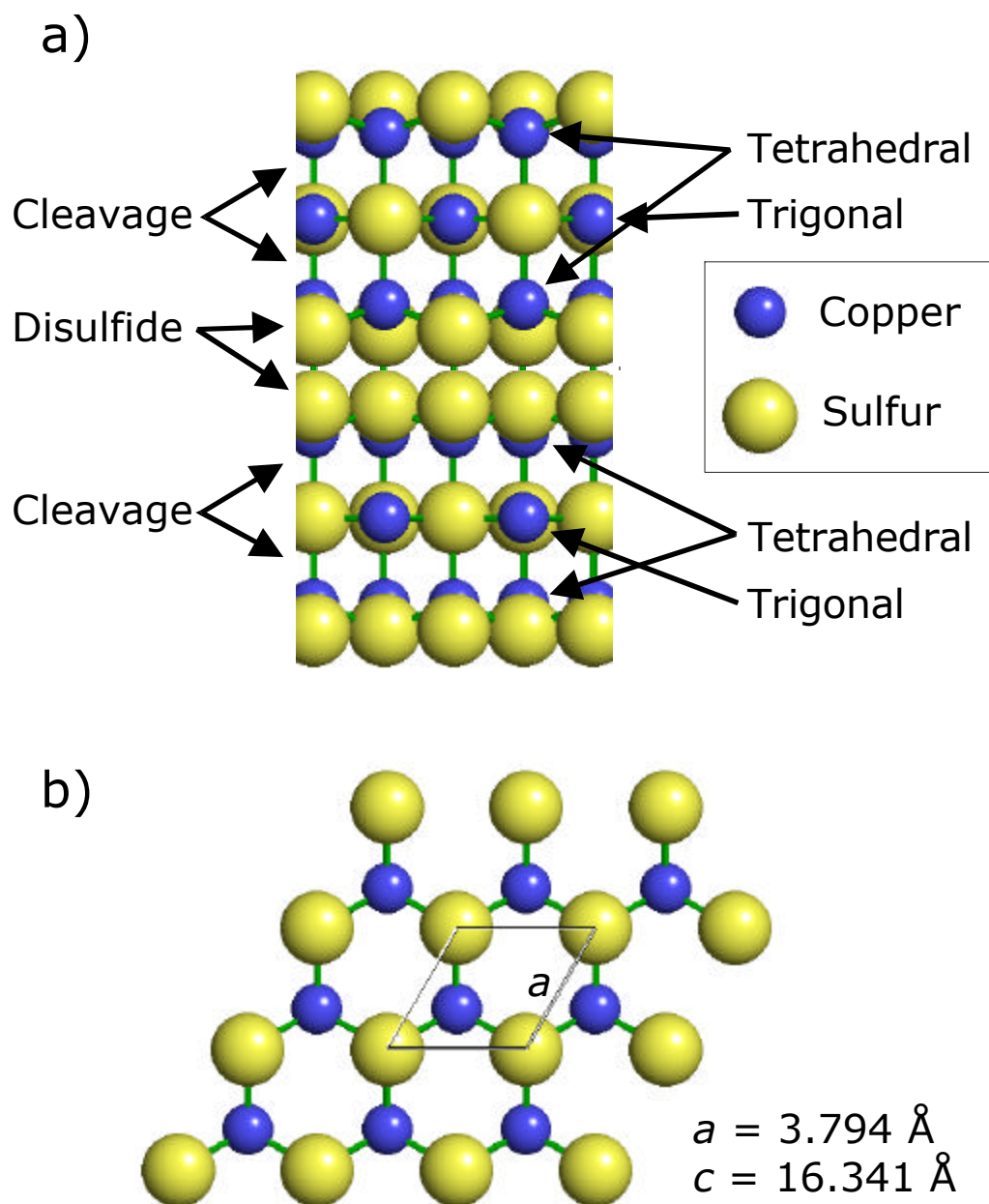


Figure 1: The structure of covellite viewed perpendicular to the  $c$ -axis (a), and parallel to the  $c$ -axis (b).

slipping of the trigonally coordinated Cu layers with respect to the tetrahedrally coordinated Cu layers (Fjellvåg *et al.*, 1988).

Table 1: Bond critical point properties for the symmetry unique bonds in covellite, where  $r(X)$  and  $r(Y)$  are bonded radii and  $\rho(r_c)$  is the electron density at the critical point.

Bond (X-Y)	$r(X)$ (Å)	$r(Y)$ (Å)	Bond Length (Å)	$\rho(r_c)$ ( $e/\text{Å}^3$ )
Cu-S ( $\perp$ $c$ -axis)	1.011	1.180	2.191	0.542
Cu-S ( $\parallel$ $c$ -axis)	1.044	1.288	2.332	0.421
Cu-S (other)	1.042	1.263	2.305	0.435
S-S	1.036	1.036	2.072	0.784

Hence, dividing the structure along the Cu-S bonds aligned parallel to the  $c$ -axis unfortunately creates two slightly different surface structures (Figure 1a). Before surface relaxation, in one case the plane of the surface is comprised of the trigonally coordinated Cu layer, with S atoms in the same plane and missing one bond, and in the other it is comprised of the formerly tetrahedrally coordinated Cu layer, with Cu atoms protruding above a S layer by 0.72 Å and missing one bond. Assuming for the moment that these surfaces do not reconstruct laterally, both surfaces would be similar when viewed down the  $c$ -axis in that they consist of an hexagonal array of Cu and S as shown in Figure 1b. This assumption is validated by the LEED patterns collected on surfaces of the in-air cleaved samples in this study. The LEED patterns display hexagonal symmetry with a measured surface cell size of 3.79 Å, which agrees well with the bulk  $a$  cell edge of 3.794 Å. However, structural relaxation perpendicular to the plane of the surface is probable (Hochella, 1990). For either surface, this would most likely involve withdrawing the S atoms into the surface somewhat, and “pushing” the Cu atoms away from the surface, similar to what has been calculated for PbS surfaces (Becker and Hochella, 1996). For the surface where the trigonal planar Cu layer is exposed, this would have the effect of breaking the planar symmetry by forming pyrimidal groups across the surface. Such a relaxation imparts even more similarity between the two possible covellite surfaces as they

would both be composed of corner sharing trigonal pyramidal groups with Cu atoms projecting further from the surface than S atoms.

In and of itself, the fact that two different yet similar covellite surfaces result from cleaving is an important result for any future surface investigation on this material. To address this more rigorously for covellite, however, requires either an unwieldy *ab-initio* periodic slab geometry optimization or quantitative LEED. For the present study, it is assumed that the surface structure can be generally represented by a hexagonal array of Cu and S atoms as shown in Figure 1b, with the Cu atoms protruding somewhat above the S atoms.

## Electronic Structure

Investigations of the electronic structure of covellite have been performed experimentally using K-edge and L-edge X-ray absorption near edge spectroscopy (Li *et al.*, 1994),  $K_{\beta}$  X-ray emission spectroscopy (Narbutt, 1974; Nemnonov and Mikhailova, 1974; Sugiura *et al.*, 1974), and X-ray photoelectron spectroscopy (Nakai *et al.*, 1978; Folmer and Jellinek, 1980). Theoretical investigations include *ab-initio* molecular orbital calculations (Tossell, 1978; Vaughan and Tossell, 1980) and extended Hückel tight binding calculations (EHTB) (Liang and Whangbo, 1993). A majority of these previous studies disagree on the distribution of oxidation states in the structure, especially with regards to Cu in the two different metal sites. However, the combination of studies by Liang and Whangbo (1993) and Nakai *et al.* (1978) forms a strong case that formal charges in CuS are best described by the formula  $(Cu^+)_3(S^{2-})(S_2^-)$ , where Cu in both tetrahedral and trigonal planar sites is approximately monovalent, the  $S^{2-}$  sites are the trigonal planar ligands, and the  $S_2^-$  sites are three of the four tetrahedral ligand sites. Our *ab-initio* periodic calculations are consistent with this distribution. Mulliken population analyses of the 3-dimensional wavefunction assign very similar oxidation states to Cu in both trigonal planar (+.978) and tetrahedral (+0.936) sites. Trigonal ligand S sites have a Mulliken charge of -1.428 and tetrahedral ligand S sites are given -0.711. It has been argued that the highest

occupied states in  $S_2^-$  orbitals should lie higher in energy and be only partially filled, as compared to the more completely filled  $S^{2-}$  orbitals (Liang and Whangbo, 1993). Hence, metallic conduction is mediated by the partially filled  $S_2^- 3p$  orbitals, with conductivity being most facile along the tetrahedrally coordinated Cu layers. This argument implies that the Fermi level should be flanked by predominantly S  $3p$  states, which has been theoretically confirmed using periodic EHTB calculations (Liang and Whangbo, 1993). In contrast, molecular orbital calculations on discrete clusters predict that the partially filled states should be crystal field like Cu  $3d$  states (Tossell, 1978; Vaughan and Tossell, 1980).

Total and projected valence band densities of states (DOS) were calculated using Crystal95 and compared them directly with UPS valence band spectra of a freshly cleaved sample of covellite (Figure 2). The calculated DOS projected onto S  $3p$  and Cu  $3d$  atomic orbitals shows that the highest occupied states are indeed predominantly comprised of S  $3p$  states, and lesser Cu  $3d$  states. The contribution of Cu  $3d$  becomes higher than that for S  $3p$  at slightly deeper levels in the valence band. Cu  $4s$  states are not shown in Figure 2 because they do not contribute significantly. Furthermore, the calculated total DOS is in very good agreement with the UPS spectra (Figure 2). According to these calculations, the consistency between our results and those of Liang and Whangbo (1993) supports the assertion that the highest occupied and unoccupied states are primarily S  $3p$  states.

For the purposes of this study, the next task is to address the difference between the electronic structure of the bulk mineral and at the {001} surface. This task is partly hampered by the fact that the surface atomic structure is only constrained and not exactly known, and partly because *ab-initio* periodic slab calculations of a metallic mineral are overly computationally intensive. However, it is reasonable to say that the electronic structure of the surface will not be significantly different, from the perspective of STM, from that described for the bulk unless dangling bonds shift state density into the bulk band gap. As a general rule,

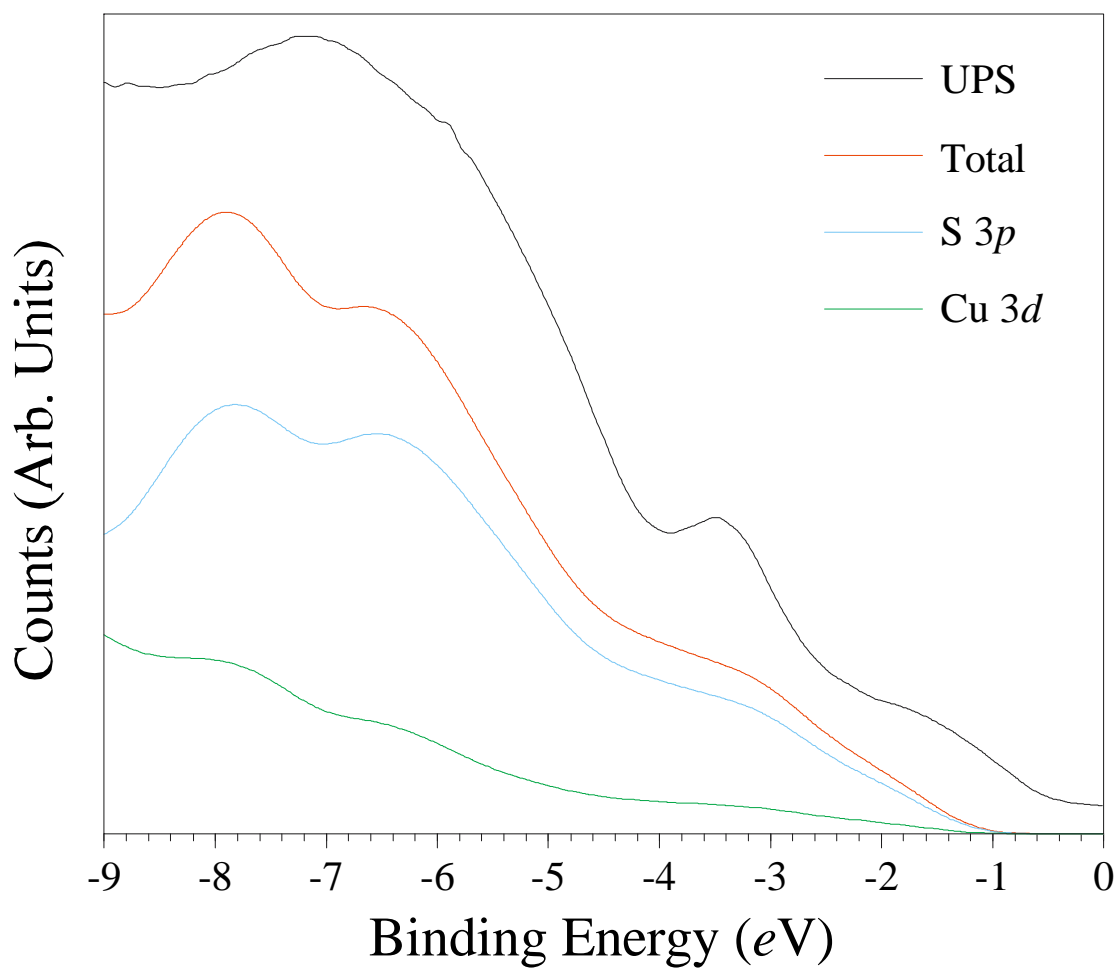


Figure 2: A comparison of experimental valence band spectra (He I UPS) with calculated densities of states. "Total" refers to the calculated total density of states, "S 3p" and "Cu 3d" refer to the calculated partial contributions from those respective states.

unreconstructed semiconductor surfaces will have dangling bond surface states (e.g. Zangwill, 1990). It has been shown for in-vacuum cleaved pyrite that *d* orbital dangling bonds are localized on surface Fe, but that undercoordinated surface S do not contribute surface state density (Rosso and Hochella, submitted). Assuming the same trend to be true for covellite, then the {001} surface terminated by broken Cu tetrahedra will have dangling Cu *d* states, but the surface terminated by the trigonal planar Cu layer will not. We can advance this discussion further with independent information supplied by STM/STS.

### Scanning Tunneling Microscopy

UHV STM images of natural covellite cleaved in air were initially collected at larger scales to characterize the surface microtopography. Large, flat terraces were found at imaging scales of hundreds of nanometers (Fig. 3a). Step heights as low as  $\sim 3 \text{ \AA}$  were found which is approximately equal to the height difference expected where both possible surface structures have been exposed and are juxtaposed next to each other on either side of the step. In some areas, the surfaces were unexpectedly rough and appeared to be “coated” with a secondary phase (Fig. 3b). This texture was also present on covellite cleaved in  $\text{N}_2$ . Hence, we interpret it to be a result of cleavage along a pre-exposed surface, a similar observation to that described for natural hematite cleavage planes (Junta-Rosso and Hochella, 1996). A detailed investigation of the chemistry of this secondary phase is beyond the scope of this study. Pre-exposed areas on the surface were avoided for the purposes of atomic scale imaging.

Atomically resolved UHV STM images were obtained on both air and  $\text{N}_2$  cleaved samples. At both positive (Fig. 4) and negative (Fig. 5) bias voltages, atomic images showed a hexagonal array of bright and dark sites with a repeat constant on the order of  $4 \text{ \AA}$  (variability due to drift), the latter being consistent with the LEED results.

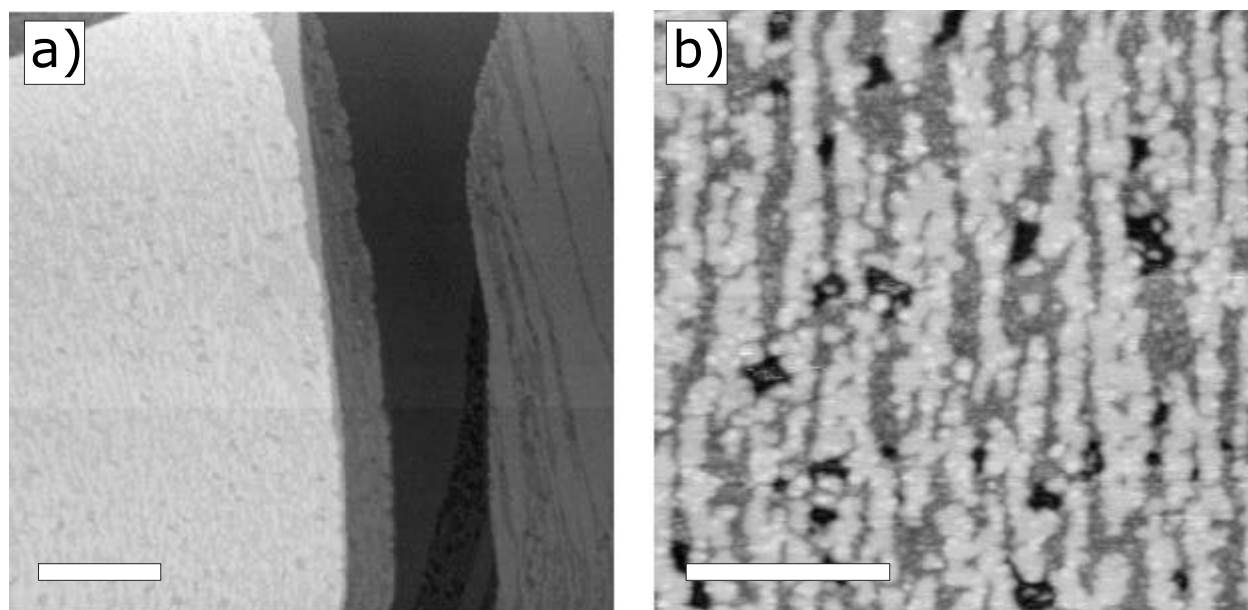


Figure 3: UHV STM images of the basal plane of covellite cleaved in air. The scale bars in a) and b) represent 100 nm and 40 nm respectively. As shown in a), large flat terraces are prevalent, separated by steps with heights as low as 3 Å. The surfaces of in-air or in-nitrogen cleaved covellite are often found to "coated" by a probable secondary phase as shown in b).

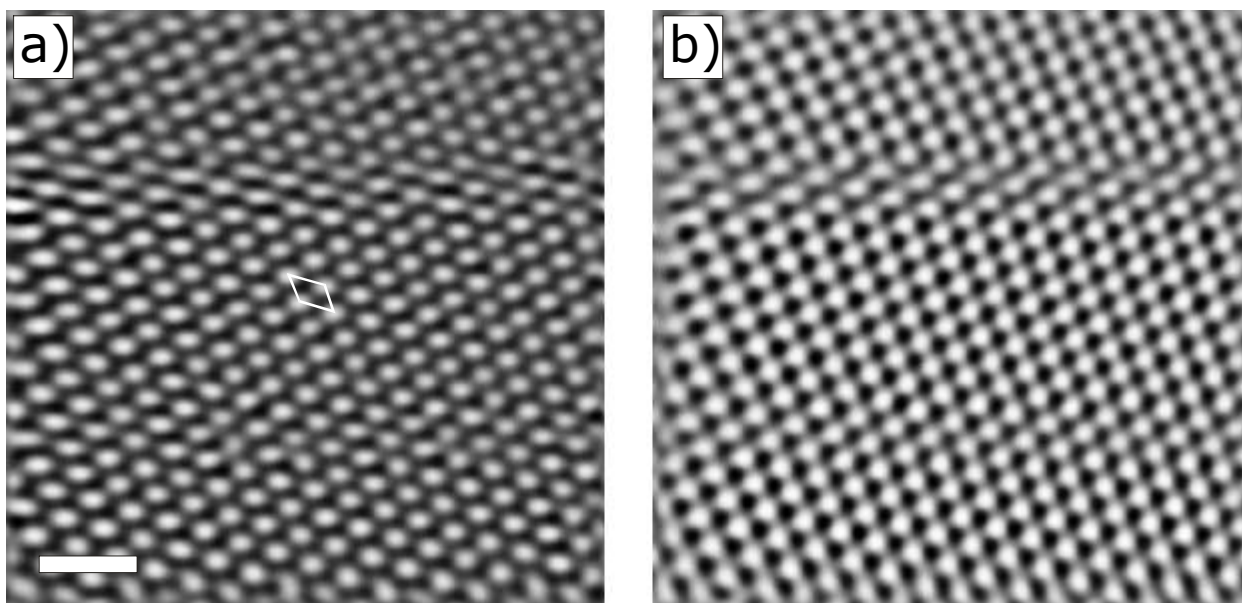


Figure 4: Topographic (a) and current (b) UHV STM images of the atomically resolved basal plane of in-nitrogen cleaved covellite. The scale bar represents  $10 \text{ \AA}$  for both images. The images were collected using  $+0.2 \text{ V}$  bias and  $1 \text{ nA}$  setpoint current. A hexagonal surface cell is indicated.

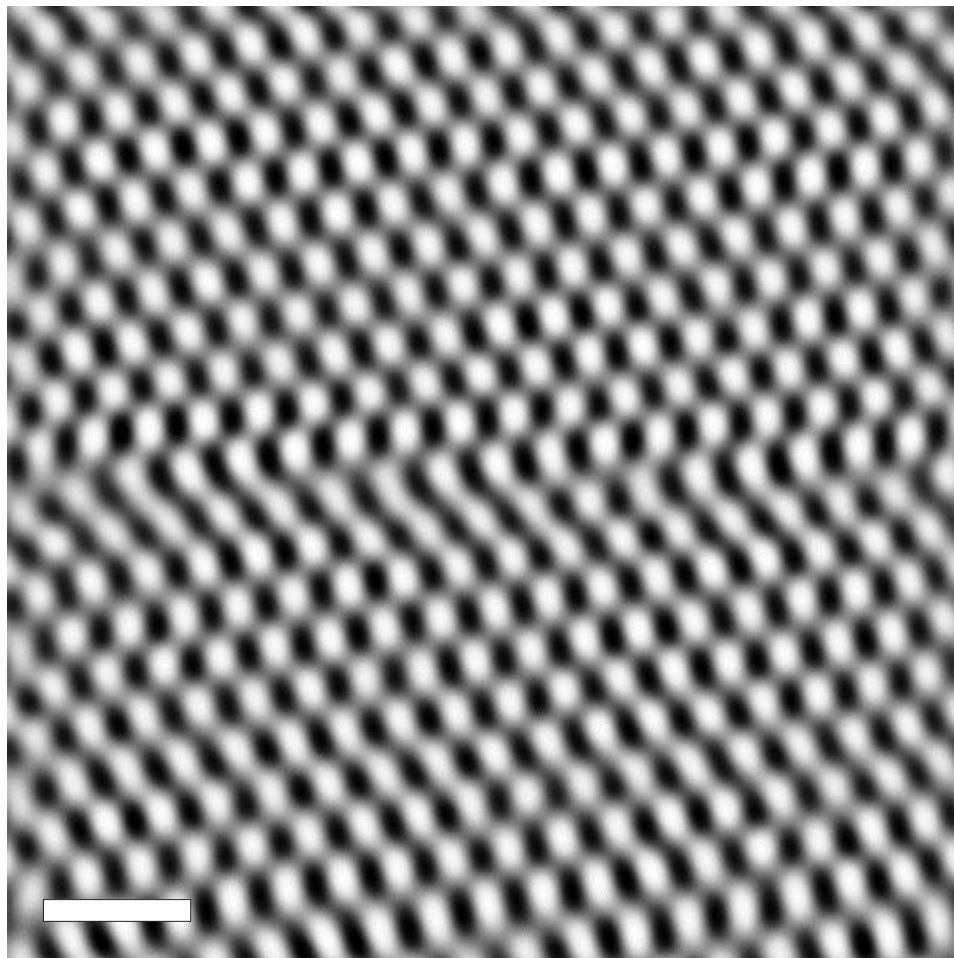


Figure 5: Current UHV STM image of the atomically resolved basal plane of in-air cleaved covellite. The scale bar represents 10 Å and the tunneling conditions were -0.6 V bias and 1 nA setpoint current.

At this point, a unique assignment of bright and dark sites to their respective atomic sites cannot be made. This is primarily due to the problem of not knowing whether surface states are present. For example, at negative bias voltage, STM is most sensitive to a small energy range of occupied states closest to the sample Fermi level (Hamers, 1993). In the absence of surface states, our theoretical calculations predict that these would be dominantly S 3p states and negative bias voltage images should show S sites as bright spots. In contrast, if Cu dangling bonds are present, tunneling current will primarily arise from partially filled Cu *d* states located near mid-gap, causing Cu sites to be brighter than S sites. Furthermore, it should be noted that although we have predicted that surface Cu sites should project from the surface slightly above the S layer, the above arguments should hold true.

### Scanning Tunneling Spectroscopy

I(V) tunneling spectra in UHV were collected concurrently while imaging at atomic resolution on samples cleaved in air to elucidate the local electronic structure in more detail. Spectra were collected with the feedback loop off under conditions of constant tip-sample separation (relatively large loop gain, slow scan rate) using a voltage ramp of -0.8 to +1 at every 40<sup>th</sup> imaging point (Figure 6a). Spectra that were found to occur directly over bright and dark sites were grouped and averaged. Figure 6b shows the average spectra of 16 curves collected over bright sites and 15 curves collected over dark sites. The curves collected over bright and dark sites are statistically indistinguishable. The lack of relative differences in these spectra may be principally related to the fact that the spectroscopic energy resolution is can be markedly decreased when the tip is very close to the sample surface, *i.e.* during atomically resolved imaging (Avouris *et al.*, 1991; Chen, 1994). That is to say that the tip wavefunction perturbs the surface electronic structure so as to smear out distinctive site specific features. Although this may be true, the I(V) curves divulge some additional information about the surface electronic structure. The general shape of the spectra exhibits a strong asymmetry, *i.e.* the current rises exponentially as a function of bias voltage at negative bias, and is “sluggish”

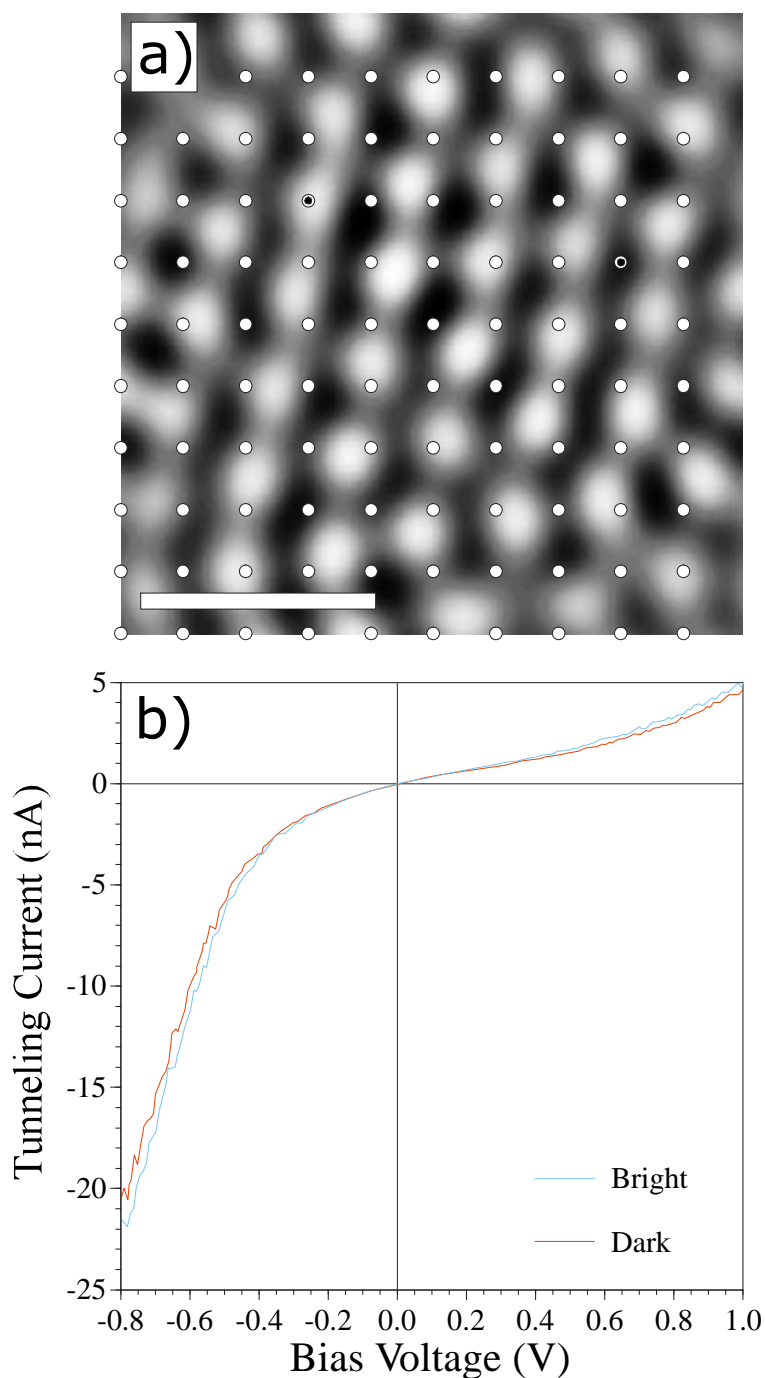


Figure 6: a) Atomic-scale current UHV STM image of the {001} surface of in-air cleaved covellite. The tunneling conditions were  $-0.2\text{V}$  bias and  $1\text{ nA}$  setpoint current.

The scale bar represents  $10\text{ \AA}$ . White dots represent the locations of  $I(V)$  tunneling spectroscopy points collected simultaneously with the image. Spectra that happened to be collected directly over bright and dark sites in the images, *e.g.* where the white dots are filled in, were averaged and are shown in b).

to rise at positive bias. This rectifying behavior is due to tip induced changes in the positions of bulk bands at the surface of a semiconductor in tunneling contact with a metal, otherwise known as tip induced band bending (Kaiser *et al.*, 1988; Weimer *et al.*, 1989). Furthermore, the sense of rectification is indicative of the majority charge carrier type in the bulk sample. The I(V) curves collected in this study are characteristic for *n*-type conduction (Kaiser *et al.*, 1988).

These concepts and their effect on the tunneling current are diagrammatically explained in Figure 7, with reference to arguments presented in Kaiser *et al.* (1988). Thermal equilibration between the metal tip and an *n*-type semiconducting sample results in the formation of a Schottky barrier ( $\phi_B$ ) (e.g. Sze, 1981) (Fig. 7b). Under conditions of applied bias, the height of the barrier is modified by the bias voltage, resulting in an increased barrier at positive bias (Fig. 7c) and a decreased barrier at negative bias (Fig. 7d). Electrons tunneling across the gap will originate from the highest occupied states of either the tip (positive bias) or from the sample (negative bias). In an *n*-type sample, it is assumed that the electrons in the highest occupied states are the majority carriers populating the conduction band minimum (Fig. 7b). As tunneling electrons must be thermally excited over the barrier, the barrier height will largely control the magnitude of the tunneling current. Thus, during the collection of I(V) spectra, the sluggish rise in the tunneling current at positive bias voltage can be attributed to a continuously increasing Schottky barrier, whereas at negative bias, the barrier is reduced and the tunneling current rises exponentially.

Tip induced modifications of the band bending at the surface are only significant on band gap surfaces, *i.e.* no surface states (Kaiser *et al.*, 1988). Surfaces with a high concentration of dangling bonds tend to be immune to electric field induced changes in the band bending during the voltage ramp because occupied surface states screen the semiconductor bulk states from the varying potential. This observation permits the conclusion that the surface imaged in Figure 6a and the spectra in Figure 6b were collected on a surface which was essentially free of

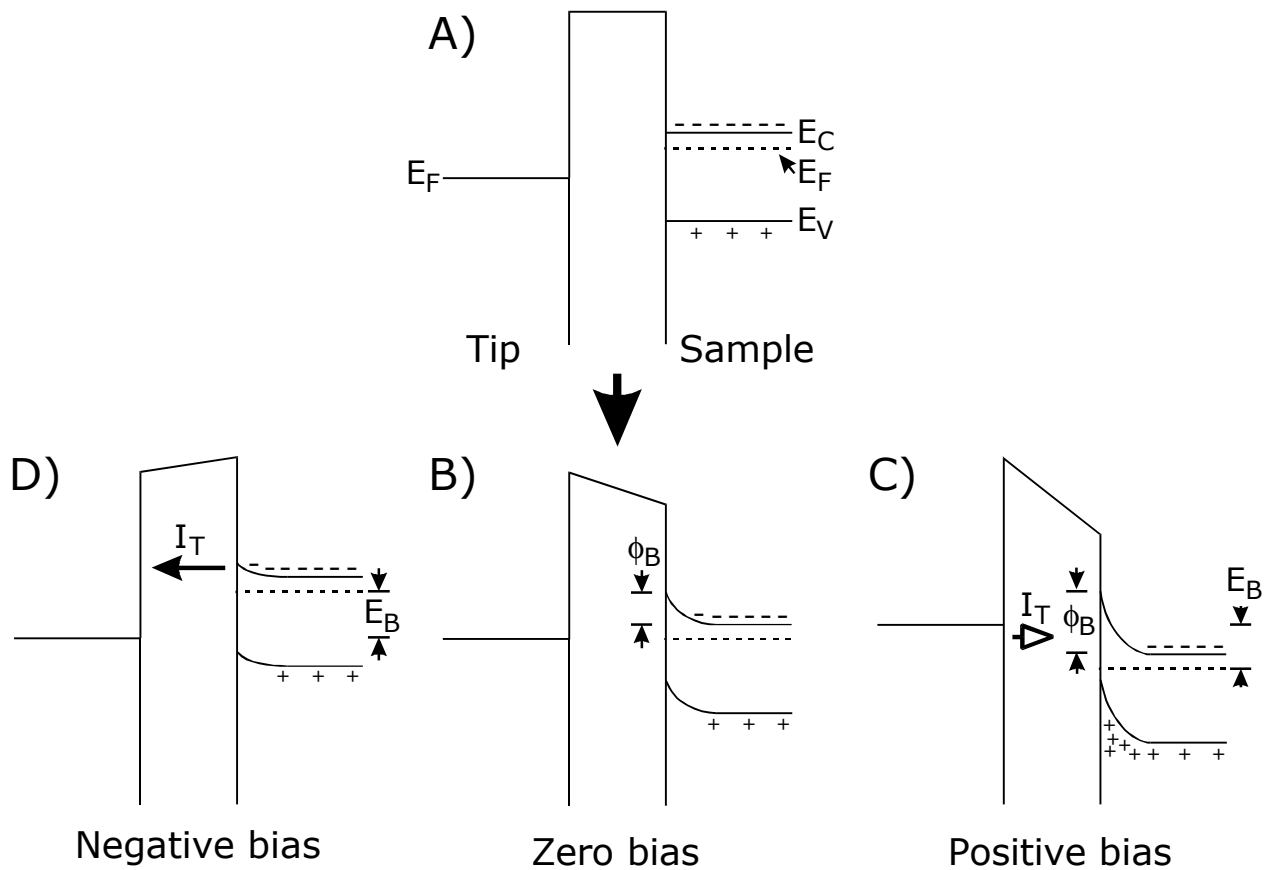


Figure 7: Schematic band structure diagrams modeling the tip-covellite tunneling contact. a) Thermal disequilibrium between tip and *n*-type sample.  $E_C$  and  $E_V$  are the conduction and valence band edges, respectively. b) The zero-bias tip-sample tunneling contact results in the upward bending of the bulk bands at the surface of the sample, forming a Schottky barrier ( $\phi_B$ ) (Sze, 1981). Under conditions of applied bias, the barrier is increased at positive sample bias (c), and decreased at negative bias (d). As electrons must be initially thermally excited over the barrier, the tunneling current is impeded at positive bias (open arrow) (c), but less so at negative bias (solid arrow) (d).

dangling bonds and thus, were most likely collected on the surface terminated by the trigonally coordinated Cu layer. Moreover, based on arguments presented above, it can now be stated that the bright spots in the image shown in Figure 6a are most likely S sites, with the tunneling current derived primarily from occupied S 3p states. The rectifying behavior of the tunneling spectra allows these conclusions to be uniquely drawn. Similar attempts to “identify” the other possible exposed surface structure using the tunneling spectroscopic “signature” have, so far, been unsuccessful.

### SUMMARY

Covellite is predicted to cleave Cu-S bonds along {001} because the S-S bond is predicted to be significantly stronger. The {001} surface can have two different, equally likely, exposed layers. LEED patterns indicate that these surfaces are not laterally reconstructed. The surface comprised of trigonal pyramidal groups of former Cu tetrahedra is expected to have *d* orbital dangling bond surface states. The surface comprised of trigonal planar Cu groups is not. *Ab-initio* periodic calculations of the 3 dimensional structure show that Cu is monovalent in both tetrahedral and trigonal planar sites, consistent with previous work. Similarly, calculations of the total DOS are in good agreement with UPS valence band spectra of freshly cleaved samples of covellite. Projected DOS calculations indicate that the highest occupied states are predominantly S 3p states and lesser Cu 3d states. STM images of the surface comprised of trigonal planar Cu groups are expected to show S sites as bright spots at both small positive and negative bias voltages. Cu 3d dangling bonds on the other possible surface are likely to cause Cu sites to be brighter than S sites. Atomically resolved STM images of covellite {001} show a hexagonal array of bright spots, consistent with LEED patterns. STM images alone do not allow an identification of the different possible exposed surface structures. I(V) tunneling spectra collected simultaneously with atomically resolved images show a rectifying behavior indicative of a lack of dangling bond states in the bulk band gap. This surface electronic

characteristic was used to uniquely differentiate between exposed surface structures on covellite.

### REFERENCES CITED

- Avouris, Ph., Lyo, I.W., and Bozso, F. (1991) Atom-resolved surface chemistry: The early steps of Si (111)-(7 × 7) oxidation. *Journal of Vacuum Science and Technology B*, 9, 424-430.
- Bader, R.F.W (1990) *Atoms in molecules: A quantum theory*, 438 p. Oxford Science Publications, Oxford.
- Becker, U., and Hochella, M.F., Jr. (1996) The calculation of STM images, STS spectra, and XPS peak shifts for galena: New tools for understanding mineral surface chemistry. *Geochimica et Cosmochimica Acta*, 60, 2413-2426.
- Buckel, W., and Hilsch, R. (1950) Zur supraleitung von kupfersulfid. *Zeitschrift fur Physik*, 128, 324-346.
- Chen, C.J. (1993) *Introduction to scanning tunneling microscopy*, 412 p. Oxford Science Publications, Oxford.
- Domashevskaya, E.P., Terekhov, V.A., Marshakova, L.N., Ugai, Ya.A., Nefedov, V.I., and Sergushin, N.P. (1976) Participation of d-electrons of metals of groups I, II, and III in chemical bonding with sulfur. *Journal of Electron Spectroscopy and Related Phenomena*, 9, 261-267.
- Dovesi, R., Saunders, V.R., Roetti, C., Causà, M., Harrison, N.M., Orlando, R., and Aprà, E. (1996) *CRYSTAL95 user's manual*, 170 p. University of Torino, Torino.
- Evans, H.T., and Konnert, J.A. (1976) Crystal structure refinement of covellite. *American Mineralogist*, 61, 996-1000.
- Evert, V., Hock, K.-H., Fiechter, S., and Tributsch, H. (1998) Electronic structure of FeS<sub>2</sub>: The

- Fjellvåg, H., Grøvdal, F., Stølen, S., Andersen, A.F., Müller-Käfer, R., and Simon, A. (1988) *Zeitschrift für Kristallographie*, 184, 111.
- Folmer, J.C.W., and Jelinek, F. (1980) The valence of copper in sulphides and selenides: an X-ray photoelectron spectroscopy study. *Journal of the Less-Common Metals*, 76, 153-162.
- Frenzel, G. (1959) Idait und blaubleibender covellin. *Neues Jahrb. Mineral Abh.*, 93, 87-132.
- Gatti, C. (1997) TOPOND96 User's Manual, 15 p. CNR-CSR SRC Milano, Italy.
- Goble, R.J. (1985) The relationship between crystal structure, bonding and cell dimensions in the copper sulfides. *Canadian Mineralogist*, 23, 61-76.
- Hamers, R.J. (1993) Methods of tunneling spectroscopy with the STM. In D.A. Bonnell, Ed., *Scanning tunneling microscopy and spectroscopy: Theory, techniques, and applications*, p. 51-103. VCH, New York.
- Hamers, R., Tromp, R., and Demuth, J. (1987) Electronic and geometric structure of Si (111)-(7 × 7) and Si (001) surfaces. *Surface Science*, 181, 346-355.
- Higgins, S.R., and Hamers, R.J. (1996) Morphology and dissolution processes of metal sulfide minerals observed with the electrochemical scanning tunneling microscope. *Journal of Vacuum Science and Technology B*, 14, 1360-1364.
- Hochella M.F., Jr., (1990) Atomic structure, microtopography, composition, and reactivity of mineral surfaces. In *Mineral-water interface geochemistry*, *Reviews in Mineralogy*, 23, 87-132.
- Junta-Rosso, J.L., and Hochella, M.F., Jr. (1996) The chemistry of hematite {001} surfaces. *Geochimica et Cosmochimica Acta*, 60, 305-314.
- Kaiser, W.J., Bell, L.D., Hecht, M.H., and Grunthaner, F.J. (1988) Scanning tunneling microscopy characterization of the geometric and electronic structure of hydrogen-terminated silicon surfaces. *Journal of Vacuum Science and Technology A*, 6, 519-523.

- Li, D., Bancroft, G.M., Kasrai, M., Fleet, M.E., Feng, X.H., Yang, B.X., and Tan, K.H. (1994) S K- and L-edge XANES and electronic structure of some copper sulfide minerals. *Physics and Chemistry of Minerals*, 21, 317-324.
- Liang, W., and Whangbo, M.-H. (1993) Conductivity anisotropy and structural phase transition in covellite CuS. *Solid State Communications*, 85, 405-408.
- Lichanot, A., Apra, E., and Dovesi, R. (1993) Quantum mechanical Hartree-Fock study of the elastic properties of Li<sub>2</sub>S and Na<sub>2</sub>S. *Physica Status Solidi B*, 177, 157-163.
- Meissner, W. (1929) Messungen mit hilfe von flüssigem helium. V. supraleitung von kupfersulfid. *Zeitschrift fur Physik*, 58, 570-572.
- Nakai, I., Sugitani, Y., Nagashima, K., and Niwa, Y. (1978) X-ray photoelectron spectroscopic study of copper minerals. *Journal of Inorganic and Nuclear Chemistry*, 40, 789-791.
- Narbutt, K.I. (1974) X-ray K $\alpha$ <sub>1,2</sub> and K $\beta$  spectra of sulfur atoms contained in minerals and certain chemical compounds. *Izvestiia Akademii nauk SSSR. Serii fizicheskai*, 38, 104-113.
- Nemnonov, S.A., and Mikhailova, S.S. (1974) X-ray K $\beta$ -spectra of sulfur in nickel, copper, and zinc monosulfides. *Izvestiia Akademii nauk SSSR. Serii fizicheskai*, 38, 56-58.
- Oftedal, I. (1932) The crystal structure of covellite. *Zeitschrift fur Kristallographie*, 83, 9-25.
- Rosso, K.M, and Hochella, M.F., Jr. (submitted) Atomically resolved electronic structure of pyrite {100} surfaces: An experimental and theoretical investigation with implications for reactivity.
- Shuey, R.T. (1975) *Semiconducting ore minerals*, 415 p. Elsevier Scientific, Amsterdam.
- Sugiura, C., Gohshi, Y., and Suzuki, I. (1974) Sulfur K $\beta$  X-ray emission spectra and electronic structures of some metal sulfides. *Physical Review B*, 10, 338-343.
- Sze, S.M. (1981) *Physics of semiconductor devices*, 868 p., Wiley, New York.

- Tossell, J.A. (1978) Theoretical studies of the electronic structure of copper in tetrahedral and triangular coordination with sulfur. *Physics and Chemistry of Minerals*, 2, 225-236.
- Towler, M.D., Dovesi, R., and Saunders, V.R. (1995) Magnetic interactions and the cooperative Jahn-Teller effect in  $\text{KCuF}_3$ , *Physical Review B*, 52, 10150-10159.
- Vaughan, D.J., and Tossell, J.A. (1980) The chemical bond and the properties of sulfides minerals: I. Zn, Fe and Cu in tetrahedral and triangular coordinations with sulfur. *Canadian Mineralogist*, 16, 157-163.
- Weimer, M., Kramar, J., and Baldeschwieler, J. (1989) Band bending and the apparent barrier height in scanning tunneling microscopy. *Physical Review B*, 39, 5572-5575.
- Zangwill, A. (1988) *Physics at surfaces*, 454 p. Cambridge University Press, Cambridge.

## **Appendix**

### ***SiO and BeO bonded interactions: A comparison of crystalline, molecular and experimental electron density distributions***

#### **ABSTRACT**

Bond critical point properties for the SiO bonds of the silica polymorph coesite, calculated for representative  $\text{H}_{12}\text{Si}_5\text{O}_{16}$  molecular moieties of the mineral with molecular wave-functions, are compared with those calculated for a bulk coesite crystal with crystalline wavefunctions. The calculated properties for the moieties and the crystal are in better agreement than they are with those observed in an X-ray diffraction experiment. A similar result was found for the BeO bonds in bromellite (BeO). The poorer agreement between the observed and calculated properties can be ascribed, at least in part, to the difficulty in determining accurate electron density distributions with X-ray diffraction intensity data recorded for nearly perfect crystals.

As the SiOSi angles in coesite increase and the SiO bond lengths shorten, there is a progressive build-up in the calculated electron density along the bonds. This is accompanied by an increase in the curvatures of the electron density both perpendicular and parallel to each bond. Although small in value, the cross-sections of the bonds become more circular as the angle increases to  $180^\circ$ . Also, the bonded radius of the oxide anion decreases as the SiO bond length decreases and the fraction of *s*-character of the bond increases.

The results of this study add to the body of evidence that indicates that the bonded interactions and properties of a number of rock forming silicates are governed primarily by short-range forces. A knowledge of the forces is central to our understanding of the interactions that govern the structure, stability, properties, solid state reactions, surface reactions and phase transformations of minerals. The software (CRYSTAL95 and TOPOND) used in this study to

calculate the bond critical properties is bound to shed considerable light on these nature of these forces and the crystal chemistry and the properties of minerals.

## INTRODUCTION

### **Electron density distributions and the chemical bond.**

The electron density distribution,  $\rho(r)$ , of a bonded array of atoms incorporates all of the information that defines the structure, stability and reactivity of the array (Kraka and Cremer, 1990). Thus, a study of the electron density distribution is an important undertaking in our quest for understanding the properties and reactions at the atomic level. In an important series of papers, Bader (1990) and his coworkers found that important insights into the properties and reactivities of a large variety of molecules can be obtained by evaluating the gradient,  $\nabla\rho(r)$ , and the Laplacian,  $\nabla^2\rho(r)$ , of the electron density distributions. They found, for example,  $\nabla\rho(r)$  provides an observable construct in the electron density distribution for studying a chemical bond, a concept that chemists in the past have regarded as an unobservable. By mapping the gradient vector field of  $\rho(r)$ , it was discovered that each pair of bonded atoms is connected by a unique line along which the electron density is a maximum with respect to any neighboring line in the field. Such a line defines a line of atomic interaction referred to as a bond path. This line of maximum electron density manifests itself in a plane through the atoms as a ridge of electron density. The point along the ridge where  $\rho(r)$  is a minimum defines a bond critical point, bcp, denoted  $r_c$  where  $\nabla(r) = 0$ . In addition, the distance between each atom and  $r_c$ , measured along the bond path, defines the bonded radius of the atom in the direction of the bonded interaction. As demonstrated by Bader and Essén (1984), the existence of a bond path connecting two atoms satisfies the necessary and sufficient condition that the pair of atoms is bonded. When a bond is broken, the bond path vanishes, but it reappears when the bond reforms (Bader *et al.*, 1983). Thus, by counting the number of bond paths that radiate from each

atom, the number of bonds and the coordination number of each atom in a structure can be uniquely determined in a simple and straightforward way.

### Properties of the Laplacian

$\nabla^2\rho(r)$  delineates those regions of a bonded array where the electron density is locally concentrated and depleted relative to the average value. Bader (1990) has shown for regions where  $\rho(r)$  is locally concentrated that the local potential energy density dominates the local electronic energy density and the electron density is tightly bound and compressed above the average value. In regions where it is locally depleted, the local kinetic energy density dominates and the electron density is expanded relative to its average distribution. While the electron density distribution of an isolated atom is characterized by a single maximum in the distribution that decays exponentially with distance from its nucleus, the  $\nabla^2\rho(r)$  distribution consists of series of alternating, concentric shells of local concentration and depletion that reflect the shell structure of the atom with the outermost shell corresponding to the valence shell. The local concentrations in the  $\nabla^2\rho(r)$  distribution of the valence shell not only provide a mapping of the non-bonded lone electron pairs of the Gillespie model (1972) of an atom but also a mapping of the bonded electron pairs of the Lewis model. The location of such sites is important because they provide a template delineating regions of a bonded array that may be susceptible to electrophilic attack and important clues for the construction of potential transition state structures and reaction paths. For example, the approach of the reactants in a Lewis acid-base can be predicted by aligning regions of local charge concentration with a region of local charge depletion (Gatti *et al.*, 1992).

### Diagnostics of an electron density distribution

During the past decade, Bader's (1991) strategies have made important contributions to our understanding of the bonded interactions and reactions in molecules. By mapping those regions where  $\nabla^2\rho(r) < 0$  together with an evaluation of the properties of the electron density

distributions at the point  $r_c$  between bonded atoms, important information has been obtained for a large variety of molecules including bond type and order,  $\pi$  bond character, electron delocalization, bent bond character, strain energy and bonds that are susceptible to cleavage. For example, the partial double CC bonds in such molecules as benzene and ethylene have been found to be elliptical in cross section, a feature that has been ascribed to the formation of  $\pi$  bonds, the greater the ellipticity, the greater the partial  $\pi$ -character of the bonds. However, bonds with unusually large ellipticities and highly curved bond paths have been shown to be strained, to destabilize a structure and to be susceptible to rupture. (Bader, 1990). On the one hand, a sharp positive curvature of the electron density along a bond path at  $r_c$  is believed to impart a 'stiffness' to the bond making it resistant to change. On the other, a bond with a large accumulation of electron density at  $r_c$  and a smaller curvature of the electron density along the bond path is believed to be less resistant to change and more easily perturbed (Bader, 1990). In addition, sites prone to electrophilic and nucleophilic activity have been used to delineate structure diagrams that embody information concerning possible molecular structures and their possible changes (Kraka and Cremer, 1990). In short, a great deal of insight is bound to be gained about the bonded and surface interactions, the structure and the stability of minerals by studying the topological properties of their electron density distribution, using Bader's (1990) strategies.

## Goals

Until now, the efforts in the exploration and study of the local structural properties (bond length, bond strength, angle variations and force constants) of minerals has been restricted primarily to calculations on representative fragments of mineral structures (Gibbs, 1982; Hill *et al.*, 1994; Gibbs *et al.*, 1998; Gibbs and Boisen, 1998). Despite the small sizes of the fragments, the calculations have not only provided a good account of the properties of chemically related crystalline materials, but they have also provided important insight into the bonded interactions of the bridging groups that play a central role in the crystal chemistry of the silica

polymorphs, silicates and siloxanes. With the development of periodic codes for bulk crystals that include a calculation of the topological properties of electron density distribution, we now have the opportunity to compare and contrast the electron density distributions and bond critical point properties of both molecules and crystals at a fundamental level.

Therefore, the goal of this study is to examine the connection between the electron density distribution and the bcp properties of the bonds in a crystal and a representative molecule. In exploring this connection, the bcp properties of the electron density distribution of the SiO bonds in the high pressure silica polymorph coesite were calculated using density functional theory with crystalline wavefunctions corrected for electron correlation and exchange. The properties provided by the calculations will be compared with those calculated for representative molecules using a comparable basis set and molecular orbital methods as well as those observed in an X-ray diffraction experiment (Downs, 1995; Geisinger *et al.*, 1987). One goal of the study will be to compare the electron density distribution calculated for crystalline coesite with that calculated for representative molecules and to see whether the trends in the properties calculated for the molecules conform with those calculated for the crystal. A second goal will be to see how well the two calculated data sets agree with the observed bcp properties.

## CALCULATED AND OBSERVED BOND CRITICAL POINT PROPERTIES

### Model crystal

Coesite is an ideal crystal for studying the bonded interactions between Si and O. For one reason it is chemically simple in that it only contains Si and O atoms in a ratio of one to two. For another, it consists of a relatively simple framework of corner sharing tetrahedra with two nonequivalent silicate tetrahedra, Si(1)O<sub>4</sub> and Si(2)O<sub>4</sub>, with eight nonequivalent SiO bonds and twelve nonequivalent OSiO and five nonequivalent SiOSi valence angles (Zoltai and Buerger,

1959). In addition, the bond lengths,  $R(\text{SiO})$ , vary between 1.595 and 1.622 Å while the SiOSi angles between the silicate tetrahedra vary between 137 and 180°. On the other hand, the OSiO angles show little variation, ranging between 108.0 and 110.5°. Despite the small range of bond lengths, they correlate with the observed SiOSi angles (Gibbs *et al.*, 1976), with  $R(\text{SiO})$  decreasing linearly with  $f_s(\text{O})$  (Figure 1), the fraction of  $s$ -character of the bond:  $f_s(\text{O}) =$

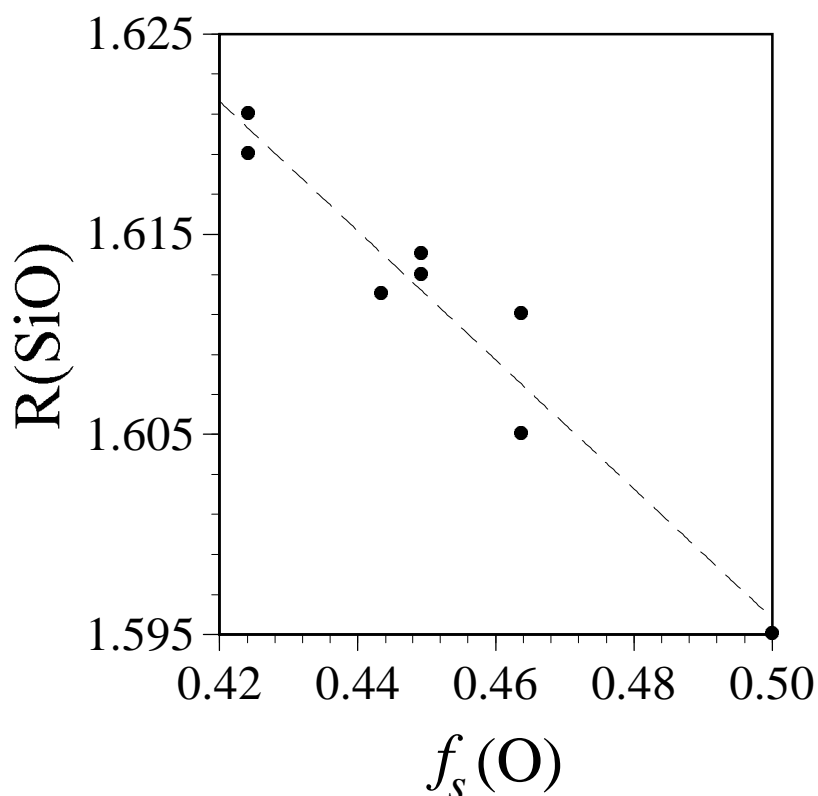


Figure 1: Plot of the observed SiO bond length in coesite,  $R(\text{SiO})$ , vs.  $f_s(\text{O})$ , the  $s$ -character of the bond.

$\cos\Theta/(\cos\Theta - 1.0)$  where  $\Theta = \langle \text{SiOSi} \rangle$  (Newton and Gibbs, 1980). The progressive shortening of the SiO bond length with increasing SiOSi angle has also been ascribed to a decrease in the radius of the oxide anion or to an increase in  $\pi$ -bonding. It will be of interest to see whether a calculation of the electron density distribution for a coesite crystal will provide a basis for understanding why the SiO bonds shorten as the angle widens and whether the shortening of

the bond can be ascribed to a decrease in the size of the oxide anion and a bonded interaction that involves  $\pi$ -bonding.

### Earlier calculations

In a recent study of the electron density distribution,  $\rho(\mathbf{r})$ , of the SiO bond, the geometries for a variety of silicate and siloxane molecules were optimized at the HF-SCF/6-311++G\* level. Using the strategies proposed by Bader (1990), electron density distributions were generated and bcp properties of the bonds were determined (Gibbs *et al.*, 1997). With decreasing SiO bond length, (1) the value of the electron density,  $\rho(r_c)$ , at  $r_c$  along the bond path increases, (2) the bonded radius,  $r_b(O)$ , of the oxide anion along the bond decreases, (3) the curvatures,  $|\lambda_1|$  and  $|\lambda_2|$ , of  $\rho(r_c)$  perpendicular to the bond path both increase, (4) the curvature,  $\lambda_3$ , of  $\rho(r_c)$  along the bond path increases and (5) the Laplacian of  $\rho(r_c)$ ,  $\nabla^2\rho(r_c)$ , increases. Thus, as the bond shortens, there is indicated to be a progressive build-up of electron density at  $r_c$  with a concomitant local concentration of the electron density both perpendicular to the path of the bond and in the direction parallel to the path away from  $r_c$  toward Si and O. Similar results were found for  $H_6Si_2O_7$  molecular models (Gibbs *et al.*, 1994) together with a progressive migration of  $r_c$  toward the oxide anion. Also, with increasing angle, the ellipticity of the bond,  $\varepsilon = (|\lambda_1|/\lambda_3 - 1.0)$ , tends to decrease to zero at  $180^\circ$ , a trend that can be ascribed to the formation of a very weak partial  $\pi$ -bond. Likewise, the bonded radius of the oxide anions decreases with increasing SiOSi angle and increasing  $s$ -character of the bond. The increase in the  $s$ -character not only suggests that the energy of the oxide anions in coesite decreases as the SiOSi angle widens, but also that they become more electronegative in character.

### Crystal calculations

To learn the extent to which the electron density distribution calculated for a bulk coesite crystal relates to the observed distribution and that calculated for representative molecules, calculations were completed for a crystal model of coesite using CRYSTAL95 (Dovesi *et al.*,

1996), a Hartree-Fock program that uses periodic boundary conditions to calculate wavefunctions for crystalline systems. The choice of the basis set in these calculations is critical for accurate and meaningful results. Gaussian basis functions commonly used in MO calculations are too diffuse to serve as suitable basis functions in crystal calculations; their use often results in an over-estimate of the overlap among the constituent orbitals and numerical instability. To avoid this problem, we used basis sets that were developed and optimized specifically for CRYSTAL95; these are available at the Crystal web site, <http://www.dl.ac.uk/TCS/Software/CRYSTAL> (June 11, 1998). The best performance was obtained using a 65-111G\* Gaussian basis set for Si (D'Arco *et al.*, 1993) and a 8-411G basis set for O (Dovesi *et al.*, 1991).

The calculations for coesite were completed using the cell dimensions, the space group type and the coordinates of the atoms reported by Downs (1995). The wavefunctions were generated in the calculation at the DFT level using the Kohn-Sham strategy together with the Lee-Yang-Parr and the Becke functionals, for electron correlation and exchange, respectively. The bond critical point properties of the calculated electron density distribution, generated from these wavefunctions, together with the Laplacian distribution were calculated using TOPOND (Gatti, 1997), companion software recently added to the CRYSTAL95 package. The bcp properties, computed with the software for each of the nonequivalent SiO bonds in coesite, are given together with the observed SiO bond lengths in Table 1 where they are compared with those calculated for  $\text{H}_{12}\text{Si}_5\text{O}_{16}$  molecules (Gibbs *et al.*, submitted) and those observed (Downs, 1996).

### **Molecular calculations**

The bcp properties for the molecules were obtained with wavefunctions calculated at the Becke3lyp/6-311G(2d,p) level (Frisch *et al.*, 1993). The calculations were completed on two  $\text{H}_{12}\text{Si}_5\text{O}_{16}$  molecules, one with the Si(1)O<sub>4</sub> and the other with the Si(2)O<sub>4</sub> silicate group of

coesite at its center. The geometries of the  $(\text{Si}_5\text{O}_{16})^{12-}$  moieties of the molecules were clamped to match the geometry of each of the moieties in coesite. The moieties were charged balanced by attaching a proton to each of the nonbridging oxide anions at a distance of 1.0Å to form molecules of  $\text{H}_{12}\text{Si}_5\text{O}_{16}$  composition with straight SiOH angles (Gibbs *et al.*, submitted). The bcp properties of the central silicate tetrahedron calculated for each molecule are given in Table 1 together with the lengths of the SiO bonds observed for coesite. The properties were calculated using a version of the AIMPAC series of programs (Biegler-Ednig *et al.*, 1980), generously supplied by Richard Bader and his research associates in the Chemistry Department at McMaster University.

### Observed electron density distribution

The experimental bond critical point data for coesite were obtained using the X-ray diffraction data measured by Geisinger *et al.* (1987) and the generalized scattering factor (GSF) method that generates a representative model of the total electron density distribution (Downs *et al.*, 1995). In the study, the eigenvalues and the eigenvectors of the Hessian of the model electron density distribution were determined at the critical point along each of the eight nonequivalent SiO bonds together with  $\rho(r_c)$ ,  $\lambda_1$ ,  $\lambda_2$ ,  $\lambda_3$ ,  $\nabla^2\rho(r_c)$  and  $r_b(\text{O})$  (Table 1).

## TRENDS BETWEEN CALCULATED AND OBSERVED BOND CRITICAL POINT PROPERTIES

### A comparison of molecular and crystal results

As observed by Gibbs *et al.* (1994) for several  $\text{H}_6\text{Si}_2\text{O}_7$  molecules, the bcp properties calculated for a coesite crystal are highly correlated with  $R(\text{SiO})$ . As  $R(\text{SiO})$  decreases,  $r_b(\text{O})$  decreases and  $\rho(r_c)$ ,  $|\lambda_1|$ ,  $|\lambda_2|$ ,  $|\lambda_3|$ , and  $\nabla^2\rho(r_c)$  each increase (Figure 2). In particular, with decreasing bond length and increasing SiOSi angle,  $r_b(\text{O})$  decreases from 0.952Å to 0.932Å while  $r_b(\text{Si})$  decreases to a lesser extent from 0.669Å to 0.663Å. Also, as the SiOSi

Table 2: Bond Critical Point Properties For SiO<sub>2</sub>.

Properties calculated for coesite:

R(SiO)	r <sub>b</sub> (O)	$\rho(r_c)$	$\lambda_1$	$\lambda_2$	$\lambda_3$	$\nabla^2 \rho(r_c)$
1.595	0.932	0.987	-6.63	-6.62	38.52	25.27
1.605	0.940	0.973	-6.47	-6.38	37.09	24.24
1.611	0.944	0.957	-6.32	-6.27	36.30	23.71
1.612	0.945	0.966	-6.42	-6.34	36.14	23.38
1.613	0.946	0.956	-6.33	-6.23	35.98	23.42
1.614	0.947	0.956	-6.30	-6.22	35.88	23.36
1.619	0.950	0.952	-6.28	-6.11	35.26	22.88
1.621	0.952	0.947	-6.24	-6.15	35.00	22.62

Properties calculated for H<sub>12</sub>Si<sub>5</sub>O<sub>15</sub> molecules:

1.594	0.931	1.025	-7.67	-7.66	38.18	22.85
1.606	0.940	1.011	-7.50	-7.44	36.52	21.58
1.610	0.943	0.999	-7.36	-7.31	35.87	21.21
1.612	0.944	1.001	-7.36	-7.30	35.66	21.00
1.612	0.944	1.007	-7.42	-7.32	35.67	20.92
1.613	0.945	0.997	-7.34	-7.26	35.47	20.87
1.619	0.947	0.990	-7.34	-7.23	35.21	20.63
1.622	0.952	0.988	-7.21	-7.12	34.32	19.98

Properties observed for coesite (Downs, 1995):

1.595	0.920	1.11	-7.5	-7.0	36.7	22.1
1.605	0.927	0.95	-6.7	-6.2	34.2	21.4
1.612	0.935	1.03	-7.2	-7.0	34.4	20.5
1.613	0.942	1.16	-8.1	-7.3	33.9	18.5
1.614	0.937	1.08	-7.1	-6.9	33.0	19.0
1.611	0.933	0.93	-6.9	-6.5	35.3	22.0
1.619	0.942	1.07	-7.2	-7.0	33.8	19.7
1.621	0.945	1.04	-7.2	-6.8	33.7	19.6

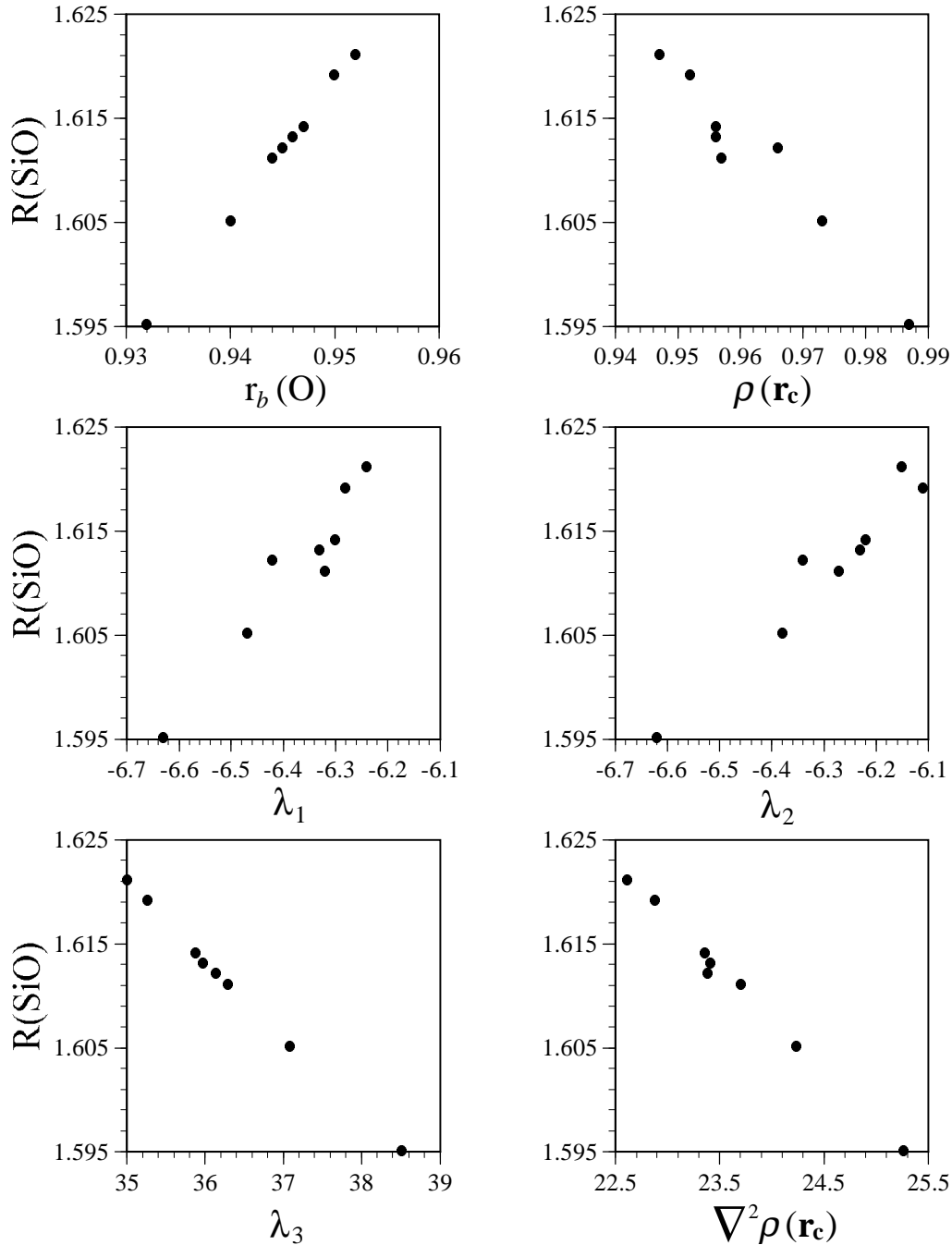


Figure 2: Scatter plots of the SiO bond lengths,  $R(\text{SiO})$ , observed for coesite vs. the bcp properties of the bonds calculated for the crystal;  $r_b(\text{O})$  is the bonded radius of the oxide anion,  $\rho(\mathbf{r}_c)$  ( $e/\text{\AA}^3$ ) is the electron density,  $\lambda_1$  and  $\lambda_2$  are the curvatures of  $\rho(\mathbf{r}_c)$  ( $e/\text{\AA}^5$ ) perpendicular to the bonds,  $\lambda_3$  is the curvature of  $\rho(\mathbf{r}_c)$  parallel to the bonds,  $\nabla^2 \rho(\mathbf{r}_c)$  ( $e/\text{\AA}^5$ ) is the Lap. of  $\rho(\mathbf{r}_c)$ .

angle in coesite increases, there is a progressive build-up of electron density at  $r_c$  and a progressive decrease in the size of the oxide anion. Thus, the shortening of the SiO bond with increasing SiOSi angle can be ascribed to both a build up of electron density in the bond and to a decrease in the size of the oxide anion. The bcp properties calculated for the two  $H_{12}Si_5O_{16}$  molecules correlate with  $R(SiO)$  (Fig. 3) in much the same way as they correlate with the bcp properties calculated for coesite. Not surprising, properties calculated for coesite are also highly correlated with those calculated for the central silicate tetrahedra of the two larger  $H_{12}Si_5O_{16}$  molecules (Fig. 4) (Gibbs *et al.*, submitted);  $r_b(O)$ ,  $\rho(r_c)$  and  $\lambda_3$  for both coesite and the  $H_{12}Si_5O_{16}$  molecules differ by less than 5%, on average, and follow the identity line. On the other hand, the values of  $\lambda_1$ ,  $\lambda_2$  and  $\nabla^2\rho(r_c)$  differ from those calculated for the molecules between 12 and 14%, on average. Indeed, Gatti *et al.* (1992) found much better agreement in a similar analysis of the bcp properties for L-alanine; the  $\nabla^2\rho(r_c)$  values generated for a molecular moiety isolated from the structure of L-alanine differs only in the third decimal place from those observed for the crystal. They also found that the calculated electron density distributions usually reproduce the experimental trends, but the absolute values of  $\rho(r)$  are 10 to 15% larger than the calculated densities. The high correlation between the molecular and crystal data calculated for coesite and the close correspondence in the molecule and crystal data for L-alanine indicates that the electron density distributions in these materials are governed, for the most part, by local forces. It also suggests that electron density distribution generated with molecular wavefunctions can provide a faithful representation of the distribution for a chemically similar crystal.

As noted above, Gibbs *et al.* (1994) observed that the ellipticity of the SiO bond is expected to be zero when the SiOSi angle is straight and both  $\pi$ -systems are involved in forming a bond (Cruickshank, 1961). Also,  $\epsilon$  is predicted to increase, as indicated above, as the angle narrows and the  $\pi$  system perpendicular to the SiOSi plane becomes dominant. The ellipticities for the

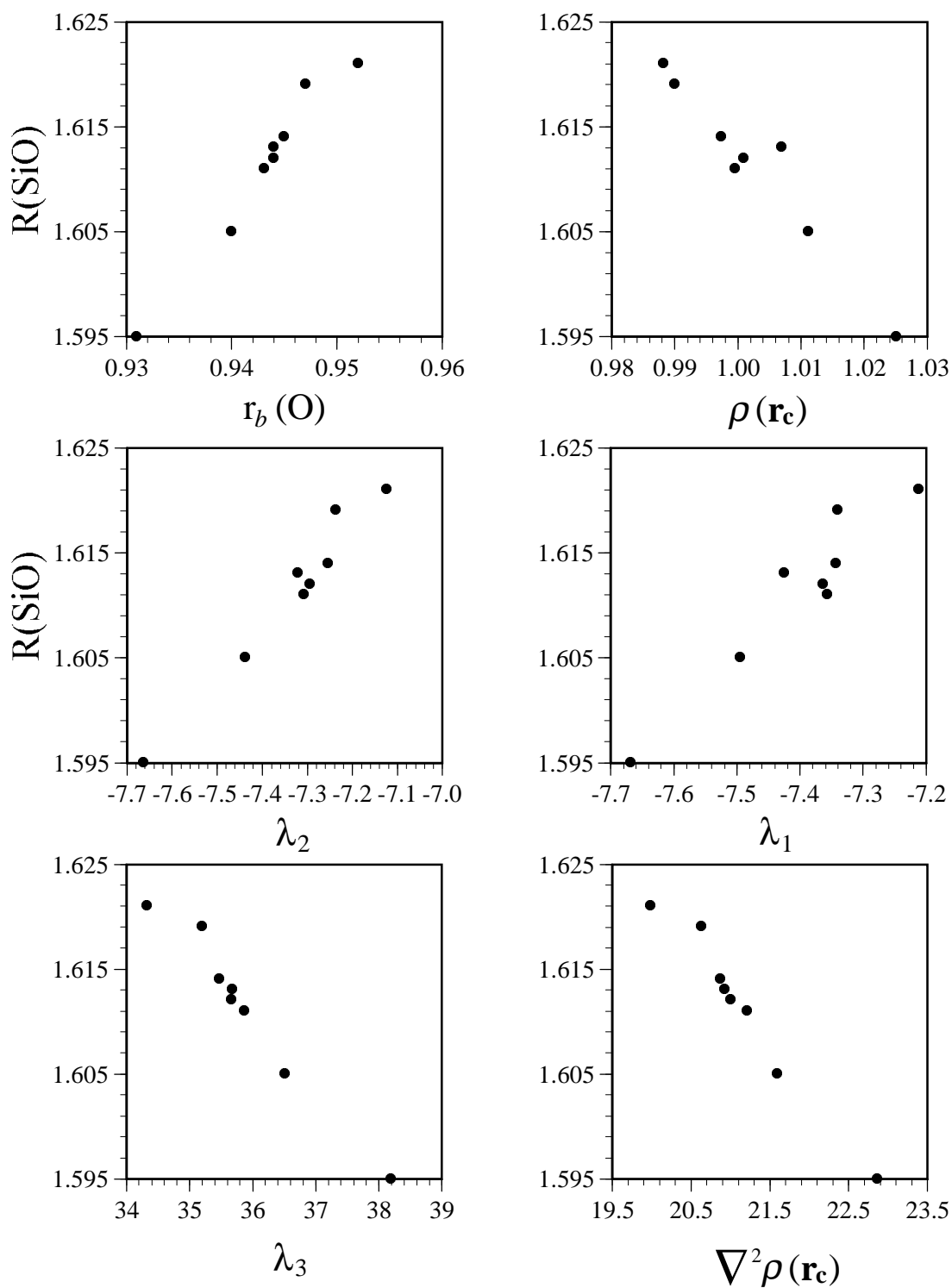


Figure 3: Scatter plots of the SiO bond lengths,  $R(\text{SiO})$ , observed for coesite vs. the bcp properties of the bonds calculated for two  $\text{H}_{12}\text{Si}_5\text{O}_{16}$  molecules; see Figure 2 caption for the definition of parameters

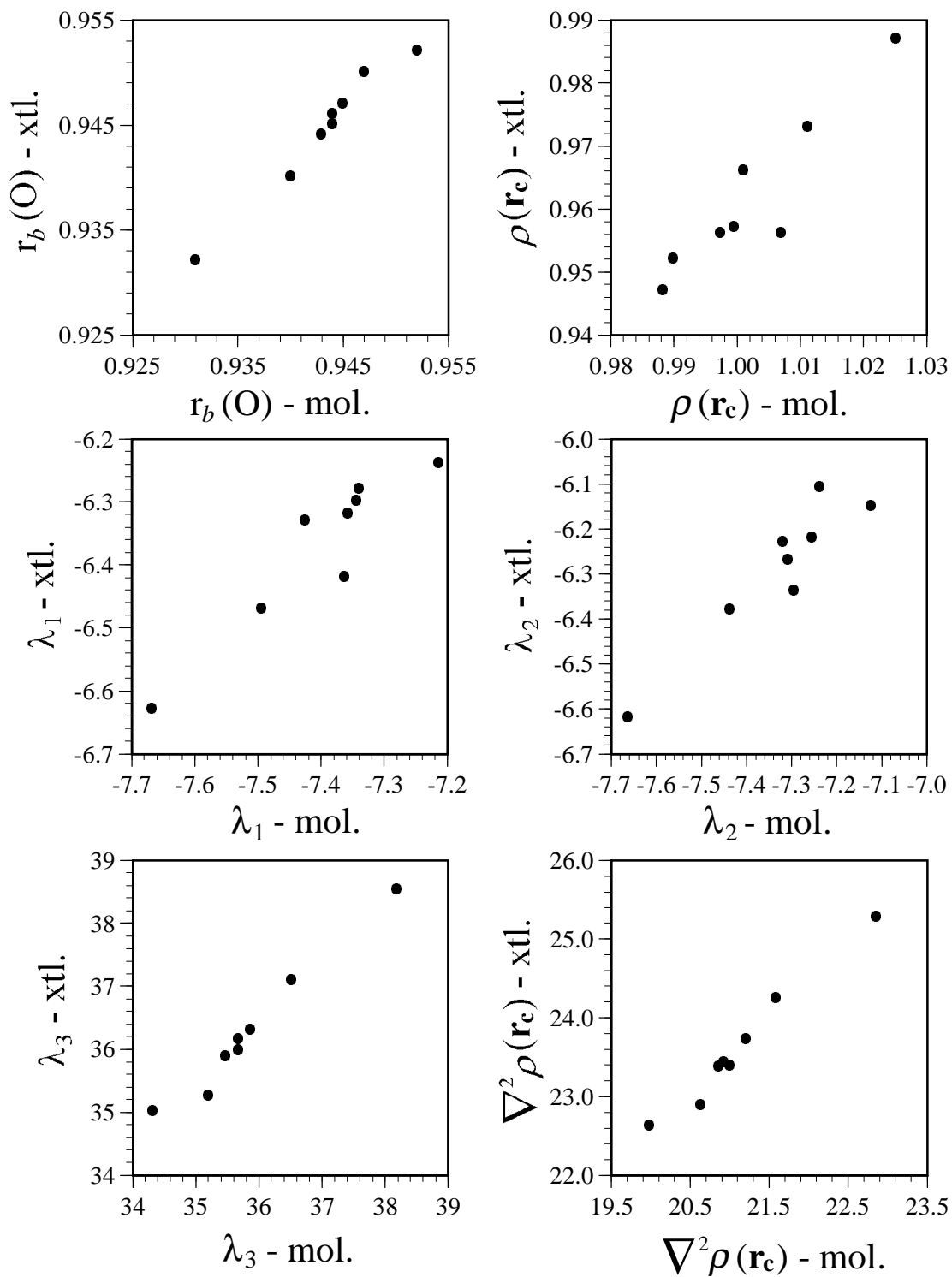


Figure 4: Scatter plots of the bcp properties calculated for a coesite crystal (xtl.) vs. those calculated for  $H_{12}Si_5O_{16}$  molecules (mol.).

SiO bonds, plotted against  $f_s(O)$  in Figure 5, show a small but systematic decrease in value as the SiOSi angle widens to  $180^\circ$  for both the molecules and the bulk crystal.

It is noteworthy that the SiOSi angles in the crystal also conform with the build-up of electron density in the bonds. The SiOSi angles between bonds of larger  $\rho(r_c)$ -values tend to be wider than those between bonds with smaller  $\rho(r_c)$ -values. Although bonds with larger  $\rho(r_c)$ -values in the Si(1)O<sub>4</sub> silicate tetrahedron tend to involve wider OSiO angles, no such relationship holds for the Si(1)O<sub>4</sub> tetrahedron (Gibbs *et al.*, 1977).

### **A comparison of observed and calculated bcp properties**

The bcp properties observed for coesite agree to within ~9%, on average, with those calculated for the crystal and to within 3%, on average, with those calculated for the molecules (Table 1). Of the observed bcp properties, only the bonded radius of the oxide anion,  $\lambda_3$  and  $\nabla^2\rho(r_c)$  correlate with those calculated (Fig. 6) while the remaining bcp properties show no correlation with the calculated values. Likewise, no correlation obtains between  $\epsilon$  and  $f_s(O)$  for the observed data (Fig. 5). This lack of agreement between the individual values observed and calculated for coesite may be related to problems encountered in recording the X-ray diffraction intensity data for the mineral and the difficulty in finding a suitable model for correcting the diffraction data for extinction effects (Geisinger *et al.*, 1987). As is well known, the intense, low angle intensity data, which embody most of the information content on the valence electrons, are most affected by extinction. Also, as extinction may be anisotropic, it is not uncommon for symmetry equivalent reflections in mineral data sets to differ from one another by as much as 60%. Thus, an averaging of the symmetry equivalent reflections, as done by Geisinger *et al.* (1987) in obtaining a set of intensity data for coesite, may account in part for the lack of agreement between the observed and calculated bcp properties.

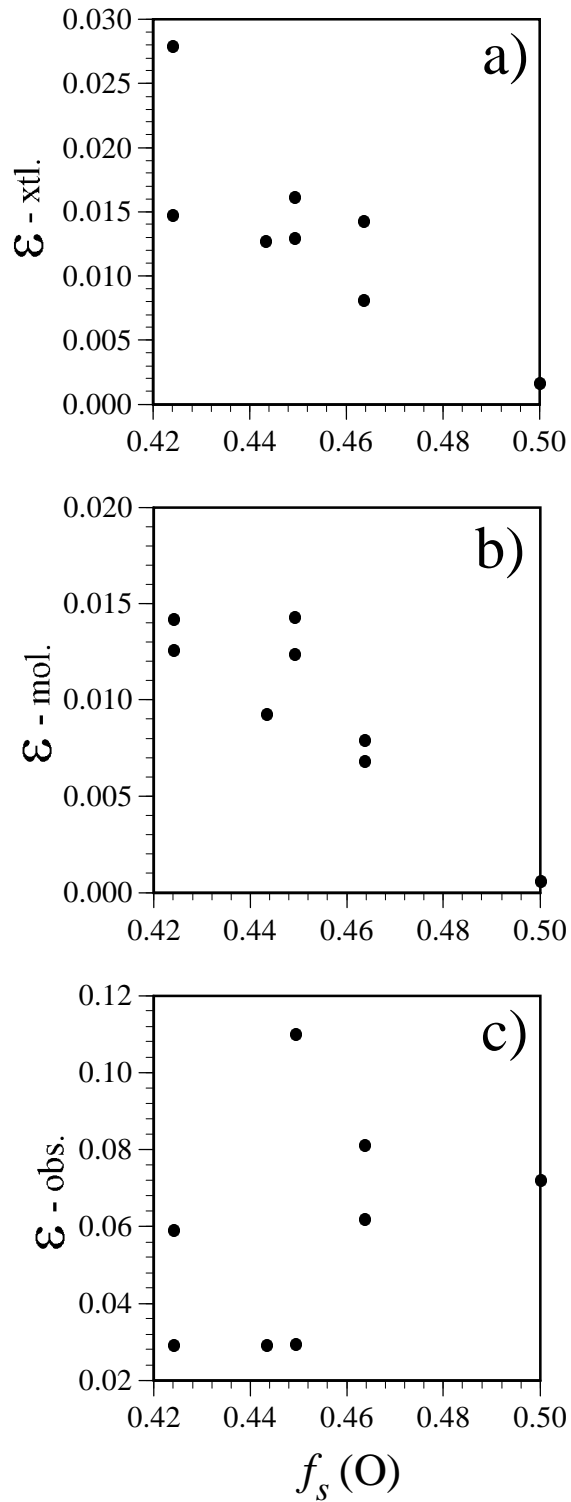


Figure 5: Scatter plots of the ellipticity,  $\epsilon$ , of the SiO bonds in coesite (a) calculated for a coesite crystal, (b) calculated for  $\text{H}_{12}\text{Si}_5\text{O}_{16}$  molecules, and (c) observed for coesite vs.  $f_s(\text{O}) = \cos\Theta/(\cos\Theta-1.0)$  where  $\Theta = \langle\text{SiOSi}\rangle$ .

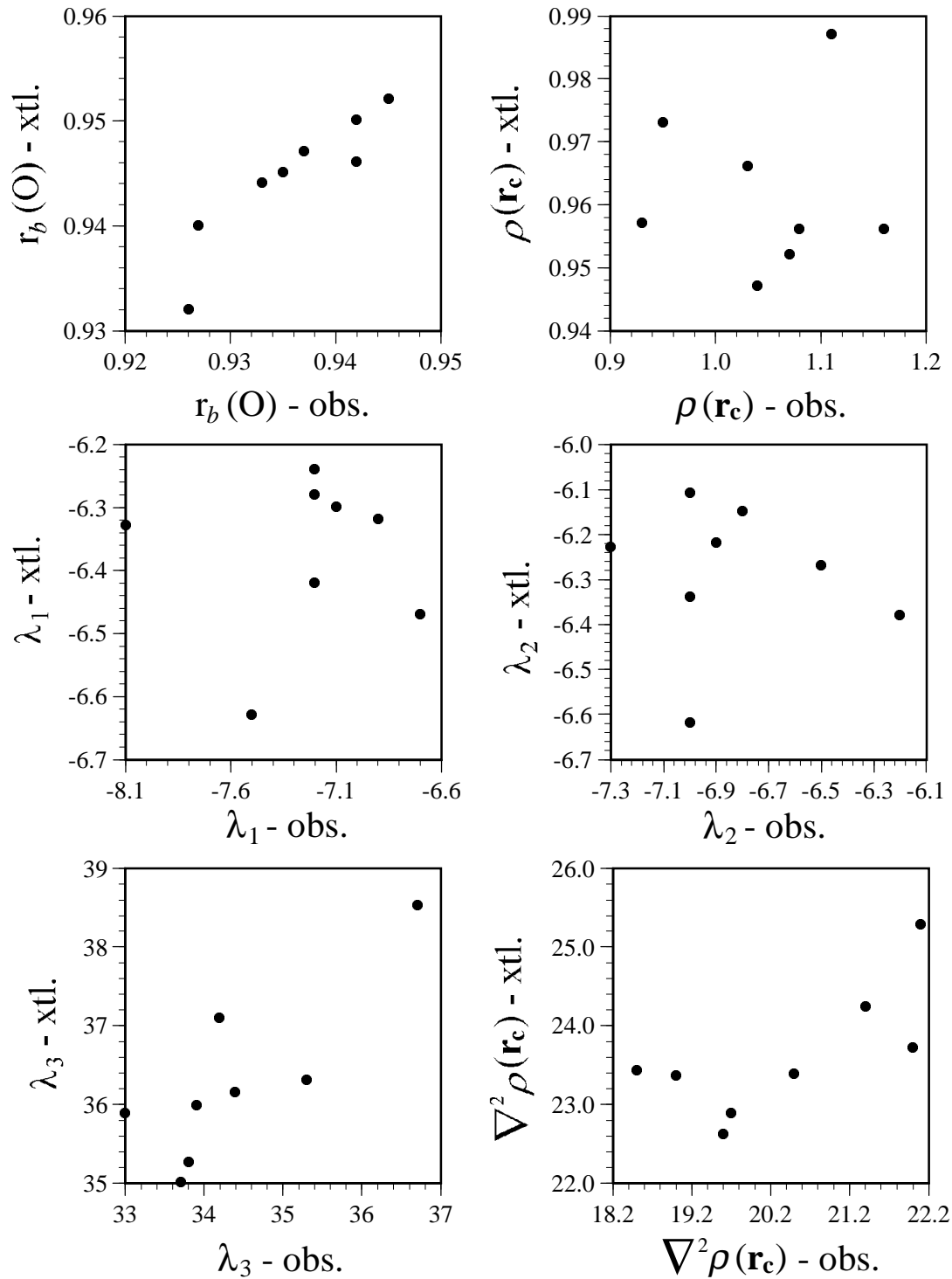


Figure 6: Scatter plots of the bcp properties calculated for a coesite crystal (xtl.) vs. those observed (obs.) (Downs, 1994).

## Calculations for BeO

For purposes of comparison, the bond critical point properties for the mineral bromellite, BeO, were also calculated using the CRYSTAL9S—TOPOND software and compared with those observed (Downs, 1991) and those calculated for the molecule  $\text{H}_6\text{BeO}_4$  ( $C_{3v}$  point group symmetry). The calculation for the crystal was completed using the cell dimensions, the coordinates of the atoms and the space group type reported by Downs (1991) for bromellite and an 8-411G Gaussian basis set for both Be and O. The bcp properties of the  $\text{H}_6\text{BeO}_4$  molecule were also calculated with MO methods at the Becke3lyp/6-311G(2d,p) level with the geometry of the  $\text{BeO}_4$  moiety of the molecule clamped at that observed for the  $\text{BeO}_4$  moiety in bromellite. The bcp properties obtained in these calculations are compared with those observed in Table 2. As observed for coesite, the calculated bonded radii for the oxide ion measured along the BeO bond for bromellite is in close agreement with that observed. However, the value of  $\rho(r_c)$  calculated for the bulk crystal is ~10% less than that observed whereas that calculated for the molecule falls within the range of observed values. The values of  $\lambda_1$  and  $\lambda_2$  calculated for both the crystal and the molecule are ~25% larger than observed while the values calculated for  $\lambda_3$  and  $\nabla^2\rho(r_c)$  are in reasonable agreement with those observed. Overall, the calculated bcp properties for the crystal and the molecule are in better agreement than either of the calculated data sets are with the observed properties.

With the bcp properties observed for bromellite and coesite, the electronegativities of both Si and O can be estimated (Boyd and Edgecomb, 1988; Hill *et al.*, 1997). As expected, the electronegativity values calculated for Be (1.3) is larger than that calculated for Si. The value calculated for Be is ~15% smaller than that (1.5) reported by Pauling's (1960) while that estimated for Si (1.8) in coesite is in exact agreement with Pauling's value.

Table 3: Bond Critical Point Properties For BeO.

Properties calculated for bromellite:

R(BeO)	$r_b(O)$	$\rho(r_c)$	$\lambda_1$	$\lambda_2$	$\lambda_3$	$\nabla^2\rho(r_c)$
1.655	1.074	0.48	-3.35	-3.35	17.33	10.60
1.647	1.067	0.49	-3.52	-3.52	18.00	10.96

Properties calculated for a  $H_6BeO_4$  molecule:

1.655	1.084	0.56	-3.08	-3.08	17.34	11.18
1.647	1.078	0.57	-3.20	-3.20	17.91	11.51

Properties observed for bromellite (Downs, 1991):

1.655	1.086	0.63	-4.67	-4.67	17.24	7.9
1.647	1.085	0.50	-4.90	-4.11	19.57	10.6

## DISCUSSION

With the recent release of the CRYSTAL95-TOPOND software (Dovesi *et al.*, 1991; Gatti, 1997), calculations comparable with those completed by Bader (1990) and his colleagues on molecules can now be completed for minerals. Indeed, such calculations are bound to provide new and important insights into the bonded interactions in a wide variety of minerals, ranging from silicates to sulfides. Not only can they highlight those bonds that are strained and susceptible to cleavage, but they can also pinpoint those regions on mineral surfaces that are prone to electrophilic and nucleophilic attack (Aray and Bader, 1996). The electron density distribution of a mineral can also be monitored to learn how the bcp properties change, how bonds are formed and broken and coordination numbers change with increasing pressure and temperature.

An accurate determination of an experimental electron density distribution for a mineral like coesite from X-ray diffraction data is a difficult task because such data is often fraught with

systematic errors such as extinction that are difficult to correct exactly. As has been seen in this study, when an X-ray diffraction experiment is completed for a mineral, the resulting electron density distributions (as in the case of coesite and bromellite) may be wanting and may not show the systematic trends that are generated by CRYSTAL95 and TOPOND. But, as the trends provided by this software are in good agreement with those generated in accurate MO calculations on molecules, we believe that the trends in the bcp properties, such as those presented in Figures 2 and 3, will closely mimic those provided by an error free set of diffraction data. Moreover, Gatti *et al.* (1992) not only found that the bcp properties observed for L-alanine are in good agreement with values calculated for the crystal, but also that the properties of a molecular moiety cut from the structure did not differ significantly from those of the crystal.

As more and more mineralogists use the CRYSTAL95-TOPOND software in their research efforts, a new effort in mineralogy is bound to unfold that is likely to result in important advances in our understanding of minerals, their properties and crystal chemistry and how the bonded interactions in minerals change with pressure and temperature. The calculations are also likely to improve our understanding of reactions mechanisms and twinning as well as providing new and important insights into solid state relations, polymorphic transformations and metastability.

Finally, the conviction that molecules can be used to model bonded interactions in crystals is not new. It is an old idea that was proposed more than 50 year ago by the well known solid state physicist J. C. Slater (1939) who, on the basis of the similarities of the geometries and rigidities of several aliphatic molecules and diamond, wrote that “A diamond is really a molecule of visible dimensions held together by just the same forces acting in small molecules.” Subsequently, with the determination of the structure of the gas phase molecule disilyl ether,  $\text{H}_6\text{Si}_2\text{O}$ , Almennigen *et al.* (1963) concluded that the bonding picture of the skeletal Si-O-Si

dimer of the molecule is similar to that in a silicate crystal because the geometry of the dimer ( $R(\text{SiO}) = 1.632\text{\AA}$ ;  $\angle\text{Si-O-Si} = 142.2^\circ$ ) is similar to that observed, on average, for a silicate crystal ( $R(\text{SiO}) = 1.626\text{\AA}$ ;  $\angle\text{Si-O-Si} = 144^\circ$ ). It is worthy of notice that an X-ray structure analysis of a disilyl ether crystal, synthesized at liquid nitrogen temperatures, shows that the geometry of the molecule in the crystal is statistically identical with that in the gas phase, despite differences between the forces acting on the atoms in the gas phase molecule and those in the crystal (Barrow *et al.*, 1979). In addition, a search of the literature shows that the average SiO bond length ( $1.634\text{\AA}$ ) and SiOSi angle ( $144^\circ$ ) observed for a variety of siloxane molecules are also similar to those observed for disilyl ether and the silicate crystals. Indeed, the structures of the condensed tetrahedral anions of organosiloxanes and silicates are so similar that they have been classified with the well known scheme used by Bragg to classify silicates (Noll, 1968). Further, as observed above, the calculated geometry, electron density distribution and the bcp properties of the distribution of the  $\text{Si}_5\text{O}_{16}$  skeleton of the  $\text{H}_{12}\text{Si}_5\text{O}_{16}$  molecule are strikingly similar to those calculated for coesite. Collectively, these results not only indicate that the force fields that govern the structures and electron density distributions of silicic acid molecules and silicate crystals are not all that different, but they also contribute to the body of data that indicates that the silica polymorphs can be viewed, as asserted earlier by Gibbs (1982), as giant molecules bound together by the same forces that bind the Si and O atoms of the silicate skeleton of a silicic acid molecule, despite the greater size of the former. It also provides a basis for understanding why the structures and the elastic properties of the silica polymorphs can be modeled with a molecule orbital based potential energy function (cf. Lasaga and Gibbs, 1987; Stixrude and Bukowinski, 1988; Tsuneyuki *et al.*, 1988; Gibbs *et al.*, 1988; van Beest *et al.*, 1990; Purton *et al.*, 1993; Boisen *et al.*, 1993) and why a large number of new silica structure types can be generated using simulated annealing strategies and a molecular potential energy function (Boisen *et al.*, 1994). As observed above, the body of evidence indicates that the forces that bind Si and O ions together in a silicate crystal can be treated as if localized as in a molecule. It also

serves as strong evidence that the chemically similar molecules can serve as useful models for studying bonded interactions in a wide range of materials (Gibbs, 1984; Lasaga and Gibbs 1990).

## REFERENCES

- Almennigen A, Bastiansen O, Ewing V, Hedberg K, Traetteberg M (1963) The molecular structure of disiloxane,  $(\text{SiH}_3)_2\text{O}$  Acta Chem Scand, 17, 2455-2460.
- Aray, Y. and Bader, R.F.W. (1996) Requirements for activation of surface oxygen atoms in MgO using the Laplacian of the electron density, Surface Science 351, 233-249.
- Bader, R.F.W. (1990) Atoms in molecules, Oxford Science Publications Oxford, UK.
- Bader, R.F.W. and Essén, H. (1984) The characterizations of atomic interactions Journal of Chemical Physics, 80, 1943-1960.
- Bader, R.F.W., MacDougall, P.J. and Lau, C.D.H. (1984) Bonded and nonbonded charge concentrations and their relation to molecular geometry and reactivity Journal of the American Chemical Society, 106, 1594-1605.
- Bianchi, R., Gatti, C., Adovasio, V. and Nardelli, M. (1996) Theoretical and experimental (113K) electron-density study of Lithium *bis*(tetramethylammonium) hexanitrocobaltate (III) Acta Crystallographica, B, 471-478.
- Biegler-König, F.W., Bader, R.F.W. and Tang, T.H. (1982) Calculation of the average properties of atoms in molecules. II Journal of Computational chemistry, 13, 317-328.
- Boisen, M.B. and Gibbs, G.V. (1993) A modeling of the structure and compressibility of quartz with a molecular potential and its transferability to cristobalite and coesite. Physics and Chemistry of Minerals, 20, 123-135.

- Boyd, R.J. and Edgecombe, K.E. (1988) Atomic and group electronegativities from the electron density distributions of molecules *Journal of the American Chemical Society*, 110, 4182-4186.
- Cremer, D. and Kraka, E. (1984) A Description of the Chemical Bond in Terms of Local Properties of Electron Density and Energy *Croatica Chemica Acta*, 57, 1259-1281.
- Cruickshank DWJ (1961) The role of 3d-orbitals in between (a) silicon, phosphorus, sulphur, or chlorine and (b) oxygen or nitrogen *J Chem Soc*, 1961, 5486-5504.
- D'Arco, Ph., Sandrone, G., Dovesi, R., Orlando, R. and Saunders, V.R. (1993) A quantum mechanical study of the perovskite structure type of  $\text{MgSiO}_3$  *Physics and Chemistry of Minerals*, 20, 407-414.
- Dovesi, R., Roetti, C., Freyria-Fava, C., Prencipe, M. and Saunders, V.R. (1991) On the elastic properties of lithium, sodium and potassium oxide. An ab-initio study *Journal of Chemical Physics*, 156, 11-19.
- Dovesi, R., Saunders, V.R., Roetti, C., Causa, M., Harrison, N.M., Orlando, R. and Apra, E. (1996) *CRYSTAL95 User's Manual* University of Torino Torino, Italy 1-170.
- Downs, J.W. (1991) Electrostatic properties of minerals from X-ray diffraction data: A guide for accurate atomistic models, In J. Ganguly, Ed, *Diffusion, Atomic Ordering, and Mass Transport*, *Advances in Physical Geochemistry*, Vol. 8 Springer-Verlag Berlin.
- Downs, J.W. (1995) The electron density distribution of coesite, *Journal of Physical Chemistry*, 99, 6849-6856.
- Frisch, M.J., Trucks, G.W., Schlegel, H.B., Gill, P.M.W., Johnson, B.G., Wong, M.W., Foresman, J.B., Robb, M.A., Head-Gordon, M., Replogle, E.S., Gomperts, R., Andres, J.L., Raghavachari, K., Binkley, S., Gonzalez, C., Martin, R.L., Fox, D.J., Defrees, D.J., Baker, J., Stewart, J.J.P. and Pople, J.A. (1993) *Gaussian 92/DFT, Revision F.2* Gaussian Inc. Pittsburgh, PA.

- Gatti, C., Bianchi, R., Destro, R., Merati, F. (1992) Experimental vs. theoretical topological properties of charge density distributions. An application to the L-alanine molecule studied by X-ray diffraction at 23 K, *Journal of Molecular Structure*, 225, 409-434.
- Gatti, C. (1997) TOPOND96 User's Manual CNR-CSR SRC Milano, Italy 1-15.
- Geisinger, K.L., Spackman, M.A. and Gibbs, G.V. (1987) Exploration of structure, electron density distribution and bonding in coesite with Fourier and pseudoatom refinement methods using single crystal X-ray diffraction data, *JPC*, 91, 3237-3244.
- Gibbs, G.V. (1982) Molecules as models for bonding in silicates, *Am. Min.*, 67, 421-450.
- Gibbs, G.V., M.B. Boisen, Jr., R.T. Downs and A.C. Lasaga, (1988) Mathematical Modeling of the structures and bulk moduli of  $TX_2$  quartz and cristobalite structure types, T=C, Si, Ge and X=O, *S. Materials Science Symposium, Better Ceramics Through Chemistry III* 124-135.
- Gibbs, G.V., Boisen, M.B., Hill, F.C., Tamada, O. and Downs, R.T (submitted) SiO and GeO bonded interactions as inferred from the bond critical point properties of electron density distributions, *Physics and Chemistry of Minerals*.
- Gibbs, G.V., Downs, J.W., Boisen, M.B. (1994) The elusive SiO bond SILICA, *Reviews in Mineralogy*, Vol. 29, Eds. PJ Heaney, CT Prewitt and G.V. Gibbs, Chapt 10, *American Mineralogist*, Washington, DC, 331-368.
- Gibbs, G.V., Hill, F.C., Boisen, M.B. (1997) The SiO bond and electron density distributions *Physics and Chemistry of Minerals*, 23, 167-178.
- Gibbs, G.V., Boisen, M.B. (1998) A molecular modeling of bonded interactions of crystalline silica. *The chemistry of organosilicon compounds*, Vol. 2, Ed. Z. Rappoport and Y. Apeloig, Chapt. 4 John Wiley & Sons, New York, N. Y.

- Hill, F.C., Gibbs, G.V. and Boisen, M.B. (1994) Bond stretching force constants and compressibilities of nitride, oxide, and sulfide coordination polyhedra in molecules and crystals, *Structural Chemistry*, 5, 349-355.
- Hill, F.C., Gibbs, G.V. and Boisen, M.B. (1997) Critical point properties of electron density distributions for oxide molecules containing first and second row cations, *Physics and Chemistry of Minerals*, 24, 582-596.
- Kraka, E. and Cremer, D. (1990) Chemical implications of local features of the electron density distributions, In Z. B. Maskic, Ed., *The concept of the chemical bond* Springer-Verlag Berlin.
- Kramer, G. J., van Beest, B. W. H. and van Santen, R. A. (1991) Relation between crystal symmetry and ionicity in silica polymorphs *Nature*, 351, 636-638.
- Lasaga, A.C. and G.V. Gibbs, (1988) Quantum mechanical potential surfaces and calculations on minerals and molecular clusters. STO-3G and 6-31G\* Results. *Phys Chem Min*, 16, 29-41.
- Lasaga, A. and G.V. Gibbs (1990) *Ab-initio* Quantum Mechanical Calculations of Water-Rock Interactions: Adsorption and Hydrolysis Reactions, *Am J Sci*, 290, 263-295.
- Newton, M.D. and Gibbs, G.V. (1980) *Ab initio* calculated geometries and charge distributions for  $\text{H}_4\text{SiO}_4$  and  $\text{H}_6\text{Si}_2\text{O}_7$  compared with experimental values for silicates and siloxanes, *Physics and Chemistry of Minerals*, 6, 221-246.
- Noll, W. (1968) *Chemistry and Technology of Silicones* Academic Press New York, N.Y.
- Pauling, L. (1940) *The Nature of the Chemical Bond* Cornell University Press Ithaca, N.Y.
- van Beest, B. W. H., Kramer, G. J. and van Santen, R. A. (1990) Force fields for silicas and aluminophosphates based on *ab initio* calculations *Phys Rev Lett*, 64, 1955-1958.
- Zoltai, T. and Buerger, M.J. (1959) The crystal structure of coesite, the dense, high-pressure form of silica, *Zeits Krist*, 111, 129-141.

# Curriculum Vitae

## Kevin M. Rosso

Research Scientist  
Environmental Molecular Sciences Laboratory - Battelle PNNL  
P.O. Box 999, K8-96  
Richland, WA 99352  
USA

---

### Personal Data:

BIRTH DATE: October 8, 1968  
BIRTH PLACE: Los Angeles, CA  
FAMILY STATUS: Married, no children

### Education:

- Ph.D. GEOCHEMISTRY (1998) *Virginia Polytechnic Institute and State University*  
Primary research focused on the electronic structure, oxidation mechanisms, and fundamental reactivity of sulfide surfaces at the atomic scale using *ab-initio* and molecular mechanics calculations, and ultra-high vacuum scanning tunneling microscopy and spectroscopy. Other projects included studying sorption reactions and energetics using *ab-initio* calculations; surface diffusion and defect structure modeling using molecular mechanics, molecular dynamics, and *ab-initio* calculations; and investigating mineral reactivity by modeling the electron density and its Laplacian. Coursework emphasis in surface science, chemical kinetics, and crystal chemistry.
- M.S. GEOCHEMISTRY (1994) *Virginia Polytechnic Institute and State University*  
Research focused on the quantification of CO<sub>2</sub> pressure and temperature in microscopic mixed-gas fluid inclusions using vibrational spectroscopy. Coursework emphasis in aqueous geochemistry, physical chemistry, and statistical thermodynamics.
- B.S. GEOCHEMISTRY (1992) *California State Polytechnic University, Pomona*  
Thesis on the geochemical evolution of silver-barite mineralization in the Calico Mtns., CA. Coursework emphasis in aqueous geochemistry, physics, and computer science.

### Employment:

- 6/98 - present RESEARCH SCIENTIST - *Environmental Molecular Sciences Laboratory, Battlle PNNL*
- 5/94 - 6/98 GRADUATE RESEARCH ASSISTANT - *Virginia Polytechnic Institute and State University*  
Responsibilities include primarily research, UNIX system administration, UHV instrumentation maintenance and repair, PC hardware and network administration, and design and construction of experimental equipment.
- 8/92 - 5/94 GRADUATE TEACHING ASSISTANT - *Virginia Polytechnic Institute and State University*  
Designed and instructed effective introductory geology laboratory courses.
- 6/92 - 8/92 GEOLOGIST - *United States Geological Survey*  
Performed field based data acquisition for a large-scale geochemical survey.

**Honors:**

Invited speaker for the *Molecular Modeling of Mineral Surfaces* special session at the 1998 Meeting of the Clay Minerals Society, Cleveland, Ohio, June 6-10.

Invited speaker for the *Theoretical Molecular Models in Earth Sciences* theme session at the 1997 Meeting of the Geological Society of America, Salt Lake City, Utah, October 20-24.

Awarded *National Association of Geology Teachers - United States Geological Society Survey Internship* for excellence in geologic field studies. (Summer 1992)

**Research Interests:**

Elucidating the relationships between the atomic and electronic structure of earth materials with their reactivity and physical properties, particularly on surfaces, using various aspects of surface science, chemistry, solid state physics, mineralogy, and crystal chemistry.

Investigating the mechanisms, energetics, and kinetics of reactions at surfaces and interfaces at the molecular scale such as metal and/or gas sorption reactions, oxidation/electron transfer, and precipitation/dissolution.

Combining theoretical modeling with experimental approaches to understand surfaces and surface reactions, from the atomic scale to macro-scale.

**Expertise:****Computational Chemistry - Molecular and electronic structure modeling using:**

GAUSSIAN94 and CRYSTAL95/DFT *ab-initio* codes

TOPOND Atoms-in-Molecules/Laplacian *ab-initio* code

GULP and MARVIN ionic potential/molecular mechanics/dynamics codes

HYPERCHEM *ab-initio*/molecular mechanics/dynamics/semi-empirical code

**Surface Science - Practical application, instrumentation, and theory of:**

Scanning tunneling microscopy and spectroscopy (STM/STS)

Ion beam sputter/anneal surface preparation

X-ray and ultra-violet photoelectron spectroscopy (XPS/UPS)

Auger electron spectroscopy (AES)

Low energy electron diffraction (LEED)

Atomic force microscopy (AFM)

Secondary ion mass spectroscopy (SIMS)

**Bulk Analytical Techniques - Practical application, instrumentation, and theory of:**

Raman/Fourier transform infra-red (FTIR) spectroscopy

Scanning electron microscopy and energy dispersive spectroscopy (SEM/EDS)

Powder X-ray diffraction (XRD)

**Technical Skills - Experimental strengths in:**

UHV instrumentation, vacuum systems, repair, and maintenance

Digital and analog electronics design, circuit construction, and diagnostics

Design and construction of experimental apparatus

**Computer Expertise:**

UNIX system administration  
FORTRAN programming; some C experience  
OS's and environments: UNIX, Windows95, DOS, DEC Windows, Solaris  
PC hardware and networking; ISA bus data acquisition and computer interfacing

**Selected Publications:**

- Rosso K.M.** and Bodnar R.J. (1995) *Microthermometric and Raman spectroscopic detection limits of CO<sub>2</sub> in fluid inclusions and the Raman spectroscopic characterization of CO<sub>2</sub>*. *Geochimica et Cosmochimica Acta*, 59, 3961-3975.
- Schmidt C., **Rosso K.M.** and Bodnar R.J. (1995) *Synthetic fluid inclusions: XIII. Experimental determination of PVT properties in the system H<sub>2</sub>O+40 wt%NaCl + 5 mol%CO<sub>2</sub> at elevated temperature and pressure*. *Geochimica et Cosmochimica Acta*, 59, 3953-3959.
- Becker U., Greatbanks S.P., **Rosso K.M.**, Hillier I.H., and Vaughan D.J. (1997) *An embedding approach for the calculation of STM images: Method development and application to galena (PbS)*. *Journal of Chemical Physics*, 107 (18), 7537-7542.
- Hochella M.F., Jr., Rakovan J.F., **Rosso K.M.**, Bickmore B.R., and Rufe E. (in press) *New directions in mineral surface geochemical research using scanning probe microscopes*. American Chemical Society Special Volume.
- Rosso K.M.**, Gibbs G.V., and Boisen M.B. (accepted to *Phys Chem Min*) *SiO and BeO bonded interactions: A comparison of crystalline, molecular and experimental electron density distributions*.
- Rosso K.M.** and Hochella M.F., Jr. (submitted to *Am Min*) *The Interaction of Pyrite {100} Surfaces with O<sub>2</sub> and H<sub>2</sub>O: Fundamental Oxidation Mechanisms*.
- Rosso K.M.** and Hochella M.F., Jr. (submitted to *Am Min*) *Atomically Resolved Electronic Structure of Pyrite {100} Surfaces: An Experimental and Theoretical Investigation with Implications for Reactivity*.
- Rosso K.M.** and Hochella M.F., Jr. (submitted to *Surf. Sci.*) *A UHVSTM/STS and ab-initio investigation of covellite (CuS) {001} surfaces*.
- Rosso K.M.**, Becker U., and Hochella M.F., Jr. (in preparation) *"Real-time" UHVSTM observation and molecular modeling of surface defect healing on pyrite*.
- Becker U., **Rosso K.M.**, and Hochella M.F., Jr. (in preparation) *Experimental and theoretical treatment of the electronic structure of defects on galena (PbS) surfaces*.

**Recent Abstracts Presented at National Meetings:**

- Rosso K.M.** and Hochella M.F., Jr. (1997) *Spectroscopic and microscopic investigations of the fundamental characteristics and reactivity of pyrite surfaces*. Presented at the Meeting of the American Chemical Society, San Francisco, California, April 13-17.
- Rosso K.M.** and Hochella M.F., Jr. (1997) *Investigation of the local electronic structure of pyrite {100} surfaces: A combined UHVSTM/STS and ab-initio modeling study*. Presented at the Meeting of the Geological Society of America, Salt Lake City, Utah, October 20-24.
- Rosso K.M.**, Becker U., and Hochella M.F., Jr. (1998) *Investigating molecular-scale surface dynamics and reactivity: Combining UHV STM/STS and theoretical calculations*. Presented at the Meeting of the Clay Minerals Society, Cleveland, Ohio, June 6-10.